

RAM

● ROBOTICS
AND
MECHATRONICS

UNDERSTANDING ADHESION FACTORS BETWEEN THIN METAL SHEETS, TOWARDS ROBOTIC DESTACKING

R.C. (Carlo) Boeve

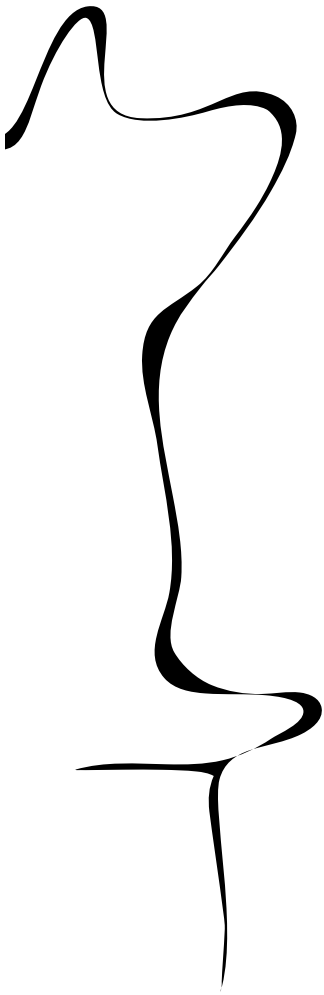
MSC ASSIGNMENT

Committee:

dr. ir. D. Dresscher
dr. ir. R.G.K.M. Aarts

April, 2025

017RaM2025
Robotics and Mechatronics
EEMCS
University of Twente
P.O. Box 217
7500 AE Enschede
The Netherlands



UNIVERSITY OF TWENTE. | **TECHMED CENTRE**

UNIVERSITY OF TWENTE. | **DIGITAL SOCIETY INSTITUTE**

Contents

1	Introduction	4
1.1	Context	4
1.2	Problem description	4
1.3	Goal	5
1.4	Research questions	5
1.5	Approach	5
1.6	Document outline	6
2	Background	7
2.1	Introduction	7
2.2	Surface tension	7
2.3	Laplace pressure	8
2.4	Magnetization	10
2.5	Cantilever beam deflection for a point load	11
2.6	Cantilever beam deflection for a uniformly distributed load	13
2.7	Cantilever-hinged beam deflection for a distributed load	15
2.8	Area moment of inertia	18
3	Industry professionals	22
3.1	Introduction	22
3.2	Practical examples	22
3.3	Actions taken to solve the problem	23
3.4	Insights into critical factors	23
3.5	Potential approaches to a solution	24
3.6	Conclusion	25
4	Literature analysis	26
4.1	Introduction	26
4.2	Adhesion factors	26
4.3	Destacking problem	30
4.4	Solutions in literature	34
5	Preliminary experiments	39
5.1	Introduction	39
5.2	Hypothesis	39
5.3	Experimental design and setup	40
5.4	Results	42

5.5	Conclusion	43
6	Model development and validation	45
6.1	Introduction	45
6.2	Cross-sectional model development	45
6.3	Finite element model development	58
6.4	Model validation	62
6.5	Conclusion	66
7	Discussion	67
7.1	Analysis of breaking force prediction discrepancies	67
7.2	Evaluation of Modelling Approaches	68
7.3	Limitations	68
8	Conclusion	70
8.1	Research questions	70
8.2	Empirical findings	70
8.3	Future research directions	71
8.4	Final Remarks	72
A	Interviews	76
A.1	Interview questions	76
A.2	Respondent A transcript	76
A.3	Respondent B transcript	82
B	Derivation area moment of inertia $I_{y'}$	87
C	Derivation distributed load f	92

Chapter 1

Introduction

1.1 Context

The sheet metal industry is constantly advancing, driven by a need for cost reduction, efficiency and reliability. The demand for automated solutions in the sheet metal industry has risen significantly due to developing automotive, electronics and construction industries that heavily rely on these parts. Automated solutions in sheet metal handling often use robotic manipulators. The manipulators are designed to transport, position and process thin metal sheets with high precision. These robots reduce manual labour, improve production efficiency and enhance factory safety.

However, despite the innovations in the robotic automation, certain challenges persist, especially in the handling of thin metal sheets. One of the most significant issues is the tendency of thin metal sheets to stick together. This issue is commonly referred to as the destacking problem or the double-sheet problem and it poses a significant problem for the sheet metal automation industry. When sheets stick together, the robotic manipulator might pick up multiple parts at once from a stack of products. Doing so can lead to equipment damage, safety hazards and downtime. Finding a solution to the destacking problem is crucial in ensuring the reliability of automated sheet metal handling robots.

1.2 Problem description

The destacking problem arises when one or multiple products stick to the product that is being destacked by the robot. There are multiple reasons why this effect is very undesirable in a robotic part handling application.

When additional products are picked up at once, these products can consequently be fed into machinery that was not prepared for multiple parts. Machines like stamping presses or deburring machines can malfunction if multiple stacked parts are entered at once. This can lead to downtime or even expensive damage to the machinery.

Carrying more products than intended can also cause the additional products to detach from the robot during handling. This causes the products to fall down and damage both the products and the robotic cell. Additionally, these detaching parts can form a safety hazard. When the robot moved the parts at high speeds and some products detach, this can result in a dangerous situation.

Since the robot is attaching to the top side of the product, it has no way of knowing if there are multiple products attached to the top product. This further increases the need for a solution that

eliminates the risk of double-sheet pickups.

There are multiple factors that can contribute to the sticking effect between products. A partial vacuum between sheets can cause the top products to be squeezed together as long as there is a seal in between them. Magnetic forces from inside the sheets or from magnetic effectors can cause products to stick together. Surface forces of two smooth surfaces that are very close together can also play a role in the sticking effect. In order to design a suitable solution for the destacking problem, it is necessary to uncover the mechanisms behind the destacking problem. Designing a suitable solution to the destacking problem requires a complete understanding of the problem at hand.

1.3 Goal

The primary objective of this project is to deepen the understanding of the critical factors that influence effective sheet separation during the destacking process. To achieve this, the thesis focuses exclusively on examining the destacking behaviour of two stacked thin metal sheets.

1.4 Research questions

This assignment aim to reach this goal by answering the following research questions: **How can the critical factors, that contribute to the successful and efficient destacking of thin metal sheets using robotic manipulators, be optimized?**

- How do industry professionals experience and perceive the destacking problem?
- What are the factors that cause adhesion between thin metal sheets, and under what conditions do these forces become significant?
- Under which conditions do adhesive effects influence destacking and when does this become problematic?
- What solutions to the destacking problem have been discussed in the literature?
- How can these insights be used to improve automated destacking procedures?

1.5 Approach

Interviews are conducted with industry professionals who have hands-on experience with the destacking problem to get an understanding of the issue. These professionals provide practical insights into the challenges faced in real-world applications, their perspectives on the primary contributing factors, and their assessments of the most suitable solutions. These interviews result in a more realistic view of the destacking problem, underlying mechanisms and promising solutions.

To expand the findings from the interviews, a literature analysis is conducted to gather relevant information on the destacking problem. This analysis discusses both academic and industry sources to ensure a broad understanding of the issue. Academic sources are used to explore possible causes of the destacking problem, identifying factors that contribute to the destacking problem. These contributing factors are studied, and relevant mathematical models describing their effects on the sticking effect are discussed.

In addition to academic research, industry sources are analysed to investigate previously implemented solutions to the destacking problem. Various techniques used in industrial settings to

overcome the destacking problem are examined for their effectiveness. By combining insights from both academic and industry literature, a well-rounded perspective on the problem and potential solutions is created.

The combined findings from the industry interviews and the literature review lead to the formulation of the main contributing factors to the destacking problem. These factors can be combined into a sum of forces that act on the product. An experimental pulling force setup is used to validate this sum of forces.

The knowledge gained about the destacking problem can be applied in practice to optimize the effector placement process. This process finds the optimal pickup effector locations on a known product surface to ensure successful destacking. To achieve this, a predictive model is required to assess whether the destacking problem will occur.

Such a model must be accurate, computationally efficient, and easy to integrate. Accuracy is important for reliably predicting double-sheet pickups based on the product dimensions and effector locations. Computational efficiency is necessary to prevent long delays in the effector placement process. Additionally, ease of integration into the effector placement process is important for practical implementation.

Different modelling approaches will be evaluated based on three criteria: accuracy, computational efficiency, and the required time investment to develop the model. The latter criteria plays a role because of the limited time span of the thesis.

1.6 Document outline

This thesis is structured as follows:

- Chapter 1 Introduction: Provides an overview of the context, problem description, research questions and approach.
- Chapter 2 Background: Presents fundamental concepts that are used in later chapters.
- Chapter 3 Industry professionals: Discusses findings from interviews with industry professionals, including their perspectives on the main contributing factors and potential solutions.
- Chapter 4 Literature analysis: Analyses relevant academic and industry sources regarding the contributing factors to the destacking problem and existing solutions.
- Chapter 5 Preliminary experiments: Validation of the derived sum of forces acting on a destacking effector through experimental measurements.
- Chapter 6 Model development and validation: details the development of predictive destacking models, validating each approach on accuracy, computational efficiency and required time investment.
- Chapter 7 Discussion: Interprets the results, compares theoretical predictions with experimental findings, and identifies potential refinements.
- Chapter 8 Conclusion: Summarizes the main findings and relates them back to the research questions.

Chapter 2

Background

2.1 Introduction

In order to provide a good foundation for the rest of the thesis, this chapter presents the necessary theoretical background. This chapter will elaborate on several concepts, including surface tension, Laplace pressure, magnetization, cantilever deflections and the area moment of inertia.

2.2 Surface tension

Molecules in a liquid are attracted to each other, these attractive forces are called cohesive forces. Cohesive forces in liquids include hydrogen bonding and Van der Waals forces [1]. Figure 2.1 shows a liquid surface with one molecule at the surface and one inside the liquid. The molecule inside the liquid experiences cohesive forces in all directions, which results in a net force of zero. The molecule at the surface only has cohesive forces on one side, resulting in a net inward force. This force pulls the surface molecules inward. The inward force is counteracted by the compression forces of the liquid.

The net inward forces on the surface result in a tension that minimized that surface area. This tension is called the surface tension γ of the liquid. The surface tension can be expressed as energy per surface area [Jm^{-2}], or as force over distance [Nm^{-1}]. A sphere is the shape that has the smallest surface area to volume ratio. This is why the surface tension in liquids result in spherical droplets or bubbles. The surfaces of such droplets or bubbles are so smooth that the fluctuations in surface thickness are in the order of Angströms (10^{-10}m) [1].

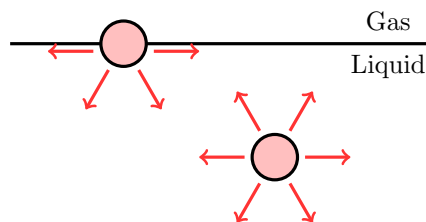


Figure 2.1: Liquid molecules, one at the surface and one inside the liquid. Cohesive forces are shown in red.

Figure 2.2 shows an experiment that can be done to demonstrate the stored energy in a surface. The figure shows a rectangular frame of which the right side can freely move from left to right. When this device is dipped into a liquid like bubble soap, a liquid film will form inside the rectangular frame. Once the frame is lifted from the liquid, the surface tension of this liquid film will pull on all sides of the frame. This pulling force will set the right side of the frame in motion since this is the only side that is able to move. The pulling force on the right side is determined by the length l of this side and the surface tension γ of the liquid. This pulling force is expressed in Equation 2.1. The factor 2 reflects the presence of two surfaces: the top of the liquid film and the bottom of the film [1].

$$F_\gamma = 2\gamma l \quad (2.1)$$

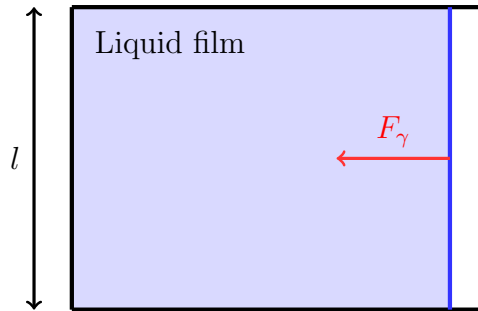


Figure 2.2: Liquid film in a square frame with one movable side on the right.

2.3 Laplace pressure

A droplet contains a curved surface that forms an interface between two liquids, as shown in Figure 2.3. This curvature creates a pressure difference, $\Delta P_{\text{Laplace}}$, between the two liquids. The pressure difference arises due to the surface tension of the liquid and the curvature of the interface.

In two dimensions, the curvature of a line at a given point is defined by a single radius. In three dimensions, the curvature of a surface at a given point is described by two radii, known as the principal radii, as can be seen in Figure 2.4. These principal radii influence the pressure difference across the interface. The relationship between the principal radii, surface tension, and the resulting pressure difference is given by the Young–Laplace equation (Equation 2.2) [3].

$$\Delta P_{\text{Laplace}} = \gamma \left(\frac{1}{r_1} + \frac{1}{r_2} \right) \quad (2.2)$$

Where:

- $\Delta P_{\text{Laplace}}$ [Pa] is the pressure difference due to the Laplace pressure across the interface.
- γ [N m^{-1}] is the surface tension.
- r_1 and r_2 [m] are the principal radii of curvature.

The principal radii of a given surface can be determined as follows: a normal is drawn through a point on the surface, and a plane is placed through this normal. The intersection radius between

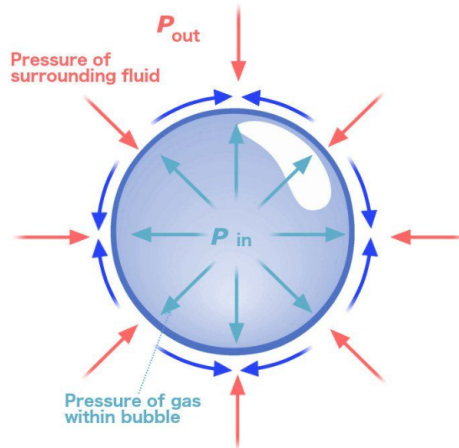


Figure 2.3: Diagram of a droplet indicating the surface tension (dark blue), internal pressure (light blue) and external pressure (red) [2].

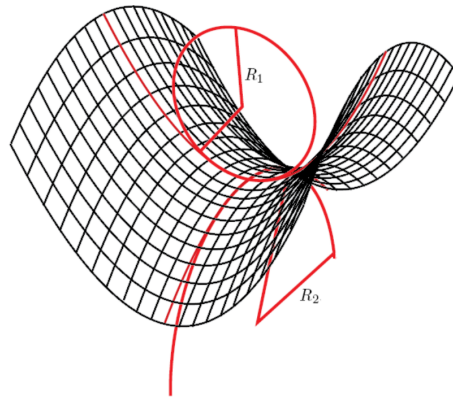


Figure 2.4: Diagram showcasing how the principal radii of curvature R_1 and R_2 describe the curvature of a surface at one point [4].

the surface and this plane is r_1 . A second plane is then placed through the normal, perpendicular to the first plane. The intersection radius of the surface with this second plane is r_2 .

- For a cylindrical surface with radius r_c : $r_1 = r_c, r_2 = \infty$
- For a spherical surface with radius r_s : $r_1 = r_2 = r_s$

A liquid bridge, such as water between two sand grains, generates an adhesive force between the bodies [5]. This adhesive force arises from both the Laplace pressure and capillary forces acting on the spheres. The strength of the adhesive force depends on the separation distance between the bodies, and the liquid bridge will rupture beyond a critical separation distance.

Figure 2.5 illustrates a cross-section of two spheres with a liquid bridge between them. In this figure:

- R [m] is the radius of the spheres.

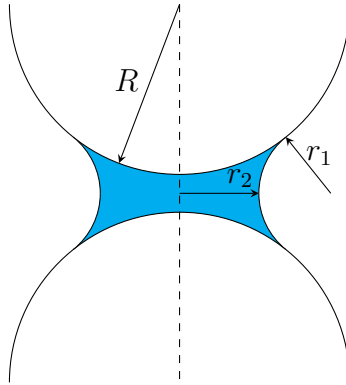


Figure 2.5: Liquid bridge between two spheres.

- r_1 [m] is the curvature of the liquid bridge.
- r_2 [m] is the inner radius of the liquid bridge [3].

The Laplace pressure for this situation can be calculation using Equation 2.2.

2.4 Magnetization

On an atomic scale, a material contains tiny currents in the form of electrons orbiting around nuclei. These currents are small and can be treated as magnetic dipoles. Ordinarily, these magnetic poles cancel each other due to the random orientations of the atoms in the material. However, when an external magnetic field is applied, a net magnetic alignment occurs. This causes the material to become magnetized [6].

Some materials can retain their magnetic polarity after the external magnetic field has been removed and are called ferromagnets or just magnets. Magnets have a magnetic north pole and a magnetic south pole. When two magnets are brought together, their opposite magnetic poles will attract and the poles with the same polarity will repel each other as can be seen in Figure 2.6.

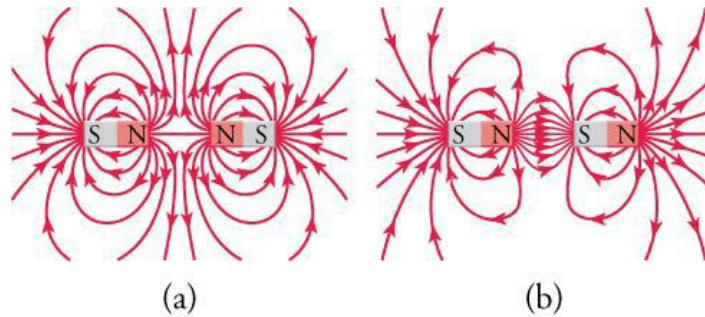


Figure 2.6: Magnetic poles with the same polarity repel each other (a) while poles of different polarity attract each other (b) [7].

To calculate the magnetic force between two magnets, the approximation in Equation 2.3 can

be used [8]. This approximation assumes an infinite high permeability of the steel magnets, parallel magnet surfaces and an uniform magnetic field between the magnets.

$$F = \frac{B^2 A}{2\mu_0} \quad (2.3)$$

Here, F [N] is the magnetic force between the magnets, B [T] is the magnetic flux density, A [m²] is the area of the parallel magnets and μ_0 is the permeability of free space ($4\pi \cdot 10^{-7}$ TmA⁻¹).

2.5 Cantilever beam deflection for a point load

Figure 2.7 shows a sketch of a cantilever beam that is subjected to a downward point load at the end of the beam. Cantilever beams are fixed in x-movement, y-movement and rotation on one side of the beam [9]. This statics model is used to walk through the process of deriving a deflection function $v(x)$ for a beam with given constraints and loads. A deflection function gives the y-movement of the beam at any location x along the beam.

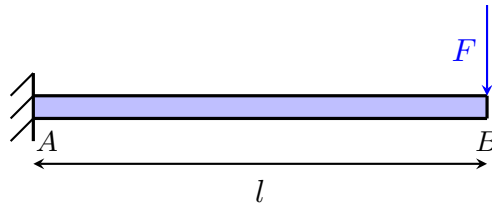


Figure 2.7: Sketch of a cantilever beam that is subjected to a point load.

The first step is to draw a free body diagram of the situation. A free body diagram only shows the structure of interest and the relevant loads, it can be used to derive equations of equilibrium [9]. Figure 2.8 shows the free body diagram of a cantilever beam that is subjected to a point load.

The second step is to note down the equations of equilibrium for one point on the beam. For a cantilever beam it is easiest to first evaluate the equilibrium at point A ($x = 0$):

$$\sum F_y \uparrow + = 0 = F_A - F \quad (2.4)$$

$$F_A = F \quad (2.5)$$

$$\sum M_A \circlearrowleft + = 0 = M_A - Fl \quad (2.6)$$

$$M = Fl \quad (2.7)$$

Note that the equilibrium forces in the x-direction were not noted down. This is because there are no forces acting in this direction and this equilibrium equation is therefore not of interest.

The third step is to cut the beam at location x , and draw the free body diagram of one of the sections of the beam [9]. This free body diagram can be used to derive expressions for the internal shear force $S(x)$ and bending moment $M(x)$. Figure 2.9 shows the left section of the beam that is cut at location x .

The expressions for $S(x)$ and $M(x)$ are obtained by noting down the equations of equilibrium at position x along the beam, this is the right side of the section in Figure 2.9:

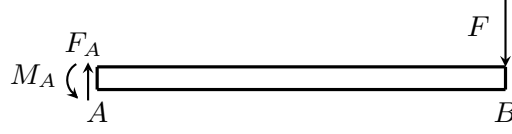


Figure 2.8: Free body diagram of the cantilever beam in figure 2.7.

$$\sum F_y \uparrow + = 0 = F_A - S(x) \quad (2.8)$$

$$S(x) = F_A \quad (2.9)$$

$$\sum M \circlearrowleft + = 0 = M_A + M(x) - F_A x \quad (2.10)$$

$$M(x) = F_A x - M_A \quad (2.11)$$

$$M(x) = Fx - Fl \quad (2.12)$$

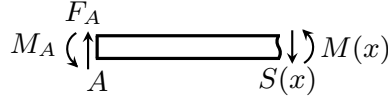


Figure 2.9: Free body diagram of a section of the beam in figure 2.8, the diagram shows the left side of a cut in the beam in location x .

An expression of the bending moment $M(x)$ can be used to derive an expression of the deflection function $v(x)$. This can be done by using the following expression from the Euler-Bernoulli beam theory [9] [10]:

$$M(x) = EI \frac{d^2 v(x)}{dx^2} \quad (2.13)$$

$$EIv(x) = \iint M(x) dx^2 \quad (2.14)$$

$$EIv(x) = \iint Fx - Fl dx^2 \quad (2.15)$$

$$EIv(x) = \int \frac{1}{2} Fx^2 - Flx + C_1 dx \quad (2.16)$$

$$EIv(x) = \frac{1}{6} Fx^3 - \frac{1}{2} Flx^2 + C_1 x + C_2 \quad (2.17)$$

$$v(x) = \frac{1}{6EI} Fx^3 - \frac{1}{2EI} Flx^2 + \frac{1}{EI} C_1 x + \frac{1}{EI} C_2 \quad (2.18)$$

In this expression, E is the Young's modulus of the material and I is the area moment of inertia of the beam. Lastly, boundary conditions can be used to determine the unknowns in the deflection function $v(x)$. For the situation in Figure 2.7, the deflection and the angle of the beam are zero at point A ($x = 0$). This is because the beam is fixed in both the y -direction and the rotation angle here. This boundary condition introduces the following two equations:

$$v(0) = 0 \quad (2.19)$$

$$\frac{dv(0)}{dx} = 0 \quad (2.20)$$

These boundary conditions can be used to determine the two unknowns in the expression of $v(x)$: C_1 and C_2 .

$$v(0) = 0 = \frac{1}{EI}C_2 \quad (2.21)$$

$$C_2 = 0 \quad (2.22)$$

$$\frac{dv(0)}{dx} = 0 = \frac{1}{EI}C_1 \quad (2.23)$$

$$C_1 = 0 \quad (2.24)$$

This results in the final expression for the deflection function of a cantilever beam that is subjected to a point load:

$$v(x) = \frac{F}{6EI}x^3 - \frac{Fl}{2EI}x^2 \quad (2.25)$$

2.6 Cantilever beam deflection for a uniformly distributed load

This section describes the derivation of the deflection function $v(x)$ of a cantilever beam that is subjected to a distributed load. This is a load type that is applied over a certain length and is therefore expressed in N m^{-1} . Figure 2.10 shows such a cantilever beam that is subjected to a downward distributed load f across the whole length l of the beam. In this figure, point A is located at $x = 0$, and point B is located at $x = l$.

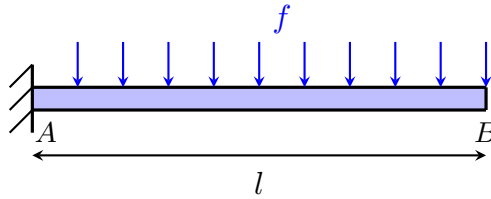


Figure 2.10: Cantilever beam with a downward uniformly distributed load f .

The free body diagram that corresponds to Figure 2.10 can be seen in Figure 2.11. This diagram includes the beam structure, the distributed force f and the reaction force F_A and moment M_A from the fixed condition on the left. Using this free body diagram, the equations of equilibrium at point A can be formulated:

$$\sum F_y \uparrow + = 0 = F_A - fl \quad (2.26)$$

$$F_A = fl \quad (2.27)$$

$$\sum M \circlearrowleft + = 0 = M_A - \frac{1}{2}fl^2 \quad (2.28)$$

$$M_A = \frac{1}{2}fl^2 \quad (2.29)$$

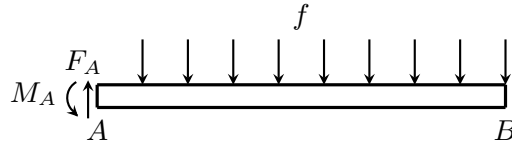


Figure 2.11: Free body diagram of the cantilever beam in figure 2.10.

An expression for the internal moment $M(x)$ can be used to derive an expression for the deflection function $v(x)$. The internal moment at location x can be found by cutting a beam at this location and formulating the equations of equilibrium. The free body diagram of the left section of the beam that is cut at x can be seen in Figure 2.12. This free body diagram can be used to formulate the equations of equilibrium at x :

$$\sum F_Y \uparrow + = 0 = F_A - fx - S(x) \quad (2.30)$$

$$S(x) = F_A - fx \quad (2.31)$$

$$S(x) = fl - fx \quad (2.32)$$

$$\sum M \circlearrowleft + = 0 = M(x) + M_A + \frac{1}{2}fx^2 - F_Ax \quad (2.33)$$

$$M(x) = -\frac{1}{2}fx^2 + F_Ax - M_A \quad (2.34)$$

$$M(x) = -\frac{1}{2}fx^2 + flx - \frac{1}{2}fl^2 \quad (2.35)$$

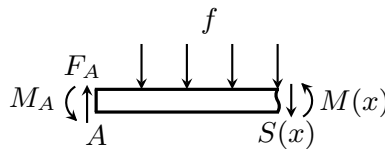


Figure 2.12: Free body diagram of a section of the beam in figure 2.11, the diagram shows the left side of a cut in the beam in location x .

The Euler-Bernoulli beam theory can again be used to derive the deflection function $v(x)$ from the internal moment $M(x)$:

$$M(x) = EI \frac{d^2v(x)}{dx^2} \quad (2.36)$$

$$EIv(x) = \iint M(x) dx^2 \quad (2.37)$$

$$EIv(x) = \iint \left(-\frac{1}{2}fx^2 + flx - \frac{1}{2}fl^2 \right) dx^2 \quad (2.38)$$

$$EIv(x) = \int \left(-\frac{1}{6}fx^3 + \frac{1}{2}flx^2 - \frac{1}{2}fl^2x + C_1 \right) dx \quad (2.39)$$

$$EIv(x) = -\frac{1}{24}fx^4 + \frac{1}{6}flx^3 - \frac{1}{4}fl^2x^2 + C_1x + C_2 \quad (2.40)$$

$$v(x) = -\frac{1}{24EI}fx^4 + \frac{1}{6EI}flx^3 - \frac{1}{4EI}fl^2x^2 + \frac{1}{EI}C_1x + \frac{1}{EI}C_2 \quad (2.41)$$

The beam is fixed on the left side at $x = 0$, meaning that it has zero deflection and slope at this location. This results in the following boundary conditions:

$$v(0) = 0 \quad (2.42)$$

$$\frac{dv(0)}{dx} = 0 \quad (2.43)$$

These boundary conditions can be used to solve for C_1 and C_2 in the deflection equation:

$$v(0) = 0 = \frac{1}{EI}C_2 \quad (2.44)$$

$$C_2 = 0 \quad (2.45)$$

$$\frac{dv(0)}{dx} = 0 = \frac{1}{EI}C_1 \quad (2.46)$$

$$C_1 = 0 \quad (2.47)$$

This results in the final deflection function $v(x)$ for a cantilever beam that is subjected to a distributed load:

$$v(x) = -\frac{1}{24EI}fx^4 + \frac{1}{6EI}flx^3 - \frac{1}{4EI}fl^2x^2 \quad (2.48)$$

2.7 Cantilever-hinged beam deflection for a distributed load

Figure 2.13 shows a cantilever beam that is hinged on a roller on the right side. This means that the beam is completely restricted on the left side and restricted in the y-direction on the right side ($v(l) = 0$). The beam is also subjected to a downward distributed load. Point A on this beam is on the left side ($x = 0$) and point B is on the right side ($x = l$). The free body diagram of the beam can be seen in Figure 2.14.

This free body diagram can be used to formulate the equations of equilibrium at point A :

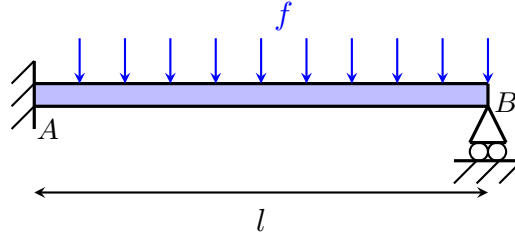


Figure 2.13: Cantilever-hinged beam with a downward uniformly distributed load f .

$$\sum F_y \uparrow + = 0 = F_A + F_B - fl \quad (2.49)$$

$$F_A = fl - F_B \quad (2.50)$$

$$\sum M \circlearrowleft + = 0 = M_A + F_B l - \frac{1}{2} fl^2 \quad (2.51)$$

$$M_A = \frac{1}{2} fl^2 - F_B l \quad (2.52)$$

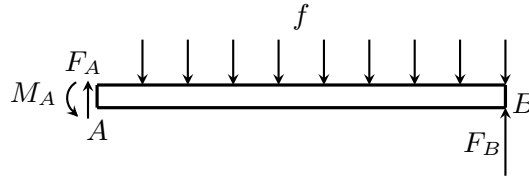


Figure 2.14: Free body diagram of the cantilever-hinged beam in figure 2.13.

A free body diagram of a section of the beam can be used to derive an expression for the internal moment $M(x)$ at a location x on the beam. The internal moment can then be used to obtain an expression for the deviation function $v(x)$. Figure 2.15 shows a free body diagram of the left section of the beam in Figure 2.14 which is cut at location x . The internal moment $M(x)$ is obtained from the equilibrium equations at x as follows:

$$\sum F_Y \uparrow + = 0 = F_A - fx - S(x) \quad (2.53)$$

$$S(x) = F_A - fx \quad (2.54)$$

$$S(x) = fl - F_B - fx \quad (2.55)$$

$$\sum M \circlearrowleft + = 0 = M(x) + M_A + \frac{1}{2} fx^2 - F_A x \quad (2.56)$$

$$M(x) = -\frac{1}{2} fx^2 + F_A x - M_A \quad (2.57)$$

$$M(x) = -\frac{1}{2} fx^2 + flx - F_B x - \frac{1}{2} fl^2 + F_B l \quad (2.58)$$

The Euler-Bernoulli beam theory can be used to derive the deflection function $v(x)$ from the internal moment $M(x)$:

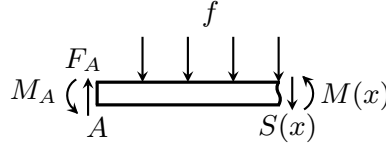


Figure 2.15: Free body diagram of a section of the beam in figure 2.14, the diagram shows the left side of a cut in the beam in location x .

$$M(x) = EI \frac{d^2 v(x)}{dx^2} \quad (2.59)$$

$$EIv(x) = \iint M(x) dx^2 \quad (2.60)$$

$$EIv(x) = \iint \left(-\frac{1}{2}fx^2 + flx - F_Bx - \frac{1}{2}fl^2 + F_Bl \right) dx^2 \quad (2.61)$$

$$EIv(x) = \int \left(-\frac{1}{6}fx^3 + \frac{1}{2}flx^2 - \frac{1}{2}F_Bx^2 - \frac{1}{2}fl^2x + F_Blx + C_1 \right) dx \quad (2.62)$$

$$EIv(x) = -\frac{1}{24}fx^4 + \frac{1}{6}flx^3 - \frac{1}{6}F_Bx^3 - \frac{1}{4}fl^2x^2 + \frac{1}{2}F_Blx^2 + C_1x + C_2 \quad (2.63)$$

$$v(x) = -\frac{1}{24EI}fx^4 + \frac{1}{6EI}flx^3 - \frac{1}{6EI}F_Bx^3 - \frac{1}{4EI}fl^2x^2 + \frac{1}{2EI}F_Blx^2 + \frac{1}{EI}C_1x + \frac{1}{EI}C_2 \quad (2.64)$$

Similar to sections 2.5 and 2.6, the fixed constraint in the y-direction and in the rotation on the left side of the beam results in the $v(0) = 0$, and the $\frac{dv(0)}{dx} = 0$ boundary conditions. These conditions can be used to determine C_1 and C_2 :

$$v(0) = 0 = \frac{1}{EI}C_2 \quad (2.65)$$

$$C_2 = 0 \quad (2.66)$$

$$\frac{dv(0)}{dx} = 0 = \frac{1}{EI}C_1 \quad (2.67)$$

$$C_1 = 0 \quad (2.68)$$

This results in the following version of the deflection function, which still contains F_B as an unknown:

$$v(x) = -\frac{1}{24EI}fx^4 + \frac{1}{6EI}flx^3 - \frac{1}{6EI}F_Bx^3 - \frac{1}{4EI}fl^2x^2 + \frac{1}{2EI}F_Blx^2 \quad (2.69)$$

The roller hinge fixes the y-coordinate of the beam to zero at position B ($x = l$). This results in the following boundary condition on the right of the beam:

$$v(l) = 0 \quad (2.70)$$

$$v(l) = 0 = -\frac{1}{24EI}fl^4 + \frac{1}{6EI}fl^4 - \frac{1}{6EI}F_Bl^3 - \frac{1}{4EI}fl^4 + \frac{1}{2EI}F_Bl^3 \quad (2.71)$$

$$0 = -\frac{1}{8EI}fl^4 + \frac{1}{3EI}F_Bl^3 \quad (2.72)$$

$$\frac{1}{3EI}F_Bl^3 = \frac{1}{8EI}fl^4 \quad (2.73)$$

$$F_B = \frac{3}{8}fl \quad (2.74)$$

This expression of F_B can be used to get a final version of the deflection function for a cantilever-hinged beam with a distributed load:

$$v(x) = -\frac{1}{24EI}fx^4 + \frac{1}{6EI}flx^3 - \frac{1}{6EI}F_Bx^3 - \frac{1}{4EI}f l^2 x^2 + \frac{1}{2EI}F_Bl x^2 \quad (2.75)$$

$$v(x) = -\frac{1}{24EI}fx^4 + \frac{5}{48EI}flx^3 - \frac{1}{16EI}f l^2 x^2 \quad (2.76)$$

2.8 Area moment of inertia

The bending stiffness of a beam is determined by both its material properties and its geometric characteristics. An important geometric property influencing bending stiffness is the area moment of inertia, denoted by I . Figure 2.16 shows two planks supported at both ends and subjected to a point load in the middle. It can be seen that the plank oriented flat undergoes more bending. This behaviour can be attributed to differences in the area moment of inertia associated with the orientation of the cross-section.

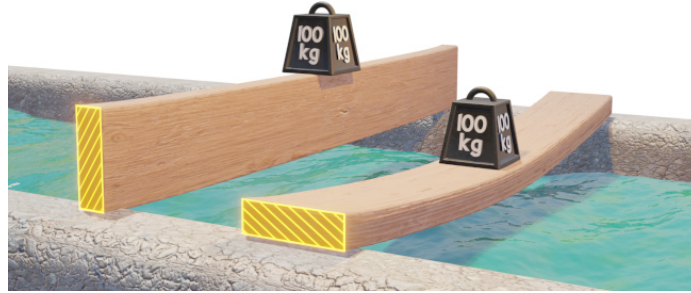


Figure 2.16: Two loaded planks with identical constraints, loads, and cross-sectional areas but differing degrees of bending [11].

A beam in bending experiences compressive internal stresses on one side of the neutral axis and tensile stresses on the other side, as shown in Figure 2.17. This figure shows in red and blue that these stresses increase in magnitude with increasing distance from the neutral axis. Since these internal stresses counteract the bending movement, the more distance there is between the neutral axis and the cross-sectional area, the more resistant the beam will be to bending. This explains

the difference in bending between the planks in Figure 2.16. The vertical plank has more cross-sectional area far away from the neutral axis which results in more internal stresses that counteract the bending.

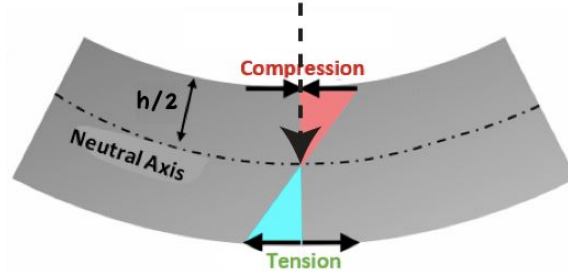


Figure 2.17: Compressive and tensile internal stresses for a beam in bending [12].

The area moment of inertia I is the property of a beam that measures this effect. The higher the area moment of inertia, the more cross-sectional area the beam has away from the bending axis and the stiffer the beam will be around that bending axis. Figure 2.18 shows the area moment of inertia of a horizontal plank, a vertical plank and a H-beam. This also explains why H-beams are shaped the way they are: to optimize the area moment of inertia for optimal stiffness with minimal weight.



Figure 2.18: Area moment of inertia I for three different beam cross-sections [13].

For cross-sections that have an arbitrary cross-section, Equations 2.77 and 2.78 can be used to calculate the area moment of inertia around the x-axis and y-axis [11].

$$I_x = \int y^2 dA \quad (2.77)$$

$$I_y = \int x^2 dA \quad (2.78)$$

Equation 2.77 can for example be used to calculate the area moment of inertia around the x-axis of the beam cross-section in Figure 2.19. This can be done by integrating along the y-axis using $dA = bdy$, as seen in Equations 2.79 to 2.84.

$$I_x = \int y^2 dA \quad (2.79)$$

$$I_x = \int_{-h/2}^{h/2} by^2 dy \quad (2.80)$$

$$I_x = \left[\frac{1}{3} by^3 \right]_{-h/2}^{h/2} \quad (2.81)$$

$$I_x = \frac{1}{3} b \left(\frac{h}{2} \right)^3 - \frac{1}{3} b \left(-\frac{h}{2} \right)^3 \quad (2.82)$$

$$I_x = \frac{bh^3}{24} + \frac{bh^3}{24} \quad (2.83)$$

$$I_x = \frac{bh^3}{12} \quad (2.84)$$

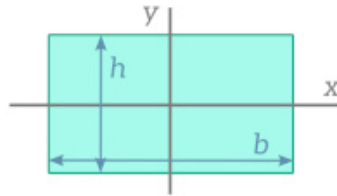


Figure 2.19: Rectangular beam cross-section with height h and width b [13].

Equations 2.77 and 2.78 are however only valid for calculating the area moment of inertia if the bending axes crosses through the centroid of the cross-section. If this is not the case, the parallel axis theorem can be used. Equations 2.85 and 2.86 show the parallel axis theorem versions of the area moment of inertia equations for the x-axis and y-axis. These equations contain the area moment of inertia I_{xc} around the bending axis that does go trough the centroid, plus the area A times the distance between the centroid axis and the actual axis d . These axis can be seen in Figure 2.20, where C is the centroid of the cross-section, X_c is the bending axis through the centroid and X is the actual bending axis.

$$I_x = I_{x_c} + Ad^2 \quad (2.85)$$

$$I_y = I_{y_c} + Ad^2 \quad (2.86)$$

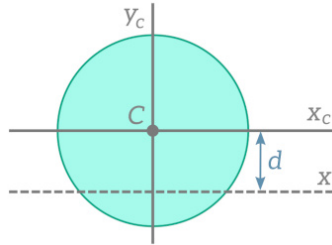


Figure 2.20: Circular cross-section with centroid C , bending axis X , parallel bending axis through centroid X_c and distance between these two axis d [13].

Chapter 3

Industry professionals

3.1 Introduction

The main objective of this thesis is to optimise the destacking process. A solid understanding of the practical aspects of the destacking problem is essential for achieving this. To gain these insights, industry professionals with hands-on experience were interviewed. Their perspectives provide valuable information on the real-world challenges of destacking, complementing the literature analysis.

Respondents were first asked to describe their experiences with the destacking problem, including the contexts in which it occurs and the types of products that were used. They were also asked how the issue was addressed in practice, if a solution was implemented. Additionally, to gain a deeper understanding of their perspectives, respondents were asked to identify the main contributing factors to the problem and suggest their most promising solutions. This chapter summarizes the answers from the respondents.

For this study, two industry professionals were interviewed. Both of these respondents are software developers that work with robotic part-handling systems on a daily basis. The interview questions are provided in Appendix A.1, while the transcripts of respondents A and B can be found in Appendices A.2 and A.3, respectively.

3.2 Practical examples

Industry professionals were asked about their experiences with the destacking problem to gain insights into the practical aspects of this problem.

The destacking issue was encountered in different settings while handling metal sheets using a stretchgripper with vacuum pads. A stretchgripper is an end-effector that can stretch its chassis to adjust the distance between its effectors, allowing it to adapt to different product sizes.

In one instance, relatively large metal sheets measuring approximately 160x140cm with a thickness of about 1 mm were being lifted. However, the sheets tended to stick together, causing multiple sheets to be lifted simultaneously. As they moved, the products would eventually separate mid-air and fall to the ground, resulting in damage.

The problem was also observed with smaller parts measuring 65x30cm. The sticking effect became more pronounced after the parts passed through a deburring machine, which may have induced residual magnetism, further contributing to the adhesion. Although efforts were made to degrease the sheets, the issue persisted, likely due to either the smooth surface of the products or

the residual magnetism.

A similar destacking challenge occurred when handling large, oily metal sheets measuring around one and a half meters in length and approximately three millimetres thick. Despite using vacuum pads rated for thirty kilos, the gripper was unable to pick up any products from the stack because they were all sticking together. The sticking effect was worsened by the vacuum formed between the products during lifting, and the oil layer created a strong seal, making separation even more difficult.

In both cases, the combination of surface conditions, potential residual magnetism, and vacuum effects between the sheets contributed to the destacking problem, presenting significant challenges in destacking these metal components efficiently.

3.3 Actions taken to solve the problem

Industry professionals were asked about the actions they had taken to address the destacking problem. These practical approaches are examined to gain insights into the problem-solving techniques used in real-world scenarios.

Several methods were attempted to resolve the destacking problem. One approach was to avoid applying compressive forces on the stack, as these forces would push more air out from between the sheets and worsen the sticking issue. To address this, the gripper was slowly lowered above the stack with engaged vacuum pads, allowing the sheets to be sucked up when they were close enough. Pickup sensors were used to detect if a sheet had attached successfully. However, this method proved unreliable due to the sensitivity of the sensors, leading to inconsistent results.

Another attempt involved hovering the gripper above the stack after pickup, hoping that any additional sheets would peel off naturally. Unfortunately, this approach failed because not all additional sheets detached in time. A different method involved rotating the gripper around one of its vacuum pads, keeping one pad on the stack while the other moved upward. This movement pressed one side of the sheet into the stack while bending the other side upward, creating a bending moment that could peel off any extra sheets. While this method sometimes worked, it was not consistently reliable and also introduced undesirable compressive forces on one side of the stack.

Additional techniques, such as shaking the gripper and using angled vacuum pads, were tested but had limited success. Products with large holes or slots presented unique challenges because their bending characteristics varied due to weak points in the material.

In another attempt to solve the issue, a new type of gripper was developed. This gripper was a larger variant of the stretching gripper, designed to reach the opposing corners of large products. This new peeling gripper used four vacuum pads arranged in a row, with the outer two pads positioned higher than the middle ones. This configuration created a downward bend in the sheet, inducing a bending moment. As a result, any additional sheets detached because they were affected by the bending moment but were not supported by the vacuum pads. This solution proved successful, and no further issues with destacking were encountered after implementing this gripper. However, a drawback of this design was its specificity—it was tailored for a single product and could not be easily adapted for other products due to its size.

3.4 Insights into critical factors

Industry professionals were asked to share their insights on the critical variables that are involved in the sticking effect between metal sheets. These insights are explored to uncover the underlying causes of the destacking problem.

Several factors contribute to the sticking effect between metal sheets. One of those factors is the amount of compressive force the stack has experienced. Compression can occur during stacking, destacking, or other steps in the manufacturing process. When the sheets are compressed, air is pushed out from between them, leading to stronger vacuums forming during destacking, which intensifies the sticking effect.

The smoothness and cleanliness of the surfaces also play an important role. Very flat, smooth, and clean surfaces without burrs create the strongest seals between sheets, making separation more difficult. In contrast, products with debris or burrs tend to have small air gaps between them, which allows for easier separation. Burrs prevent the sheets from fully contacting each other, thereby disrupting the seal and reducing the vacuum effect.

Another significant factor is the vacuum created between the sheets during destacking. When the products are lifted, a partial vacuum forms between them, and if the seal remains intact, atmospheric pressure pushes down on the sheets, making them difficult to separate. This effect is particularly problematic for thin laser-cut metal parts due to their clean edges and smooth surfaces. The issue worsens when sheets are positioned lower in a stack, as they bear the weight of the sheets above them. This added pressure forces more air out from between the sheets, further strengthening the vacuum and increasing the sticking problem.

Residual magnetism can also add to the destacking problem. In real-world cases, metal parts have been observed to become magnetically charged after passing through certain machines. For instance, the destacking problem worsened every time the sheets went through a deburring machine, suggesting that residual magnetism was increasing their tendency to stick together. Magnetically charged sheets attract each other, further worsening the sticking effect.

3.5 Potential approaches to a solution

Industry professionals were asked to share their thoughts on potential approaches that could improve destacking efficiency and reliability. These proposed solutions are examined to identify promising strategies that could be further developed to address the destacking issue.

An important aspect of an effective solution for the destacking problem is the inclusion of a double-sheet detection system. Even very good solutions are unlikely to succeed one hundred percent of the time. Therefore, the system should be capable of detecting when a pickup fails, allowing the process to stop before any damage occurs. Without such a detection system, the robot must always assume the worst-case scenario, significantly increasing cycle times.

Vacuum effectors in combination with a peeling motion (bending the product downward in the middle) are considered a promising approach for successful destacking. Unlike magnetic effectors, vacuum effectors are not limited to ferritic sheet materials and do not have a magnetic penetration depth that attracts multiple products. One challenge with vacuum effectors is the potential loss of pressure when picking up products with holes. However, magnetic effectors also experience a reduction in attractive force in these cases. Proper effector positioning can help prevent vacuum pads from attaching to holes in the first place.

Bending the top product has been found to be particularly effective for large products. However, this method may require further development for smaller, more rigid products that do not bend as much due to gravity alone. For these types of products, an alternative method might involve a third effector in the middle, positioned slightly lower than the outer two vacuum pads. This configuration forces the product to bend more, breaking the seal between the sheets.

Another potential solution involves applying vibrations to the gripper after pickup. These vibrations could help break the seal between sheets, causing any additional attached products to separate

more easily. Additionally, organizing the stack so that each product is slightly offset from the previous one could reduce the destacking problem. However, implementing this approach would require changes to earlier steps in the manufacturing process, which may not always be feasible or desirable.

3.6 Conclusion

The interviews with industry professionals provide valuable insights into the practical aspects of destacking metal sheets and the factors that contribute to the destacking problem. The respondents highlight how surface conditions, compressive forces, residual magnetism, and vacuum effects can contribute to the destacking problem. Real-world examples illustrate how these factors play a role in different scenarios, from handling large and oily sheets to dealing with residual magnetism introduced during manufacturing.

Various actions have been taken to address the issue, including new gripper designs and adjusted effector movements to induce bending in the top sheet. While some methods proved effective in specific scenarios, none offered a universal solution for all scenarios. The development of a specialized peeling gripper for a specific product type demonstrates that targeted solutions could resolve destacking problems, but adaptability remains a concern.

Several promising solutions for the destacking problem have been suggested, including the use of vacuum effectors with a peeling motion, the introduction of vibrations to break adhesion between sheets and modifying stacking arrangements. Additionally, the implementation of a reliable double-sheet detection system was deemed crucial for preventing damage and reducing cycle times.

These findings provide a practical insight into the destacking problem and its possible solutions. The information gathered with these interviews provide an answer to the first research sub-question:

- How do industry professionals experience and perceive the destacking problem?

Chapter 4

Literature analysis

4.1 Introduction

The main objective of this thesis is to optimize the automated destacking of thin metal sheets. A major challenge in this process is the destacking problem, where multiple sheets adhere to one another, disrupting the destacking operation. To develop effective solutions for this problem, it is important to understand the underlying causes of adhesion and the conditions under which it becomes problematic for destacking.

This chapter presents a literature analysis to explore the factors that cause thin metal sheets to stick together and to identify when these adhesive effects interfere with the destacking process. Additionally, existing solutions from the literature are examined to understand how this issue has been addressed in the past. By reviewing these aspects, this chapter aims to answer the following research sub-questions:

- What are the factors that cause adhesion between thin metal sheets, and under what conditions do these forces become significant?
- Under which conditions do adhesive effects influence destacking and when does this become problematic?
- What solutions to the destacking problem have been discussed in the literature?

By addressing these questions, this chapter explores the relevant literature that is available for the destacking problem.

4.2 Adhesion factors

To develop an effective solution to the destacking problem, it is essential to first identify the factors that cause adhesion between thin metal sheets. This section examines the literature to determine the key contributors to the sticking effect.

Atmospheric pressure

When separating two stacked sheets, a gap forms between them. If this gap remains sealed, preventing the internal pressure from equalizing with the surrounding air, a partial vacuum is created. The

resulting pressure difference ΔP_{atm} exerts an inward force on the boundary of this cavity, effectively pushing the sheets together. This pressure difference persists until the seal between the sheets is broken, allowing the air to equalize. The strength of this seal is influenced by factors such as surface roughness and the presence of oil coatings.

The total downward force F_{atm} on the top sheet due to atmospheric pressure is given by Equation 4.1:

$$F_{\text{atm}} = \Delta P_{\text{atm}} A \quad (4.1)$$

where:

- ΔP_{atm} [N/m²] is the pressure difference between the cavity and the surrounding air.
- A [m²] is the surface area of the sheet.

This equation follows from the definition of pressure as force per unit area [14]. The sheet area A is taken once (for the top sheet) and not twice because the atmospheric forces on the second sheet do not contribute to the downward forces on the top sheet. The force increases with both the surface area and the pressure difference. As a result, factors such as the initial volume of trapped air between sheets influence the destacking process.

Sections 4.3 and 6.2 provide a more detailed analysis of atmospheric pressure effects in stacked sheets.

Capillary forces

Stacks of thin metal sheets often contain a thin layer of corrosion-resistant oil to prevent rusting. A liquid between two solids can form a liquid bridge, as was described in Section 2.3. Such a liquid bridge can form between thin metal sheets if they contain a corrosion-resistant oil, creating an adhesion force [3]. This force arises due to capillary effects and surface tension. Figure 4.1 shows an example of a liquid bridge between two sheets. In this figure, l and w are the length and width of the sheets, d is the distance between the sheets, θ is the interface contact angle and r_1 is the principal radius of the liquid bridge.

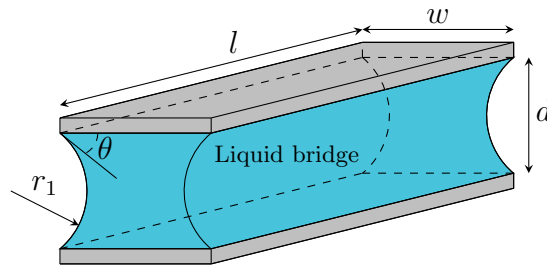


Figure 4.1: Liquid bridge between two sheets.

For larger liquid volumes, gravitational forces can influence the shape of the interface curvature. However, this effect can be neglected when the characteristic size L of the liquid bridge is much smaller than the capillary length l_{cap} : $L \ll l_{\text{cap}}$ [15]. For a liquid bridge, the characteristic size is the length of the liquid bridge (the distance between the two solid surfaces). The capillary length can be calculated using Equation 4.2.

$$l_{\text{cap}} = \left(\frac{\gamma}{g\Delta\rho} \right)^{1/2} \quad (4.2)$$

where:

- γ [Nm^{-1}] is the liquid-vapour surface tension.
- g [ms^{-2}] is the gravitational acceleration.
- $\Delta\rho$ [kgm^{-3}] is the density difference between the liquid and the vapour.

As was discussed in section 2.3, the pressure difference $\Delta P_{\text{Laplace}}$ between the liquid bridge and the surrounding air results in an attractive force. For a liquid bridge between two stacked sheets, this Laplace force F_{Laplace} on the top sheet is equal to the pressure difference times the area of the sheet A , as can be seen in Equations 4.3 and 4.4.

$$\Delta P_{\text{Laplace}} = \gamma \left(\frac{1}{r_1} + \frac{1}{r_2} \right) \quad (4.3)$$

$$F_{\text{Laplace}} = \Delta P_{\text{Laplace}} A \quad (4.4)$$

Section 2.2 explained how the interface between a liquid and a gas generates surface tension, which acts along all edges of the surface. Figure 2.2 in Section 2.2 illustrated how this tension pulls on the edges of a liquid-vapour surface. Similarly, the liquid in Figure 4.1 has a liquid-vapour surface that exerts a pulling force on its edges. As can be seen from the geometry in this figure, the contribution of this tension to the adhesion forces depends on the interface angle θ . This contribution decreases as the angle decreases, reaching its maximum at 90° and dropping to zero at 0° . Therefore, this dependence is modelled using a sine function: $\sin(\theta)$.

Since surface tension acts downward along the edges of the top sheet, its effect scales with the edge length. For the geometry in Figure 4.1, the total edge length of the top sheet is $2l + 2w$, where l and w are the length and width of the sheet, respectively. As explained in Section 2.2, the liquid-vapour surface tension strength γ depends on the specific liquid-vapour combination. The resulting component of the surface tension that contributes to the downward force on the top sheet, F_{tension} , is given in Equation 4.5.

$$F_{\text{tension}} = (2l + 2w)\gamma \sin(\theta) \quad (4.5)$$

The total capillary adhesion force on the top sheet is the sum of the Laplace force and the pulling force of the surface tension, this can be seen in Equation 4.6.

$$F_{\text{cap}} = \gamma \left(\frac{1}{r_1} + \frac{1}{r_2} \right) A + (2l + 2w)\gamma \sin(\theta) \quad (4.6)$$

Residual magnetism

When an external magnetic field is applied to a ferromagnetic material, the small magnetic domains within the material align, resulting in a net magnetisation. The magnetisation that remains after the external field is removed is known as residual magnetism or remanence. The strength of this residual magnetism depends on both the applied field and the retentivity of the material [16].

In the sheet metal industry, lifting magnets are commonly used to handle parts. However, the use of strong magnets on ferromagnetic components can induce significant residual magnetism [17]. In manufacturing, this residual magnetism can lead to several issues, including:

- Parts sticking together.
- Welding complications due to deflection of the welding arc.
- Attraction of metal dust and shavings.
- Unintended adhesion of parts to machinery.
- Increased wear on bearings.

Stacked metal sheets containing residual magnetism attract each other. The magnetic force between two parallel magnetic surfaces can be determined using Equation 2.3 from Section 2.4. This equation assumes the magnets have infinitely high permeability and that the magnetic field between them is uniform. In practice, however, the magnetic field is not uniform, causing the magnetic force to decrease with distance. This relationship is more complex and depends on the geometry. Nevertheless, the equation remains useful for estimating the maximum magnetic force in stacked sheets with residual magnetism.

Triboelectric effect

Most people have likely experienced a mild static shock when touching a metal doorknob. This phenomenon is caused by the triboelectric effect, in which electrical charge is transferred between two surfaces when they come into contact and are then separated again [18]. A common example occurs when walking across a rug. Charge is then accumulated in the body and subsequently released upon touching a conductive object such as a doorknob. This process is referred to as the redistribution of static charges [19].

During the handling and processing of thin metal sheets, there are numerous opportunities for the triboelectric effect to induce static charges. However, because the sheets are made of a conductive material, any relative charge differences between stacked sheets tend to redistribute rapidly, reducing the likelihood of significant attractive or repulsive forces between them. The triboelectric effect may only have a notable influence in cases where the product includes a protective plastic film or is coated with oil or paint.

Metal-to-metal adhesion forces

Metal-to-metal adhesion forces can play a significant role in the sticking of thin metal sheets that are smooth and clean [20]. The surface roughness of the sheets influences these adhering forces since a smooth surface will have more points of contact between the two sheets. A smooth surface will therefore experience more of these adhering forces than a rough surface.

Surface contamination reduces the adhesion between metal parts. Even minute layers of surface oxidation, grease or other types of contamination can significantly reduce adhesion for smooth surfaces. Experimentation on metal-to-metal surface adhesion between metals was done by M.E. Sikorski [20]. In these experiments, surface adhesion was detected after mechanical polishing down to 0.1 μm diamond particle size. Unless the samples were also vapor-decreased, the adhesion between the metal samples was undetectable. This level of surface smoothness and cleanliness will not be applicable for the application of this research. However, the samples used by M.E. Sikorski have a contact area of 1.27 cm^2 whereas metal sheets in the application of this research can easily have a contact area of 1000 cm^2 . Adhesion forces that were undetectable for M.E. Sikorski could be relevant for this project due to the larger area. However, this is not very likely because the test products used in this thesis are not as smooth as the products used by M.E. Sikorski.

Conclusion

To investigate the factors that cause adhesion between thin metal sheets, this section examines the various forces that can act on the sheets. The primary forces identified include atmospheric pressure, capillary forces, residual magnetism, triboelectric effects, and metal-to-metal adhesion. The second research sub-question is:

- What are the factors that cause adhesion between thin metal sheets, and under what conditions do these forces become significant?

This section addresses the first part of this question by exploring the various factors contributing to the adhesion between thin metal sheets. Section 4.3 will address the second part by calculating the total adhesion forces acting on stacked sheets.

4.3 Destacking problem

Section 4.2 identified the main factors contributing to adhesion between thin metal sheets. Building on these insights, this section examines how these factors influence the destacking problem. Each factor is evaluated for its significance in causing adhesion, and for those factors that have a substantial impact, adhesion forces are calculated.

Test products

Test products are needed to perform destacking experiments and calculations. Two thin metal sheet products were selected for this purpose. The two test products, their weights and their dimensions are shown in Figure 4.2. Two test products of different sizes were chosen to see the difference in the sticking effect between the two product sizes.

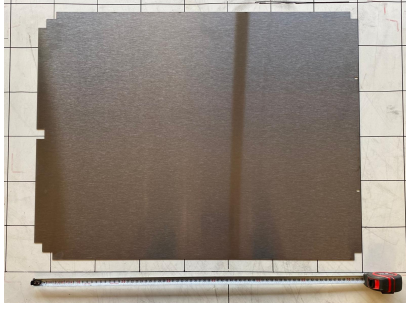
To determine the initial volume of air between stacked test products, the total thickness of a stack was first measured. This was measured at five locations to calculate the average stack height. Similarly, the thickness of a single sheet was also measured at five locations. The average stack height was then compared to the sum of the average sheet heights. The difference, divided by the number of gaps in the stack, gives an average gap distance of 0.013 mm between two sheets. This average gap distance is combined with the sheet area to calculate the initial volume between sheets that can be seen in Figure 4.2.

Atmospheric pressure

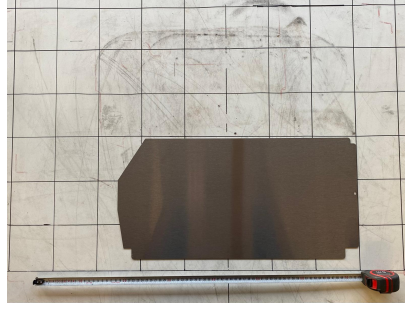
A partial vacuum can be created underneath the sheet during destacking as long as the seal remains intact, as was discussed in Section 4.2. The downward force on the top sheet due to the atmospheric pressure is equal to the pressure difference times the area of the sheet, as can be seen in Equation 4.7.

$$F_{\text{atm}} = \Delta P_{\text{atm}} A \quad (4.7)$$

The areas A of test product one and two are 0.417 m^2 and 0.153 m^2 respectively. The pressure difference ΔP_{atm} depends on the amount of air that is trapped in between the sheets, and the volume increase of this airgap. The standard atmospheric pressure is taken to be about 100 kPa [21]. When we assume that a partial vacuum of 50% is reached before the seal breaks, the pressure difference is 50 kPa.



- Test product one
 - Weight = 2.294 kg
 - Length = 73.6 cm
 - Width = 56.7 cm
 - Thickness = 0.9 mm
 - Area = 0.417 m²
(approximated as rectangle)
 - Initial volume between sheets
= 5.421×10^{-6} m³



- Test product two
 - Weight = 0.990 kg
 - Length = 55.4 cm
 - Width = 27.6 cm
 - Thickness = 1.0 mm
 - Area = 0.153 m²
(approximated as rectangle)
 - Initial volume between sheets
= 1.989×10^{-6} m³

Figure 4.2: Test products one and two.

This results in a downward atmospheric force of $F_{\text{atm}} = 50\,000 \text{ Pa} \cdot 0.417 \text{ m}^2 = 20\,850 \text{ N}$ for test product one. Similarly, this results in an atmospheric force of 7650 N for test product two. This is equal to a weight of 2125 kg and 780 kg that pushes down on test product one and two respectively.

Even if only a partial vacuum of 10% would be achieved, the resulting force of 4170 N (425 kg) and 1530 N (156 kg) for test product one and two would still be significant compared to the weight of these sheets (2.294 kg and 0.990 kg). It can therefore be concluded that the atmospheric pressure and the seal strength between sheets will play a crucial role in the destacking problem.

Capillary forces

As discussed in Section 4.2, a layer of liquid, such as corrosion resistant oil, between stacked sheets can form a liquid bridge. A liquid bridge between two parallel plates results in attractive capillary forces caused by the Laplace pressure and the surface tensions.

To determine if the gravitational force will influence the shape of the liquid bridge, the characteristic size L needs to be compared to the capillary length l_{cap} . If the characteristic size is much smaller than the capillary length ($L \ll l_{\text{cap}}$), the effect of gravity on the liquid shape can be neglected.

The characteristic size for liquid bridges is the distance between the two solid bodies. The measured average distance between test product sheets is 0.013 mm, as is discussed in Section 4.2. This distance is taken for the characteristic size L for this calculation.

The liquid-vapour surface tension γ between machine oil and air is 0.032 Nm^{-1} [22]. The acceleration due to gravity g is equal to 9.81 ms^{-2} . The difference between the liquid and vapour densities $\Delta\rho$ is equal to 877.41 kgm^{-3} since the density of machine oil is 878.7 kgm^{-3} [23] and the density of air is 1.29 kgm^{-3} [24]. Using Equation 4.2, this gives a capillary length l_{cap} of 1.93 mm.

With these values for L and l_{cap} , it can be concluded that the influence of gravity on the curvature

of the liquid-vapour interface is negligible for this case since the characteristic size ($L = 0.013$ mm) is less than the capillary-length ($l_{\text{cap}} = 1.93$ mm) [15]. For liquid-vapour interfaces where the influence of gravity can be neglected, the Young-Laplace in Equation 4.3 can be used to calculate the pressure difference across the interface.

The total capillary force can be seen in Equation 4.8 and was also discussed in Section 4.2. For a liquid bridge between two sheets, the second radius of curvature r_2 becomes infinity because the edges are straight. The pressure difference across the interface therefore becomes: $\Delta P_{\text{Laplace}} = \frac{\gamma}{r_1}$.

If a corrosion resistant oil covers the complete sheet surface with a thin film, it will have a high wettability. This means that it will have a low contact angle. Otherwise, with a low wettability, the oil would form droplets and not protect the metal sheet. In this approximation the contact angle of the oil is assumed to be zero. If it is assumed that the contact angle is zero, the principal radius r_1 is half the distance between the sheet, as can be seen in Figure 4.1. The distance between the sheets is again taken to be the measured value from Section 4.2: 0.013 mm. This gives a principle radius r_1 of 0.0065 mm.

$$F_{\text{cap}} = \gamma \left(\frac{1}{r_1} + \frac{1}{r_2} \right) A + (2l + 2w)\gamma \sin(\theta) \quad (4.8)$$

Using the above mentioned values for the principle radius, surface tension, contact angle, sheet distance, sheet length and sheet width in Equation 4.8, a value of 2053 N and 753 N is obtained for test product one and two respectively.

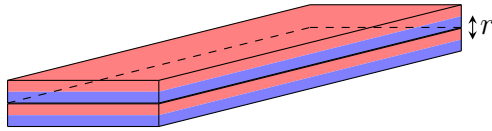


Figure 4.3: Stacked parts that contain residual magnetization.

Residual magnetism

Figure 4.3 shows two stacked parts that contain residual magnetism. The north poles of the parts are indicated in red and the south poles are indicated in blue. Equation 2.3 can be used to estimate the magnetic force between these parts.

The following parameters are known:

- A magnetometer (also called a Gaussmeter) can be used in practice to measure the residual magnetic field of a part [25]. Measurements with these instruments are expressed in Gauss or Tesla. For this example, a magnetic flux density of 0.01 T is taken. This value is taken because 0.01 T of residual magnetism can already be induced in a part after the use of handling magnets [17].
- The sheet dimensions from test product one and two in Figure 4.2 are used for this calculation.
- The magnetic permeability of free space is a constant [26]: $\mu_0 = 4\pi \cdot 10^{-7} \text{ NA}^{-2}$.

Using these parameter values in Equation 2.3 results in a magnetic force of 16.6 N and 6.1 N for test product one and two respectively. From Equation 2.3 it becomes clear that the magnetic flux density B between the metal parts is strongly related to the magnetic force between the thin metal sheets. This flux density depends on the magnetic field strengths that the part has previously been

in contact with [17]. The significance of residual magnetism as an adhering factor between thin metal sheets will therefore depend on the magnetic handling that was done to the parts prior to stacking.

Triboelectric effect

The triboelectric effect can result in adhering forces between metal sheets due to static charges. However, for most industrial applications, the conducting metal sheets will redistribute their electric charges when stacked. It is therefore assumed that static charges do not play a major role in the destacking problem.

Metal-to-metal adhesion

Metal-to-metal adhesion forces can result in attractive forces if the surfaces are very smooth and clean. It is assumed that these forces will not play a significant role in the destacking problem. This is assumed because the metal sheets in an industrial setting will not be smooth to the micron scale and also not be completely contamination free. These factors are however required for these metal-to-metal adhesion forces to become significant [20].

Use of effectors

The use of magnetic effectors can significantly contribute to the destacking problem. For example, an 40 mm diameter magnetic gripper will exert about 105 N on a 1 mm thick steel plate with an airgap of 1 mm between the magnet and the sheet [27]. This force is expected to be higher if the airgap was not filled with air but with another steel plate since the permeability of carbon steel is about one hundred times higher than the permeability of air [28]. The permeability of a medium quantifies the magnetization in a material in response to an external magnetic field [29].

Using two of these grippers to destack 1 mm thick metal sheets will therefore result in an adhering force in the range from 150 to 250 N on the second metal sheet. Even using smaller 24 mm diameter magnets from the same supplier will result in an adhering force in the range of 20 to 40 N on the second 1 mm sheet following from the same reasoning [30]. This is considerably less but it also sacrifices 79% of the holding force on the top part.

Conclusion

The adhesive forces resisting the separation of two stacked sheets act downward on the top sheet (resisting lifting) and upward on the second sheet (pulling it up). These forces can be expressed as the sum of atmospheric pressure force F_{atm} (Equation 4.1), capillary force F_{cap} (Equation 4.6), and the magnetic force F_{mag} due to residual magnetism (Equation 2.3). Triboelectric and metal-to-metal adhesion forces can be neglected for typical industrial sheet metal applications due to material conductivity and surface roughness, respectively.

Sticking becomes problematic when the adhesive forces acting on the second sheet exceed the gravitational force pulling it down. This sticking condition is given by:

$$F_g < F_{\text{atm}} + F_{\text{cap}} + F_{\text{mag}}$$

$$mg < 2\Delta P_{\text{atm}}A + \gamma \left(\frac{1}{r_1} + \frac{1}{r_2} \right) A + (2l + 2w)\gamma \sin(\theta) + \frac{B^2 A}{2\mu_0} \quad (4.9)$$

This analysis focuses exclusively on the interaction between two sheets, as stated in Section 1. While adhesive forces between the second and third sheets may also contribute, they are not considered here.

Table 4.1 summarises the magnitude of each adhesive force for the two test products in Figure 4.2.

Table 4.1: Comparison of adhesion forces acting on sheets during destacking

	Test product one	Test product two	Notes
F_{atm}	20 850 N	7650 N	50% partial vacuum in cavity
F_{atm}	4170 N	1530 N	10% partial vacuum in cavity
F_{cap}	2053 N	753 N	For machine oil – air surface tension
F_{mag}	16.6 N	6.1 N	Residual magnetism of 0.01 T
$F_{\text{triboelectric}}$	-	-	Negligible due to sheet conductivity
$F_{\text{metal-to-metal}}$	-	-	Negligible due to surface roughness
F_{effector}	-	-	Not applicable for vacuum effectors

By determining the contribution of each force to the sticking condition, this analysis answers the third research sub-question:

- Under which conditions do adhesive effects influence destacking and when does this become problematic?

4.4 Solutions in literature

This section discusses existing approaches to the destacking problem to understand how researchers and industry professionals have addressed this challenge in the past.

Double sheet detection

One approach to the destacking problem is to detect when multiple products have been destacked at once. This approach does not solve the source of the problem but it does mitigate the consequences, because it can stop the production process when two sheets have been destacked at once. Ultrasonic transducers are often used to detect the double sheets [31]. These transducers send out an ultrasonic signal and can calculate the distance to a flat surface by measuring the time of flight of the echoing sound signal. By placing one of these sensors above and one below the sheet, the thickness of the sheet can be measured. This setup can also be used to detect a double sheet, if the measured thickness is double the expected thickness. An example for such a double sheet system for paper sheets can be seen in Figure 4.4.

Magnetic sheet separator

Another approach to the destacking problem is the use of magnetic sheet separators. These are devices that are able to vertically fan out a stack of products, allowing for destacking without double sheet pickups. An example of an industrial magnetic sheet separator can be seen in Figure



Figure 4.4: Ultrasonic double sheet detection system for paper sheets [32].

4.5. This sheet separator is placed on one side of the stack and can be toggled on or off. It is also possible to place another magnetic sheet separator on the other side of the stack to prevent the sheets from tilting.

The magnetic sheet separator is just a horizontally polarized strong magnet that is placed on the side of a stack. Due to the horizontal polarization, the complete side of the stack is magnetized with the same magnetic pole. This causes the magnetized sheets to repel each other, resulting in the fanning effect.

A disadvantage of magnetic sheet separators is that it has to be placed on the side of the stack. This means that the edge of the stack should always be in the same position, which reduces flexibility.



Figure 4.5: Industrial magnetic steel sheet separator [33].

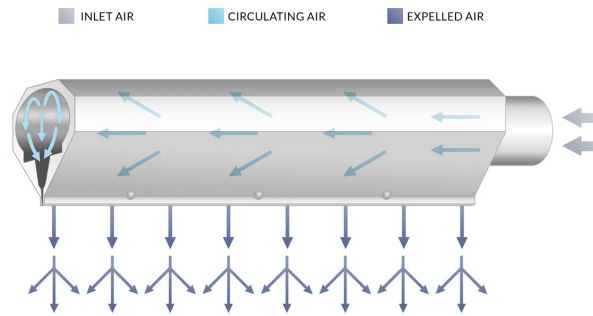


Figure 4.6: Schematic drawing of an air knife [34].

Air knife

Compressed air can also be used to break the seal between two sheets, this can be done using so-called 'air-knives'. Air knives work by blowing air in a compartment that is designed to circulate the air. The high pressure air can only exit this compartment through a narrow slit, resulting in a high exit velocity. This high-velocity air is then used to break the seal between stacked products. A schematic drawing of an air knife can be seen in Figure 4.6.

Bending moment

Bending the edges of the top product upward is one way to break the seal between the two sheets. One way of achieving this, is by gripping the corners of the top product and bending them upward. An example of a magnetic end effector that uses this approach can be seen in Figure 4.7 [35]. This device uses magnetic grippers that can be rotated outward. This rotation is actuated by side-mounted air cylinders. By rotating the magnetic effectors outward, the attached sheets will bend downward which induces a bending moment. Consequently, when enough bending moment is induced, the second sheet will peel off while the top sheet remains attached to the magnets.

A disadvantage of this approach is that the sheet needs to be picked up at the edges in order to induce enough bending moment in the sheets. An advantage of this approach is that the destacking tool is incorporated into the handling tool, omitting the need for a separate destacking tool.

Mechanical peeling

Another method for separating thin metal sheets from a stack is to mechanically peel the top part from the stack. One example of such an approach can be seen in Figure 4.8. This figure is from a patent for a destacking device that uses a screw-shaped separator device [36]. The threads of this device grip in between stacked sheets and lift them up from the stack.

Conclusion

In analysing existing solutions, various methods such as double-sheet detection, magnetic sheet separators, air knives, bending moments and mechanical peeling were examined. Double-sheet detection does not mitigate the sticking issue but it does prevent undesirable consequences from the destacking problem. Other solutions such as magnetic sheet separators, air knives and mechanical peeling often require a destacking setup that is designed for one specific product. Given this limitation, there is a

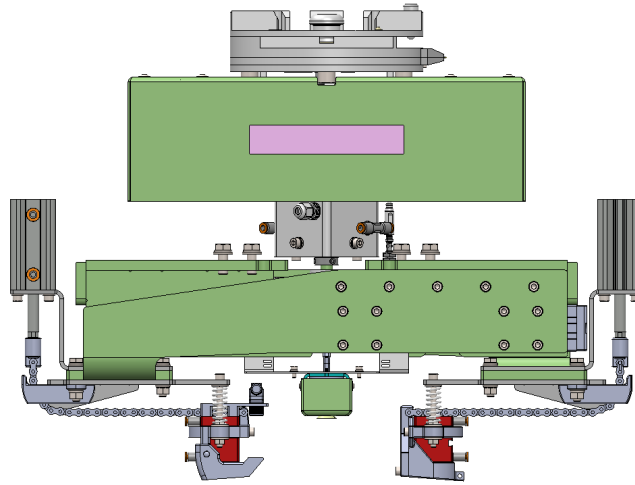


Figure 4.7: End effector design that utilizes rotatable magnets to induce a bending moment in the top product [35].

need for a more general destacking solution that can handle a larger variety of products. Examining the solutions to the destacking problem that have been discussed in literature answers the fourth research sub-question:

- What solutions to the destacking problem have been discussed in the literature?

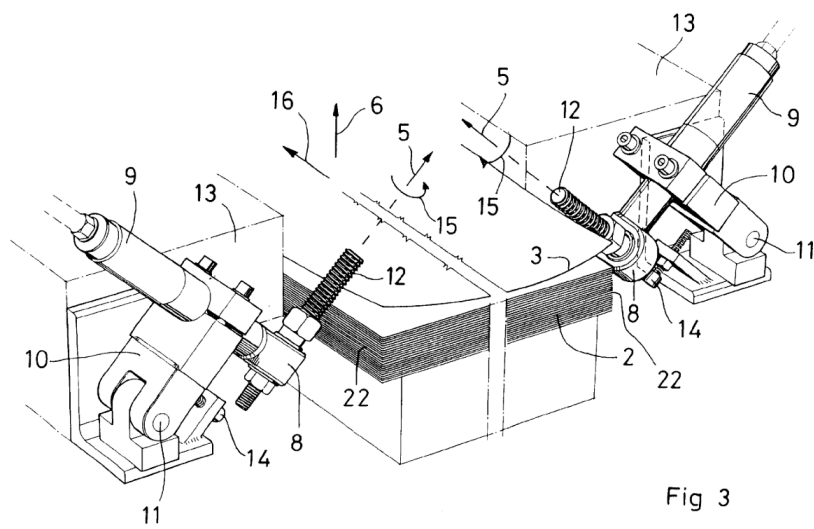


Fig 3

Figure 4.8: Patented device for mechanically destacking the top sheet from a stack using angled screws [36].

Chapter 5

Preliminary experiments

5.1 Introduction

During the destacking process, various forces act on the products. Section 4.2 discussed all potentially relevant forces, while Section 4.3 introduced the following sticking condition:

$$F_g < F_{\text{atm}} + F_{\text{cap}} + F_{\text{mag}} \quad (5.1)$$

This chapter applies the equations from Section 4.3 to predict the maximum pulling force required for destacking. The calculated pulling forces are then compared with experimental results to assess the extent to which these initial estimates reflect reality.

5.2 Hypothesis

The test products that are described in Section 4.3 are used in these preliminary experiments. These test products do not contain corrosion-resistant oils and do not contain any residual magnetism. This means that the adhesion effects of the capillary and magnetic forces can be neglected. This results in the sum of forces F_{tot} that can be seen in Equation 5.2. This sum of forces acts on the top sheet of a stack during destacking in the downward direction.

$$F_{\text{tot}} = F_g + F_{\text{atm}} = mg + \Delta P_{\text{atm}} A \quad (5.2)$$

Test product one has a mass of 2.294 kg, and test product two has a mass of 0.990 kg resulting in a gravitational force of 22.5 N and 9.71 N respectively. The area of test product one is 0.417 m² and the area of test product two is 0.153 m², as was given in Figure 4.2. The maximum pressure difference ΔP_{atm} between the atmospheric pressure and the pressure in the cavity between the sheets is determined by the vacuum percentage created as the top sheet is separated. Since the strength of the seal between the sheets depends on various physical factors such as surface roughness, cleanliness, and the stacking process, accurately predicting the maximum vacuum percentage before the seal breaks is challenging.

For the purpose of this calculation, a build-up of 10% partial vacuum before the seal breaks is assumed. This corresponds to a pressure difference of 10 kPa, given that atmospheric pressure is approximately 100 kPa. Using the values above in Equation 5.2, the maximum pulling force for test products one and two calculated to be 4193 N and 1540 N respectively.

Hypothesis: using a vacuum handling effector, the required pulling force to destack test product one and two is 4193 N and 1540 N respectively.

5.3 Experimental design and setup

In order to measure the maximum destacking pulling force, a device is required that includes a vacuum pad, can measure and log its pulling force over time, and can be attached to a robotic manipulator. The device shown in Figure 5.1 was developed for this purpose. It features a vacuum pad measuring 11.5 cm by 11.5 cm, a pneumatic vacuum generator, a Zemic H3-C3-100kg-3B load cell, and a chain connected to a zero-point clamping bolt, which allows attachment to the robotic manipulator. The manipulator used in this experiment is the ABB Articulated Robot IRB 6700.



Figure 5.1: Destacking device that uses a 11.5 cm by 11.5 cm vacuum pad and can be used to measure and log the pulling force over time.

This assignment focuses exclusively on the destacking behaviour of two thin metal sheets, as discussed in Chapter 1. However, if the adhesion forces are greater than the gravitational forces, the second sheet will stick to the top sheet. This prevents the destacking device from Figure 5.1 from measuring the maximum adhesion forces between the sheets, as it will instead only measure the combined gravitational forces of both sheets.

To ensure that the second sheet remains fixed to the ground, allowing accurate measurement of the maximum adhesion forces, a fixture device was developed. This device, shown in Figure 5.2, includes a 50 cm by 25 cm vacuum pad, a pneumatic vacuum generator, and a wooden pallet. When a product is placed on this device and the vacuum generator is activated, the suction force of the vacuum pad holds the product firmly in place.

Control measurements

Performing a destacking measurement using the destacking device shown in Figure 5.1 results in a maximum pulling force for each measurement. In order to analyse the contribution of adhesion forces to this maximum pulling force, the contribution of the gravitational force must be known. Although the weight of the test products is already known, control measurements were conducted to eliminate potential inaccuracies arising from manual load cell calibrations.



Figure 5.2: Fixture device that uses a 50 cm by 25 cm vacuum pad and can be used to fix a product in place and prevent sticking.

In these control measurements, a single test product is placed on a standard EUR-pallet. The destacking device is then positioned at the centre of the product. After switching on the vacuum generator, the destacking effector is moved upward slowly (at a speed of less than 1 mm s^{-1}) and at a constant rate. A picture of the experimental setup can be seen in Figure 5.3. Note that this picture shows a stack of test products, only one test product was used at a time for the control measurements. The pulling force is logged over time until it stabilises at a constant value. The resulting plots of pulling force over time for the control measurements of test products one and two are shown in Figures 5.5a and 5.5b.



Figure 5.3: Experimental setup including the robotic manipulator, the test product, the destacking device from Figure 5.1 and a laptop for logging measured values.

Destacking measurements

The goal of the destacking measurements is to determine the contribution of adhesion forces to the overall destacking force, assuming that only the top sheet is picked up. A stack of two products is used for these measurements. To ensure that the second product does not adhere to the top product, the fixture device shown in Figure 5.2 is used. Apart from the use of the second product and the fixture device, the destacking measurements follow the same procedure as the control measurements.

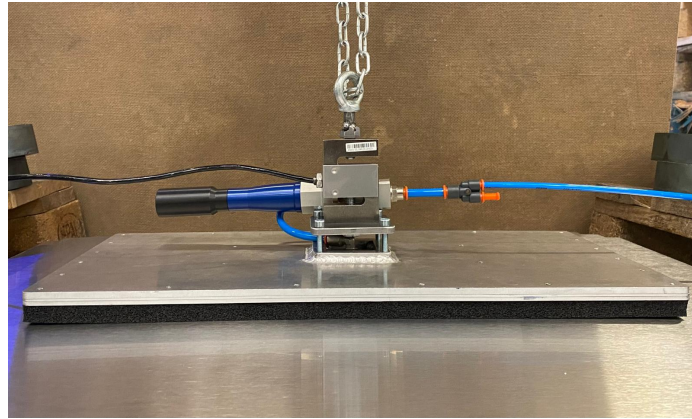


Figure 5.4: Destacking device equipped with a 50 cm by 25 cm vacuum pad, capable of measuring and logging the pulling force over time.

During testing, the vacuum forces generated by the 11.5 cm by 11.5 cm vacuum pad were insufficient to destack test product one. To increase the vacuum strength, the destacking device was fitted with a 50 cm by 25 cm vacuum pad, as shown in Figure 5.4. The plots of the pulling force during the destacking measurements for test products one and two are shown in Figures 5.5c and 5.5d, respectively. The destacking measurement for test product one was conducted using the large vacuum pad from Figure 5.4, while the measurement for test product two was carried out using the small vacuum pad from Figure 5.1.

5.4 Results

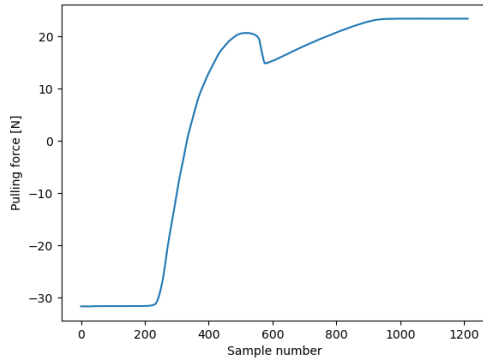
The control measurement of test product one is shown in Figure 5.5a. This measurement reached a maximum pulling force of 23.4 N, which corresponds to 2.39 kg. This is 96 g more than the weight of 2.294 kg stated in Figure 4.2, which was measured using an industrial scale (Salter Brecknell B820).

The destacking measurement of test product one is shown in Figure 5.5c. In this case, the maximum pulling force at which the top sheet separates from the second sheet was not reached. The measurement was stopped prematurely because the pulling force approached the maximum capacity of the load cell, which is 100 kg (981 N). This force is at least 957.6 N larger than the control measurement, the actual difference between the two will be larger.

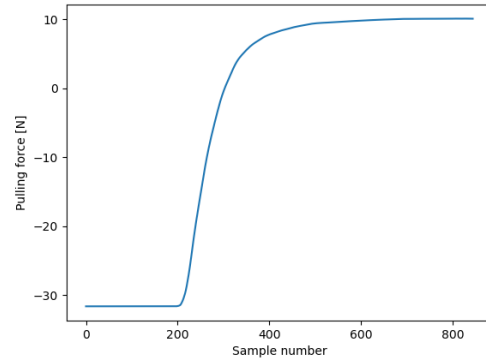
The control measurement of test product two is shown in Figure 5.5b. This measurement reached a maximum pulling force of 9.90 N, corresponding to 1.01 kg. This is 20 g more than the measured weight of 990 g stated in Figure 4.2.

The destacking measurement of test product two is shown in Figure 5.5d. This measurement reached a maximum pulling force of 10.1 N (1.03 kg). This force is 0.20 N larger than the control

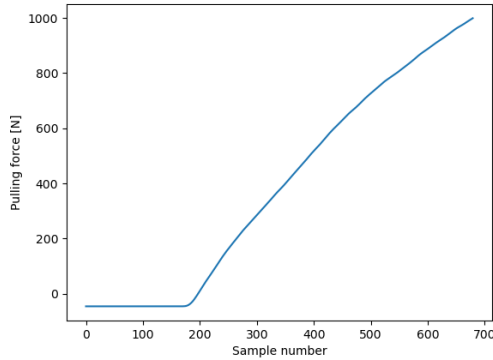
measurement.



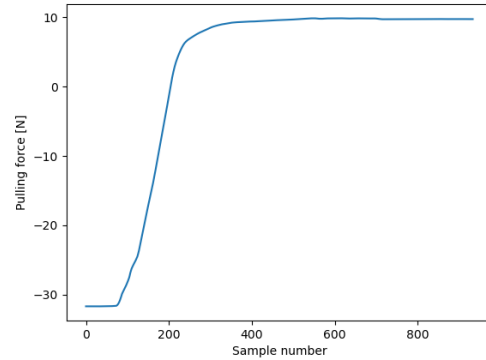
(a) Test product one: control measurement



(b) Test product two: control measurement



(c) Test product one: destacking using large vacuum pad



(d) Test product two: destacking using small vacuum pad

Figure 5.5: Measured pulling force for the control measurement of test product one and two (a and b), and for the destacking measurement of test product one and two (c and d).

5.5 Conclusion

The difference between the measured product weights and the control measurements is 96 g for test product one and 20 g for test product two. Both values indicate an acceptable calibration of the load cell for the purposes of these measurements.

The adhesion force between two sheets of test product one is at least 957.6 N, as this is the difference between the control measurement and the highest measured value during the destacking test. This force is lower than the value predicted by the hypothesis in this chapter, which estimates a force of 4193 N. However, the measured values for test product one are insufficient to reject the hypothesis, as the actual adhesion force could be higher than the measurement. A load cell with a higher capacity was not available for this assignment. To conclusively accept or reject the hypothesis for test product one, a higher-capacity load cell would be required.

The adhesion force between two sheets of test product two is 0.20 N, based on the difference

between the control measurement and the destacking measurement. This difference is negligible, suggesting that no partial vacuum was formed beneath test product two during destacking. This result contradicts the hypothesis for test product two, which predicts an adhesion force of 1540 N. One possible explanation for the absence of adhesion force is the smaller size of test product two. The effector is positioned significantly closer to the product edge in this case compared to test product one. This shorter distance may contribute to immediate seal breakage between the sheets during lifting.

Chapter 6

Model development and validation

6.1 Introduction

The main research question asks how the critical factors in the destacking process can be optimised. As discussed earlier, double-sheet pickups often occur when a seal forms beneath the top sheet, creating a partial vacuum. Developing a model to predict the deflection of thin metal sheets during destacking provides valuable insights into these factors and their optimisation.

A predictive model is particularly useful as it allows for the prediction of double sheet pickups, enabling manufacturers to optimize effector placement on products for minimizing the destacking problem. Additionally, it provides a structured approach to understanding the sticking effect. To be practical, such a model should balance accuracy and efficiency, it should be precise enough to predict the sticking effect while minimizing computational demands. In order to contribute to a practical solution to the destacking problem, the model should be able to be integrated into destacking processes.

This chapter presents the development and validation of two models that simulate the deflection of thin metal sheets during destacking. Section 6.2 outlines the development of the cross-sectional model, a statics-based approach that applies Euler–Bernoulli beam theory to approximate the deflection of the sheet’s cross-section. Section 6.3 describes the development of the FEM model, a Finite Element Model that utilises the Pynite Python package to approximate sheet deflection in three dimensions. The performance of both models is evaluated in Section 6.4, which details the experimental setup used to assess their predictive accuracy. Finally, Section 6.5 summarises the findings from both the models and experimental results.

All calculations and plots in this chapter are performed using the Python programming language, chosen for its ease of implementation and open-source nature, making it readily integrable into destacking algorithms without additional costs.

6.2 Cross-sectional model development

A predictive sheet deflection model can be used to predict double-sheet pickups if it can accurately reproduce destacking behaviour. This section explains the construction of the cross-sectional model. First, the assumptions and simplifications underlying the model are discussed, followed by the derivation of the model. The validation of this model is discussed in Section 6.4.

Assumptions and simplifications

Validation experiments will not be conducted using magnetic effectors, so magnetic contributions from the effectors to the destacking problem can be neglected.

The vacuum pads that are used in the validation experiments have a maximum holding force. The experiments are however conducted in the operating range of the pads, so this maximum holding force will not be taken into account in the mathematical model.

It is clear from the interviews with the industry professionals that multiple products can stick to the top product during destacking. It was however chosen to only model one sheet to reduce the complexity of the mathematical model. The rest of the stack is assumed to remain stationary. Figure 6.1 shows the destacking process at four points in time. It can be seen in this figure that the seal is assumed to break once it starts to tilt at one of its edges.

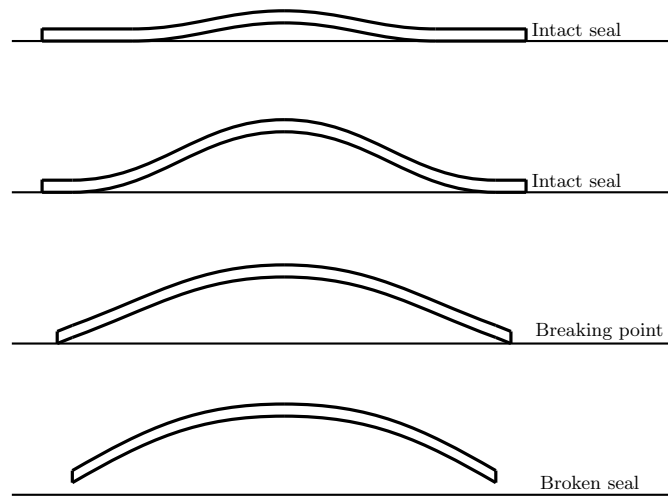


Figure 6.1: The seal is considered broken when the top sheet starts to separate from the stack around its edges.

As the robotic manipulator moves upward, the pulling force exerted by the vacuum effector increases. This increase in pulling force results in a deformation of the top sheet. The top sheet deforms upward which causes the cavity volume beneath the top sheet to expand, as can be seen in the first two figures in Figure 6.1. This expanding cavity volume increases the pressure difference with the surrounding air. The sheet is deformed due to this pressure difference, the normal forces from the second sheet, the gravitational force acting on the sheet and the pulling force from the robot. A mathematical model is needed to combine these forces and calculate the resulting sheet deflection.

The Euler-Bernoulli beam theory describes the deflection of loaded beams [9]. This theory can be used to calculate the deflection of a two-dimensional beam when all loads, boundary conditions, and beam parameters are known. The model is constructed using this theory because the separation of the sheets along their edges results from the deflection of the top sheet under the applied loads. Additionally, this theory is computationally efficient since it results in an analytical solution. Since the theory applies to two-dimensional beams, the destacking model simplifies the actual sheet deformation into a two-dimensional cross-sectional representation.

A cross-sectional view of the destacking process is shown in Figure 6.3, which will be discussed in more detail later. The bending of the sheet due to the upward movement of the effector is assumed to be radially symmetric around the contact point of the effector. This allows for the modelling of only half of the beam that is shown in Figure 6.3.

To confirm that the deflection of a sheet is indeed radially symmetric, a FEM simulation was performed using Solidworks. The deflection results of these simulations are shown in Figure 6.2. The FEM model simulates a sheet with the dimensions of test product one ($736 \times 567 \times 0.9\text{mm}$) and the Young's modulus of a steel alloy ($2.1 \times 10^{11} \text{ N/m}^2$). The sheet is suspended 10 mm above a virtual ground, representing the second sheet in the stack when the robotic manipulator has moved 10 mm upward. A rectangular area in the centre of the sheet, corresponding to the dimensions of the vacuum effector ($11.5 \times 11.5 \text{ mm}$), is fixed in place.

The sheet is subjected to a downward distributed load. This load accounts for the weight of the sheet and the atmospheric pressure, as described in Section 4.3. The net atmospheric pressure increases as the vacuum percentage underneath the top sheet increases. The plots in Figure 6.2 show the deflection results for different vacuum percentages. Plot (a) represents the deflection caused only by the weight of the sheet (0% vacuum), while Plot (f) shows the displacement for the highest simulated vacuum percentage (10%). Simulations of higher vacuum percentages were excluded due to the extreme and unrealistic sheet deflection results.

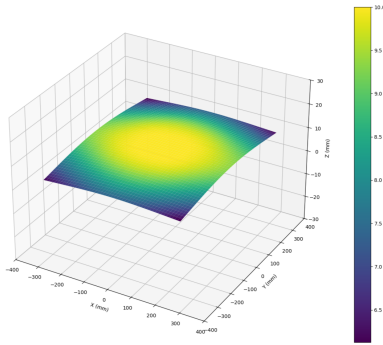
The results demonstrate that the bending of the sheet is radially symmetric around the effector location. Based on the criteria stated in Figure 6.1, the seal would be considered broken for Plots (a) to (c), and the seals in Plots (d) to (f) would be considered intact.

Mathematical formulation of the model

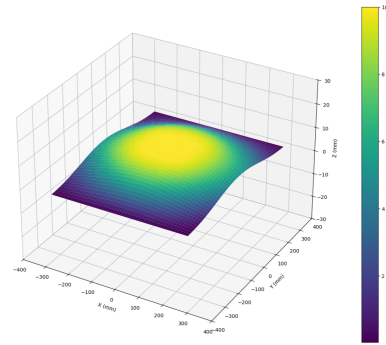
Figure 6.3 provides a cross-sectional view of a thin metal sheet during destacking. It shows a moment in the destacking process where the sheet is lifted from the middle, but the seal is still intact. This creates a partial vacuum under the sheet, which is indicated in the figure with a light blue colour. This partial vacuum results in a net atmospheric pressure that pushes down on the top sheet. The gravitational force also exerts a distributed downward load on the top sheet, both forces are drawn in blue in Figure 6.3. The upward pulling point force that acts in the middle of the sheet is drawn in red. This figure shows $2F_{\text{pull}}$ because the rest of the derivation considers only half of the cross-section, allowing for the use of one F_{pull} for these calculations. The grey s-shaped device that is attached to the vacuum pad represents the Zemic H3-C3-100kg-3B load cell that is used in the experimental validation, this is described in more detail in Section 6.4.

There is a relationship between the cavity volume beneath the top sheet and the net pressure acting upon it. As the pulling force increases, the effector moves up and the cavity volume expands. Provided the seal around the cavity remains intact, this expansion leads to a reduction in cavity pressure and therefore an increase in relative pressure on the top sheet. This rise in pressure counteracts the further expansion of the cavity. During the destacking the upward pulling force from the robot is equal to the atmospheric pressure and gravitational force action downward on the sheet.

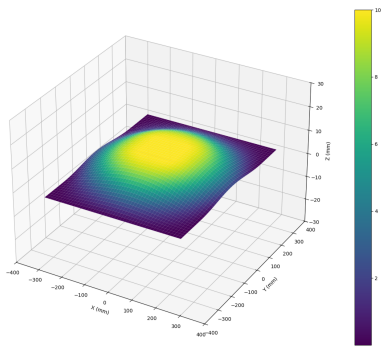
The left and right sides of the cross-section in Figure 6.3 are assumed to be symmetric, as was described earlier in this section. This enables the modelling of only one side of the cross-section. A schematic representation of this model is shown in Figure 6.4. The left end of the beam ($x = 0$) is referred to as point *A*, while the right end ($x = l$) is referred to as point *B*. The beam is subjected to a distributed downward load f and an upward force F_{pull} at point *A*. The distributed load simulates the sum of the gravitational force of the sheet F_g and the pressure difference F_{atm} due to the partial vacuum. The upward force F_{pull} at point *A* simulates half of the pulling force from the effector since



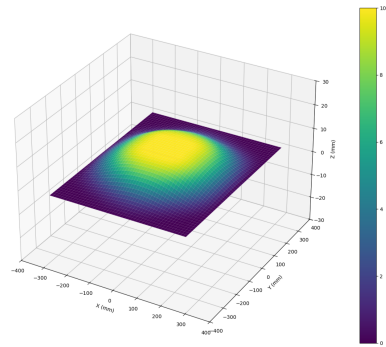
(a) Deflection top sheet for 0% of the pressure difference.



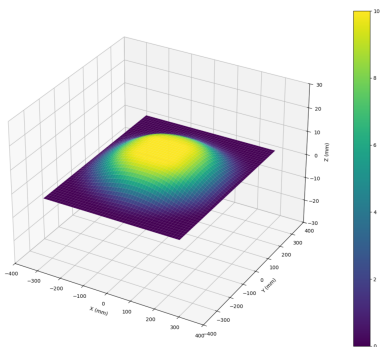
(b) Deflection top sheet for 0.5% of the pressure difference.



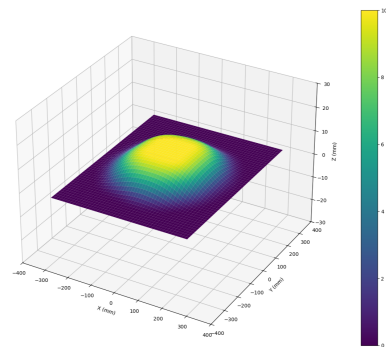
(c) Deflection top sheet for 1% of the pressure difference.



(d) Deflection top sheet for 2% of the pressure difference.



(e) Deflection top sheet for 3% of the pressure difference.



(f) Deflection top sheet for 10% of the pressure difference.

Figure 6.2: Static FEM simulation displacement results six different vacuum percentages. The dimensions of test product one are simulated with a 10 mm distance between the first and second sheet.

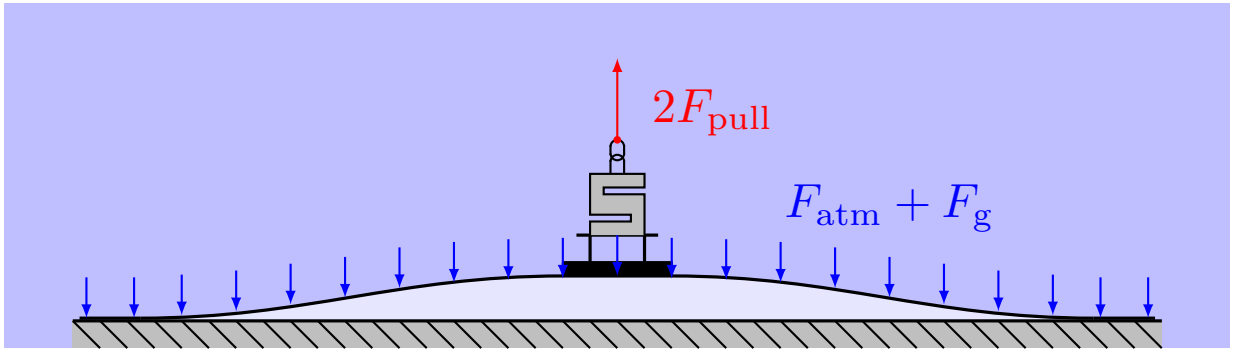


Figure 6.3: Destacking schematic cross-section

only half of the sheet is modelled.

Point A is constrained by a y -guided cart, while point B is constrained by a hinge on an x -guided cart. This configuration allows point A to move only in the y -direction, while point B can rotate and move in the x -direction. The rotation of point A is constrained due to the symmetry of the setup. In reality, the moment M_A at point A is provided by the left side of the sheet, resulting in zero rotation at the centre of the sheet. Additionally, point A is not fixed in the y -direction, as with a cantilever beam, to ensure that the effector can lift the sheet upward using F_{pull} .

Point B is placed on a cart to allow the ends of the sheet to glide over the rest of the stack, enabling movement in the x -direction and thereby allowing for an increase in the cavity volume.

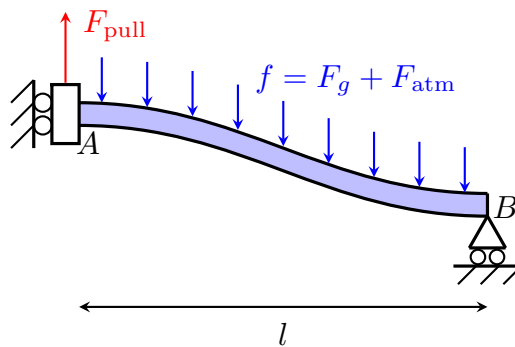


Figure 6.4: Sketch of a guided-hinged beam that is subjected to a point load and a distributed load.

Similar to the derivations in Sections 2.5, 2.6 and 2.7, a free body diagram is needed to formulate the equations of equilibrium at point A . The free body diagram of the beam in Figure 6.4 can be seen in Figure 6.5. This diagram is used to formulate equations of equilibrium at point A . This diagram is used to formulate the following equations of equilibrium at point A :

$$\sum F_y \uparrow + = 0 = F_{\text{pull}} + F_B - fl \quad (6.1)$$

$$F_B = fl - F_{\text{pull}} \quad (6.2)$$

$$\sum M \circlearrowleft + = 0 = M_A + F_B l - \frac{1}{2} fl^2 \quad (6.3)$$

$$M_A = \frac{1}{2} fl^2 - F_B l \quad (6.4)$$

$$M_A = \frac{1}{2} fl^2 - fl^2 + F_{\text{pull}} l \quad (6.5)$$

$$M_A = -\frac{1}{2} fl^2 + F_{\text{pull}} l \quad (6.6)$$

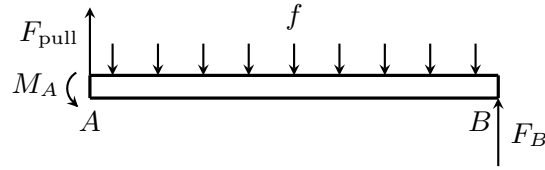


Figure 6.5: Free body diagram of the guided-hinged beam in figure 6.4.

A section is made at location x on the beam to calculate the internal bending moment $M(x)$ and shear force $S(x)$. The free body diagram of the left section of the beam can be seen in Figure 6.6. The internal moment $M(x)$ is obtained by stating the equations of equilibrium at location x :

$$\sum F_y \uparrow + = 0 = F_{\text{pull}} - fx - S(x) \quad (6.7)$$

$$S(x) = F_{\text{pull}} - fx \quad (6.8)$$

$$\sum M \circlearrowleft + = 0 = M_A + M(x) + \frac{1}{2} fx^2 - F_{\text{pull}} x \quad (6.9)$$

$$M(x) = -\frac{1}{2} fx^2 + F_{\text{pull}} x - M_A \quad (6.10)$$

$$M(x) = -\frac{1}{2} fx^2 + F_{\text{pull}} x + \frac{1}{2} fl^2 - F_{\text{pull}} l \quad (6.11)$$

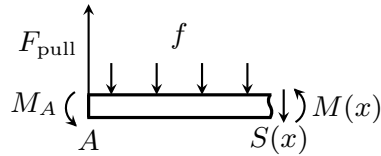


Figure 6.6: Free body diagram of a section of the beam in figure 6.5, the diagram shows the left side of a cut in the beam in location x .

This expression of the internal moment $M(x)$ can be used to find the deflection function $v(x)$ using the Euler-Bernoulli beam theory [9]:

$$v(x) = \frac{1}{EI} \iint M(x) dx^2 \quad (6.12)$$

$$v(x) = \frac{1}{EI} \iint \left(-\frac{1}{2}fx^2 + F_{\text{pull}}x + \frac{1}{2}fl^2 - F_{\text{pull}}l \right) dx^2 \quad (6.13)$$

$$v(x) = \frac{1}{EI} \int \left(-\frac{1}{6}fx^3 + \frac{1}{2}F_{\text{pull}}x^2 + \frac{1}{2}fl^2x - F_{\text{pull}}lx + C_1 \right) dx \quad (6.14)$$

$$v(x) = \frac{1}{EI} \left(-\frac{1}{24}fx^4 + \frac{1}{6}F_{\text{pull}}x^3 + \frac{1}{4}fl^2x^2 - \frac{1}{2}F_{\text{pull}}lx^2 + C_1x + C_2 \right) \quad (6.15)$$

The beam is constraint in its rotation at point A , resulting in zero slope at this position. This constraint gives the first boundary condition: $\frac{dv(0)}{dx} = 0$. Additionally, the beam is constraint in the y-direction at point B , resulting in zero deflection at this position. This constraint gives the second boundary condition: $v(l) = 0$.

The first boundary condition can be used to show that C_1 is zero:

$$\frac{dv(x)}{dx} = \frac{1}{EI} \left(-\frac{1}{6}fx^3 + \frac{1}{2}F_{\text{pull}}x^2 + \frac{1}{2}fl^2x - F_{\text{pull}}lx + C_1 \right) \quad (6.16)$$

$$\frac{dv(0)}{dx} = \frac{1}{EI} C_1 = 0 \quad (6.17)$$

$$C_1 = 0 \quad (6.18)$$

The second boundary condition can be used to determine C_2 :

$$v(x) = \frac{1}{EI} \left(-\frac{1}{24}fx^4 + \frac{1}{6}F_{\text{pull}}x^3 + \frac{1}{4}fl^2x^2 - \frac{1}{2}F_{\text{pull}}lx^2 + C_2 \right) \quad (6.19)$$

$$v(l) = 0 = \frac{1}{EI} \left(-\frac{1}{24}fl^4 + \frac{1}{6}F_{\text{pull}}l^3 + \frac{1}{4}fl^4 - \frac{1}{2}F_{\text{pull}}l^3 + C_2 \right) \quad (6.20)$$

$$0 = -\frac{1}{24}fl^4 + \frac{1}{6}F_{\text{pull}}l^3 + \frac{1}{4}fl^4 - \frac{1}{2}F_{\text{pull}}l^3 + C_2 \quad (6.21)$$

$$0 = \frac{5}{24}fl^4 - \frac{1}{3}F_{\text{pull}}l^3 + C_2 \quad (6.22)$$

$$C_2 = -\frac{5}{24}fl^4 + \frac{1}{3}F_{\text{pull}}l^3 \quad (6.23)$$

This value for C_2 can now be used to determine the deflection function $v(x)$:

$$v(x) = \frac{1}{EI} \left(-\frac{1}{24}fx^4 + \frac{1}{6}F_{\text{pull}}x^3 + \frac{1}{4}fl^2x^2 - \frac{1}{2}F_{\text{pull}}lx^2 + C_2 \right) \quad (6.24)$$

$$v(x) = \frac{1}{EI} \left(-\frac{1}{24}fx^4 + \frac{1}{6}F_{\text{pull}}x^3 + \frac{1}{4}fl^2x^2 - \frac{1}{2}F_{\text{pull}}lx^2 - \frac{5}{24}fl^4 + \frac{1}{3}F_{\text{pull}}l^3 \right) \quad (6.25)$$

The distributed load f [N m^{-1}] needs to be known in order to calculate the deflection function $v(x)$. This distributed force consists of the sum of the distributed gravitational force F_g [N m^{-1}] and the distributed force from the atmospheric pressure difference F_{atm} [N m^{-1}]. The distributed

gravitational force can be seen in Equation 6.26. Here, m is the mass of the sheet [kg], g is the gravitational acceleration [ms^{-2}] and L is the sheet length [m].

$$F_g = \frac{mg}{L} \quad (6.26)$$

The increase in the volume of the cavity underneath the top sheet creates a partial vacuum, resulting in a downward pressure on the top sheet. This occurs because air cannot enter the cavity as long as a seal is not broken. The ambient pressure outside the cavity is denoted as P_0 , the initial pressure within the cavity before the upward movement of the destacking effector is P_1 , and the final pressure inside the cavity after the volume change is P_2 .

Boyle's law states that the product of the pressure and volume of an ideal gas remains constant, provided the temperature and the number of molecules are constant [37]. Using this law, the final pressure P_2 can be determined from the initial pressure P_1 and the respective volume change.

Once P_2 is known, the pressure difference ΔP acting downward on the top sheet can be calculated by comparing P_2 to the ambient pressure P_0 . This is shown in Equations 6.27 to 6.32.

$$PV = \text{constant} \quad (6.27)$$

$$P_1V_1 = P_2V_2 \quad (6.28)$$

$$P_2 = \frac{P_1V_1}{V_2} \quad (6.29)$$

$$\Delta P = P_0 - P_2 \quad (6.30)$$

$$\Delta P = P_0 - \frac{P_1V_1}{V_2} \quad (6.31)$$

$$\Delta P = P_0 \left(1 - \frac{V_1}{V_2} \right) \quad (\text{Only if } P_1 = P_0) \quad (6.32)$$

It is assumed that the cavity pressure before destacking is equal to the ambient pressure ($P_1 = P_0$), so Equation 6.32 can be used to determine ΔP . Figure 6.4 shows the cross-sectional beam for which we want to determine the distributed load f . This load is distributed over a length l , rather than an area. Therefore, the unit of the distributed force f , the distributed gravitational force F_g , and the distributed atmospheric pressure F_{atm} should all be [Nm^{-1}]. To achieve this, the pressure difference ΔP from Equation 6.32 is multiplied with the test part width w to get the atmospheric force over cross-sectional length, instead of the atmospheric force over area. This is shown in Equation 6.33.

$$F_{\text{atm}} = \Delta Pw \quad (6.33)$$

$$F_{\text{atm}} = P_0w \left(1 - \frac{V_1}{V_2} \right) \quad (6.34)$$

$$f = F_g + F_{\text{atm}} \quad (6.35)$$

$$f = \frac{Wg}{L} + P_0w \left(1 - \frac{V_1}{V_2} \right) \quad (6.36)$$

Combining the distributed gravitational force with the distributed atmospheric force gives an expression for the distributed load, which can be seen in Equation 6.36. The initial volume of test

product one in Figure 4.2 is used for the initial cavity volume V_1 . The cavity volume after the volume change V_2 depends on the curved shape of the sheet. The curvature of half of the cross section is described by the deflection function $v(x)$ in Equation 6.25 if the model in Figure 6.4 is used.

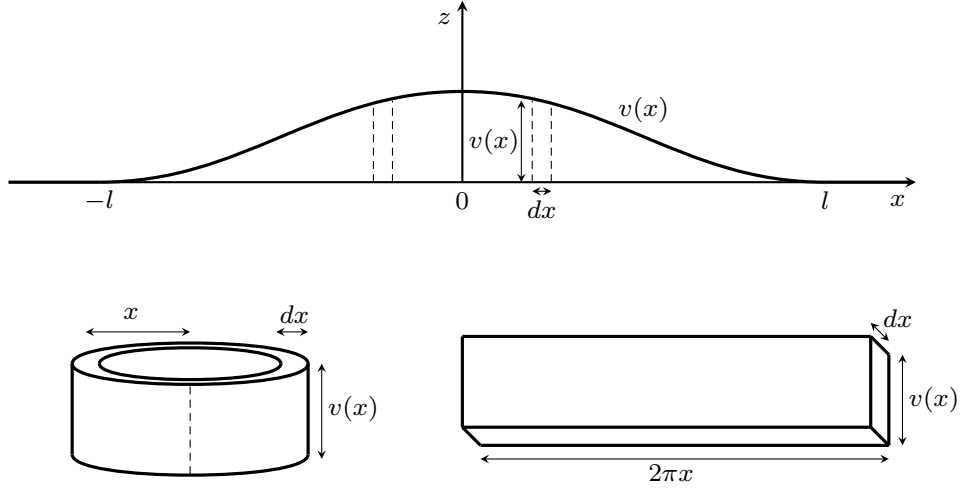


Figure 6.7: Integrating the volume beneath the deflection function $v(x)$ over the radius x to obtain the cavity volume V_2 .

Figure 6.7 shows a drawing of the deflection function $v(x)$. This function gives the y-position of the sheet from $x = 0$ to $x = l$. The mirrored plot of $v(x)$ is also drawn in the range from $x = 0$ to $x = -l$ to get the complete curvature of the cross section that is shown in Figure 6.3. The three-dimensional curve of the sheet is formed by rotating the curve of $v(x)$ around the y-axis. The volume beneath this curve can be divided into hollow cylinders with an infinitesimal thin thickness dx , as drawn in Figure 6.7. Such a cylinder has a radius x and a height $v(x)$. Cutting this cylinder and rolling it out results in the box drawn on the bottom right of Figure 6.7. This box has the infinitesimal volume of $2\pi x \cdot v(x) \cdot dx$. Integrating this volume over the radius from $x = 0$ to $x = l$ gives the cavity volume V_2 [38]:

$$V_2 = \int_0^l 2\pi xv(x)dx \quad (6.37)$$

$$v(x) = \frac{1}{EI} \left(-\frac{1}{24}fx^4 + \frac{1}{6}F_{\text{pull}}x^3 + \frac{1}{4}fl^2x^2 - \frac{1}{2}F_{\text{pull}}lx^2 - \frac{5}{24}fl^4 + \frac{1}{3}F_{\text{pull}}l^3 \right) \quad (6.38)$$

$$V_2 = \frac{2\pi}{EI} \int_0^l x \left(-\frac{1}{24}fx^4 + \frac{1}{6}F_{\text{pull}}x^3 + \frac{1}{4}fl^2x^2 - \frac{1}{2}F_{\text{pull}}lx^2 - \frac{5}{24}fl^4 + \frac{1}{3}F_{\text{pull}}l^3 \right) dx \quad (6.39)$$

$$V_2 = \frac{2\pi}{EI} \int_0^l \left(-\frac{1}{24}fx^5 + \frac{1}{6}F_{\text{pull}}x^4 + \frac{1}{4}fl^2x^3 - \frac{1}{2}F_{\text{pull}}lx^3 - \frac{5}{24}fl^4x + \frac{1}{3}F_{\text{pull}}l^3x \right) dx \quad (6.40)$$

$$V_2 = \frac{2\pi}{EI} \left[-\frac{1}{144}fx^6 + \frac{1}{30}F_{\text{pull}}x^5 + \frac{1}{16}fl^2x^4 - \frac{1}{8}F_{\text{pull}}lx^4 - \frac{5}{48}fl^4x^2 + \frac{1}{6}F_{\text{pull}}l^3x^2 \right]_0^l \quad (6.41)$$

$$V_2 = \frac{2\pi}{EI} \left(-\frac{1}{144}fl^6 + \frac{1}{30}F_{\text{pull}}l^5 + \frac{1}{16}fl^6 - \frac{1}{8}F_{\text{pull}}l^5 - \frac{5}{48}fl^6 + \frac{1}{6}F_{\text{pull}}l^5 \right) \quad (6.42)$$

$$V_2 = \frac{\pi}{EI} \left(\frac{1}{9}fl^6 + \frac{3}{20}F_{\text{pull}}l^5 \right) \quad (6.43)$$

This expression for the cavity volume V_2 can be substituted in the expression for the distributed load f , this substitution can be seen in Appendix C. The distributed load in Appendix C has two solutions because the quadratic formula has been used in the substitution. The distributed force is already defined downward in the free body diagram in Figure 6.5. Because of this, the distributed force itself should have a positive sign, which is used in Equation 6.44.

$$f = \frac{-\left(\frac{3\pi F_{\text{pull}}l^5}{20EI} - \frac{Wg\pi l^6}{9EIL} - \frac{P_0w\pi l^6}{9EI}\right) + \sqrt{\left(\frac{3\pi F_{\text{pull}}l^5}{20EI} - \frac{Wg\pi l^6}{9EIL} - \frac{P_0w\pi l^6}{9EI}\right)^2 - 4\frac{\pi l^6}{9EI} \left(-\frac{3Wg\pi F_{\text{pull}}l^5}{20EIL} - \frac{3P_0w\pi F_{\text{pull}}l^5}{20EI} + P_0wV_1\right)}}{2\frac{\pi l^6}{9EI}} \quad (6.44)$$

The area moment of inertia I and the Young's modulus E are used in the Euler-Bernoulli beam theory for the stiffness of a beam. While the Young's modulus is a material property, the area moment of inertia is geometry dependent. The area moment of inertia depends on the cross-section of the beam, as is also discussed in background Section 2.8. The area moment of inertia I of a beam with a rectangular cross-section can be calculated using Equation 6.45. Here, b and h are the width and height of the rectangular cross-section, respectively.

$$I = \frac{bh^3}{12} \quad (6.45)$$

However, the cross-sectional shape of the metal sheet becomes less rectangular as the sheet starts to bend upward in the middle. In practice, the sheet is bending around both the x-axis and the y-axis at the same time, significantly increasing its stiffness. A cross-section of the sheet can be seen in Figure 6.7, this cross-section of the sheet is modelled as a beam. However, since it is assumed that the cavity is radially symmetric, the cross-section in Figure 6.8 is the cross-section of the beam in Figure 6.7. Both cross-sections have the same shape, but can be distinguished by the horizontal x-axis and y-axis.

The bending axis of the cross-section in Figure 6.8 is assumed to have a height that is half of the maximum height ($\frac{1}{2}v(0)$). This is assumed because the top of the beam cross-section experiences

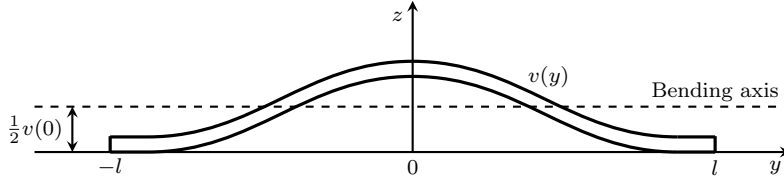


Figure 6.8: Beam cross-section of the modelled sheet during destacking

tension while the bottom undergoes compression. The bending axis is parallel to the horizontal axis, allowing for the use of the parallel axis theorem from Section 2.8. This theorem combines the area moment of inertia I_y around the horizontal axis with the distance d between the bending axis and the horizontal axis. In this case this distance is $\frac{1}{2}v(0)$. The resulting area moment of inertia $I_{y'}$ around the bending axis that results from the parallel axis theorem can be seen in Equation 6.46.

$$I_{y'} = I_y + Ad^2 \quad (6.46)$$

$$I_{y'} = \int z^2 dA + Ad^2 \quad (6.47)$$

The deflection function $v(y)$ that was stated in Equation 6.25 defines the cross-section shape that is shown in Figure 6.8. In Equation 6.25 the deflection function is denoted as $v(x)$, but the x-, and y-axis are interchangeable in this context due to the radial symmetry. This expression can be used substituted for the deflection z in Equation 6.47. However, $v(y)$ is only defined for positive values of y . This is why $I_{y'}$ is first calculated for positive values of y using $v(y)$, and then doubled to obtain the final value for $I_{y'}$. The cross-section of the sheet for positive values of y can be seen in Figure 6.9. This figure also shows how the infinitesimal integration area dA is equal to hdy when integrating along y . The substitution of the deflection function into the equation for the area moment of inertia can be seen in Appendix B. This derivation results in the area moment of inertia in Equation 6.48.

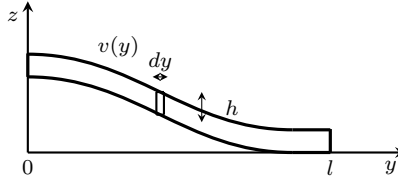


Figure 6.9: Destacking sheet cross-section for positive y values.

$$I_{y'} = \frac{h^{1/3}l^{7/3}}{E^{2/3}} \left(\frac{39619l^2}{725760} f^2 - \frac{13F_{\text{pull}}l}{84} f + \frac{19F_{\text{pull}}^2}{140} \right)^{1/3} \quad (6.48)$$

The area moment of inertia $I_{y'}$ from Equation 6.48 and the distributed load f from Equation 6.44 are interdependent on each other. It was chosen to solve these two equations iteratively in the python code because solving them analytically would result in an undesirably long equation.

An example of the beam deflection plot $v(x)$ that was obtained using the above mentioned equations for $I_{y'}$, f and $v(x)$, can be seen in Figure 6.10. The material and dimension properties of test product one were used for this plot:

- Beam length: 0.284 mm (half the width of test product one)
- Young's modulus: $E = 200 \times 10^9 \text{ N/m}^2$ (typical value for steel [39])
- Starting pressure between the sheets: $P_0 = 101\,325 \text{ N/m}^2$ (one standard atmosphere)
- Starting volume between sheets: $V_0 = 5.4 \times 10^{-6} \text{ m}^3$ (as discussed in Section 4.3)

Figure 6.10 clearly shows that the normal force from the second sheet is not included in the model. In practice, the deflection caused by the distributed load would never drop below zero, as the top sheet cannot pass through the second sheet. Negative values of $v(x)$ are therefore assumed to be zero in practice. It is assumed that the seal beneath the top product remains intact if the slope of $v(x)$ is positive at $x = L$. This condition is satisfied in Figure 6.10 for a pulling force of 10 450 N. Conversely, it is assumed that the seal is broken if the slope of $v(x)$ is negative at $x = L$. This occurs for a pulling force of 11 250 N in Figure 6.10. The breaking point of the seal is defined as the pulling force F_{pull} that results in a slope of zero at $x = L$. In Figure 6.10, this corresponds to a pulling force of 10 850 N.

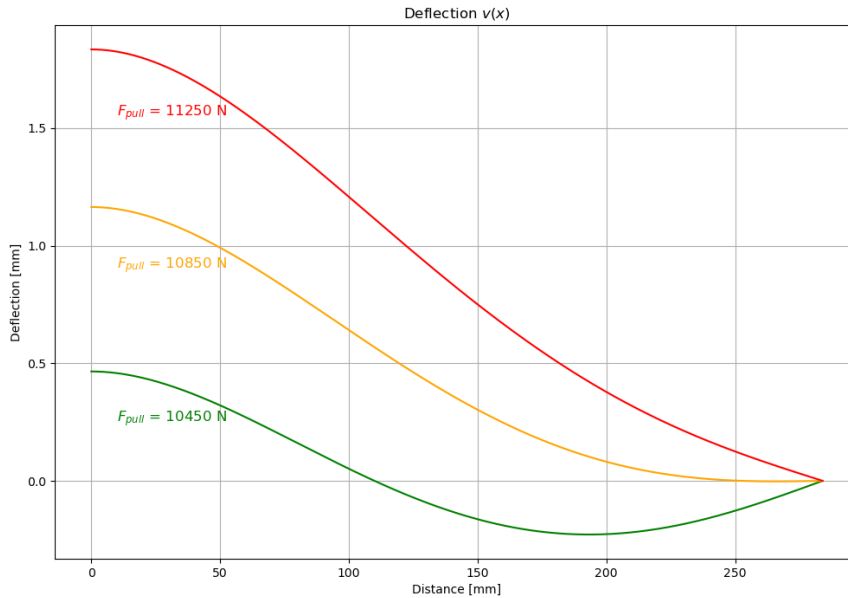


Figure 6.10: Deflection function $v(x)$ for the cross section of half of test product one, subjected to a pulling force F_{pull} on the left and a distributed downward force f .

The model can be applied to calculate the breaking force F_{break} at which the seal beneath the top sheet breaks by iterating through pulling forces. The pulling force that results in a zero slope of $v(x)$ at the point $x = L$ is considered the estimated breaking force for the given beam length.

Results cross-sectional model

The beam length in Figure 6.10 is set to half the width of test product one because the deflection of the sheet cross-section is assumed to be symmetrical, as previously discussed in this section. However, if the effector is not positioned at the centre of the sheet, the distance from the middle of the effector to the sheet's edge is reduced. A shorter distance to the edge limits the space available for the sheet to deflect downward towards the second sheet. To evaluate the effect of the effector's distance to the product edge, the model is iterated using varying beam lengths. The model begins with half the width of test product one and progressively decreases the distance to the edge, which corresponds to reducing the beam length L . The largest modelled length is 280 mm and the shortest length is 60 mm, corresponding with the measured values that will be described in Section 6.4. For each beam length, the model also iterates through increasing pulling forces to determine the estimated breaking force F_{break} . This process produces a plot of the estimated breaking forces for progressively decreasing beam lengths, as shown in Figure 6.11.

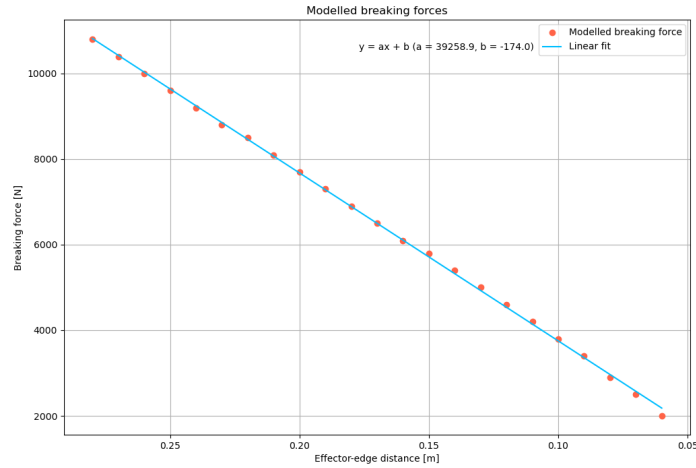


Figure 6.11: Modelled breaking forces at varying effector-edge distances, with linear fit function.

The breaking forces estimated by the cross-sectional model appear to follow a linear trend. To determine the parameters of this trend, the data points were fitted with a linear function using the `polyfit()` function from the NumPy Python package. This function fits polynomial curves of a specified degree to a set of data points. In the case of a linear fit, the resulting function has the form $y = ax + b$ [40].

For the modelled breaking forces, the linear fit yields a slope (a) of $39\,258.9\text{ N m}^{-1}$ (39.2589 N mm^{-1}) and an intercept (b) of -174.0 N , as shown in Figure 6.11. Note that the x-axis of Figure 6.11 is inverted to highlight the decrease in breaking force as the effector is placed closer to the edge, this explains why the slope a is positive and not negative.

Conclusion cross-sectional model development

The linear fit of the modelled breaking forces in Figure 6.11 indicates that the breaking force decreases linearly as the distance between the effector and the product edge is reduced. Solving the fit function

for $ax + b = 0$ gives a zero-crossing at $x = 4.4$ mm. Given the uncertainties in the fit and the dimensions of test product one (736 mm by 567 mm), this value can be approximated as zero.

The cross-sectional model therefore predicts that the breaking force increases with the effector–edge distance at a rate of approximately 40 N mm^{-1} , and approaches zero when picking up the product directly at the edge.

This prediction supports the destacking strategy of minimising the distance between the effector and the product edge to maximise the likelihood of successful separation. However, the estimated breaking forces are excessively high, with the model predicting a maximum pulling force exceeding 10 000 N for the destacking of test product one. Such forces are unrealistic, as other components in the destacking system would likely fail or separate before reaching this level.

Nonetheless, the cross-sectional model reveals a clear linear relationship between the effector–edge distance and the breaking force. An experimental setup is required to validate whether this linear trend holds in practice. The experimental validation of the cross-sectional model is discussed in Section 6.4.

6.3 Finite element model development

A three-dimensional predictive deflection model can be used to predict the effect of effector placement on double-sheet pickups. Such a model can use specific product dimensions and effector sizes to determine whether a double-sheet pickup will occur based on the given effector placement. Finite Element Modelling (FEM) is typically used to calculate deformations and reaction forces for three-dimensional shapes. These models are often created in specialised FEM software designed for both meshing and simulating such scenarios. However, to apply FEM calculations in a destacking process, the calculations must be time-efficient and easily integrable into the existing system. This means that standalone FEM software is unsuitable, as it cannot be easily integrated into real-time code of the effector placement software. This section outlines the development process during this assignment to develop a FEM solution that can be integrated in real time with existing effector placement software.

PyNite library

As discussed above, the FEM software should be capable of being integrated into real-time effector placement code. For the three-dimensional predictive sheet deflection model, it was decided to search for a Python FEM library. Using Python for this purpose offers several advantages: it is platform-independent, open-source (and therefore free to use) and it facilitates rapid development due to its ease of use. Although more computationally efficient languages exist, Python’s time efficiency is more than adequate for the purposes of this assignment.

The Python library chosen for this purpose is PyNite. PyNite is an open-source Python library designed for performing Finite Element Analysis (FEA) of structures [41]. The library offers a user-friendly set of functions, which are both lightweight and easy to use. This particular library was selected for its ease of use and its flexibility in meshing, defining loads, applying constraints, and other features.

Materials and Meshing

PyNite allows users to define custom materials that can be assigned to meshed structures. The defined material properties are used during model analysis to compute deflections, stresses, and strains. The `add_material()` function allows the user to define the Young’s modulus, the shear

modulus, the Poisson's ratio and the density of a material. For this assignment, steel was used as the material, with the following properties:

- Young's modulus: $210 \times 10^9 \text{ N m}^{-2}$ [42]
- Shear modulus: $79.3 \times 10^9 \text{ N m}^{-2}$ [43]
- Poisson's ratio: 0.30 [44]
- Density: 7850 kg m^{-3} [45]

In finite element models, a mesh represents a discretisation of a structure's geometry. It is composed of elements and nodes, with the nodes acting as connection points between the elements. Elements can be one-, two-, or three-dimensional, depending on the geometry being modelled. Due to the flat geometry of the sheets, two-dimensional quadrilateral elements were chosen for this application.

The PyNite package includes several functions for generating meshes of specified shapes. The `add_rectangle_mesh()` function was used in this assignment to generate a mesh for a rectangular sheet. This function accepts the width, length, and thickness of the sheet, along with a mesh size parameter. A smaller mesh size results in a finer mesh with greater detail but increases computational load. A mesh size of 50 mm was selected, as it provided a good balance between computational efficiency and mesh resolution.

Supports

The destacking effector is moved upward slowly during the experiments described in Sections 5.3 and 6.4, resulting in an effector height that changes over time. However, the PyNite library is not designed to handle structures or loads that change over time. Therefore, it was decided to simulate the destacking setup at a fixed effector height. This height (z -coordinate) can then be varied across separate simulations to determine for example the seal width for different effector positions.

To simulate the effect of the destacking effector, the middle node of the meshed sheet is fixed in place at the specified effector height. This constraint is applied using the `def_support()` function, which can fix translation of a node in the x , y , and z directions, as well as its rotation around the x -, y -, and z -axes.

Gravitational Forces

The gravitational force acting on the sheet is calculated by multiplying its mass with the gravitational acceleration, $g = 9.81 \text{ m s}^{-2}$. The total gravitational force is then evenly distributed across all nodes in the mesh by dividing it by the total number of nodes. This results in a uniform gravitational load applied to each node in the negative z -direction.

The `add_node_load()` function is used to apply these forces. This function allows the application of external loads or torques to individual nodes.

Normal Forces

Dedicated FEM simulation programs often include collision features. These features can for example be used to simulate interactions between solid bodies and virtual walls. The Solidworks simulation plots in Figure 6.2 show an example of an interaction between a solid body and a virtual wall. In these simulations, a virtual wall is included that acts as a ground plane, resulting in the deformed

shape shown in the figure. Simulating such a ground plane, through which the modelled sheet cannot pass, is needed to realistically model the deformations of the sheet.

The PyNite library does not include built-in functions to simulate collisions with virtual walls or other structures. A virtual wall, necessary in the simulation to represent the second sheet in the stack, provides normal forces to the nodes, preventing them from passing through the sheet. Since this feature is not available in PyNite, the normal forces exerted by the second sheet are calculated and applied iteratively to the corresponding nodes.

To calculate the required normal forces from the second sheet on the top sheet, a list is created to store the normal force for every node in the mesh. When the top sheet is simulated without applying normal forces, parts of the sheet partially pass through the second sheet in the stack (ground plane at $z = 0$). This can be seen in Figure 6.12. To counteract this, a normal force is applied to nodes that fall below $z = 0$, with the magnitude scaled according to the z -distance between the node and $z = 0$. The model is then reanalysed.

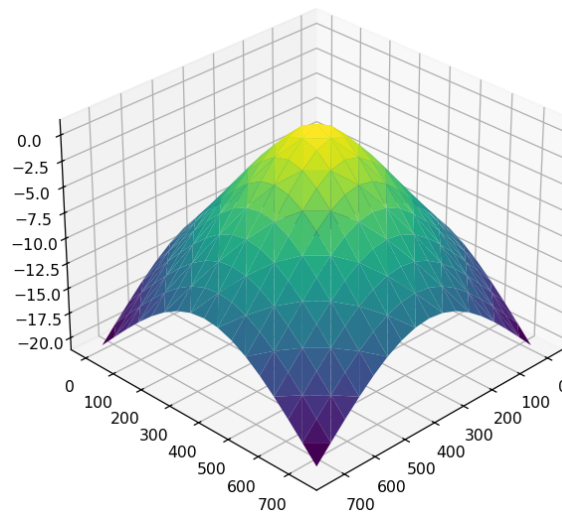


Figure 6.12: Sheet deflection in mm due to gravitational forces with a fixed middle node at $z = 1$ mm.

Any nodes still below zero are subjected to an additional normal force, again scaled by the z -distance between the node and $z = 0$. This iterative process is executed for a predetermined number of iterations, which is an input parameter to the model. After all iterations, all nodes should converge to zero or a positive z -value. Using this method, the normal forces from the second sheet (ground plane) acting on the contacting nodes can be determined iteratively. This approach offers a solution to the lack of built-in collision features in the PyNite library for this application.

Figure 6.13 shows the sheet deflection resulting from the application of the iteratively determined normal forces to the same sheet as depicted in Figure 6.12. The sheet in Figure 6.13 is subjected to the gravitational force and the normal forces exerted by the second sheet.

Atmospheric Forces

As described in earlier sections, the pressure difference between atmospheric pressure and the cavity beneath the top sheet increases as the effector moves upward. This pressure difference acts on the

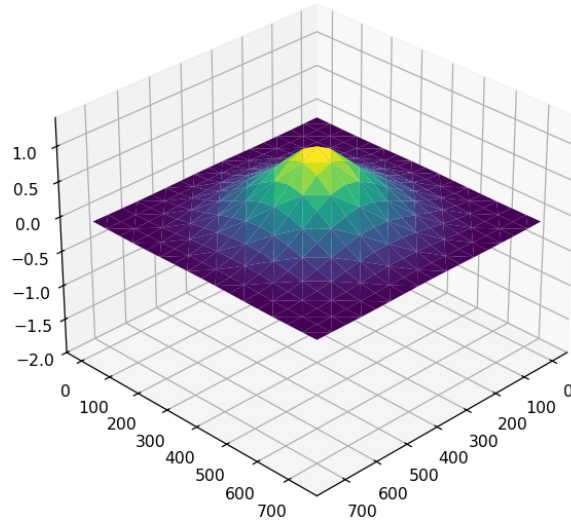


Figure 6.13: Sheet deflection in mm due to gravitational forces and normal forces with a fixed middle node at $z = 1$ mm.

top sheet as a distributed downward load. The pressure difference depends on the atmospheric pressure P_0 , the initial volume between the sheets V_1 , and the current cavity volume V_2 , as shown in Equation 6.32 and repeated in Equation 6.49. This equation is valid under the assumption that the initial pressure between the sheets is equal to atmospheric pressure, which is assumed for this assignment.

$$\Delta P = P_0 \left(1 - \frac{V_1}{V_2} \right) \quad (6.49)$$

A standard atmospheric pressure of $101\,325 \text{ N/m}^2$ is used for P_0 . The initial volume V_1 is taken from measurements of test product one ($5.421 \times 10^{-6} \text{ m}^3$), as shown in Figure 4.2. The current cavity volume V_2 is approximated by summing the products of the area per node and the z -coordinates of all nodes located above zero.

The resulting pressure difference ΔP [N/m^2] is then multiplied by the area per node [m^2] to obtain the downward force per node due to the pressure difference. This force is applied to all nodes with a z -coordinate above zero using the `add_node_load()` function.

Analysing the model using atmospheric pressure forces, as described above, did not result in converging deflections, as shown in Figure 6.13. The atmospheric forces are significantly larger in magnitude than the gravitational forces. Attempting to calculate the normal forces while accounting for both gravitational and atmospheric forces resulted in non-converging deflections.

Due to time constraints, there was limited opportunity to further investigate and resolve these issues. A convergence criterion based on displacement thresholds could be considered in future work. As a result, further development of a FEM-based destacking model in Python will require either additional development work or the use of a library that does support collision features.

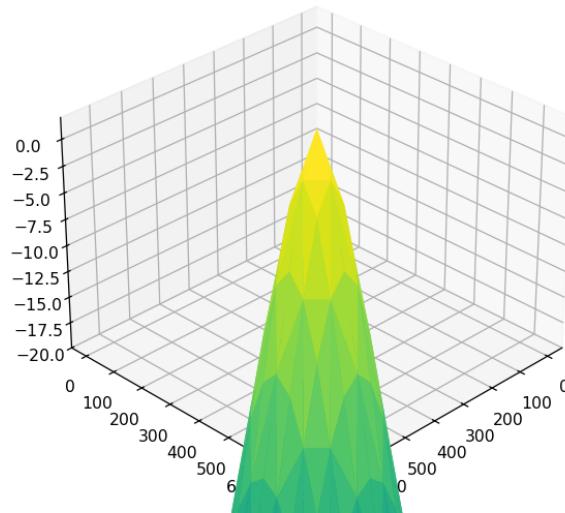


Figure 6.14: Sheet deflection in mm due to gravitational forces, normal forces and atmospheric forces with a fixed middle node at $z = 1$ mm.

Conclusion finite element model development

The PyNite modelling library offers an integrated approach for simulating sheet deflections within a Python environment, making it suitable for integration into existing systems. However, the library is primarily designed to simulate the effects of loads on static structures, such as beam constructions. It does not include functionality to simulate collisions with virtual walls, which is essential for modelling the normal forces exerted by the second sheet in the stack.

An attempt was made to calculate these normal forces manually, but this approach led to non-converging results. As a result, this modelling approach did not yield a predictive model that was suitable for the purposes of this assignment. Although a more appropriate Python library for this specific application was not identified during this assignment, such a library may exist and could potentially provide a better fit for the modelling requirements.

6.4 Model validation

To assess the accuracy of the cross-sectional model in predicting the maximum pulling force at varying distances between the effector and the edge of the product, experimental validation is required. This section describes the experiments conducted to obtain corresponding measurements, compares the model's predictions to the experimental results and discusses the validation of the finite element model.

Experimental setup

The experimental setup used to measure the breaking force at various distances between the effector and the product edge is generally the same as described in Section 5.3. During these measurements, it was observed that the second sheet deflected upward at the edges during the destacking process, while being held down in the centre by the fixture device shown in Figure 5.2.

To help explain this effect, a schematic drawing was made, as shown in Figure 6.15. This figure presents a cross-section of the destacking setup described in Section 5.3, with the bottom section representing the fixture device. The deflections illustrated are exaggerated for clarity. As the effector moves upward, the bending required to maintain the seal is distributed between both sheets. If the second sheet were held completely horizontal, all the bending would have to occur in the top sheet, causing the seal to break sooner for the same effector height.

Since the bending effect of the second sheet shown in Figure 6.15 was not included in the modelling, it was avoided for the experiments in this section by using a larger stack (more than 10 parts) instead of the fixture device. Replacing the fixture device, which allowed the bending effect shown in Figure 6.15, with a larger stack reduced the maximum pulling forces observed before seal breakage.

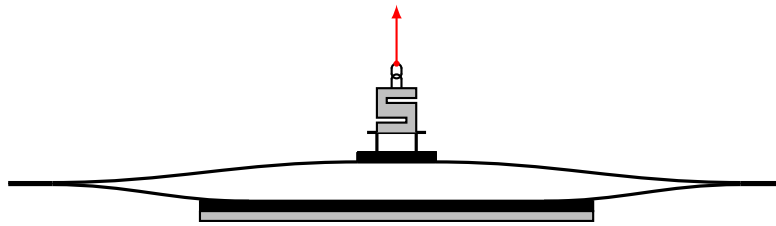


Figure 6.15: Edges of the second sheet deflect upward during destacking while being held down in the centre by the fixture device from Figure 5.2.

The experimental results from Section 5.5 showed that adhesion forces were not observed for test product two. For this reason, the experiments described in this section were conducted only on test product one.

The cross-sectional model predicts the maximum pulling forces (breaking forces) for varying distances between the effector and the product edge. To evaluate the accuracy of these predictions, a total of 23 measurements were performed at different effector-edge distances.

The largest effector-edge distance used is 280 mm, which corresponds to approximately half the width of test product one. The smallest distance used is 60 mm, which is approximately half the width of the small vacuum pad. Using a smaller distance would cause the vacuum pad to lose pressure on the product edge.

Experimental results

The plots of the measured pulling force over time for these measurements are shown in Figure 6.16. As seen in most of the plots, the pulling force increases as the robotic manipulator moves upward. This increase compensates for the growing pressure on the top sheet caused by the partial vacuum beneath it. The breaking force is reached when the seal under the top sheet begins to fail, allowing air to enter and equalise the pressure difference. For the effector-edge distances of 80 mm, 70 mm, and 60 mm, the sheets were observed to separate immediately.

To clarify the relationship between breaking force and effector-edge distance, the peak pulling forces (breaking forces) from Figure 6.16 are plotted separately in Figure 6.17.

Cross-sectional model validation

The results of the cross-sectional model can be approximated with a linear fit, as shown in Figure 6.11. Similarly, the measured breaking forces from Figure 6.17 were fitted with several functions to analyse the trends in the experimental data. Specifically, linear, quadratic, and exponential fits

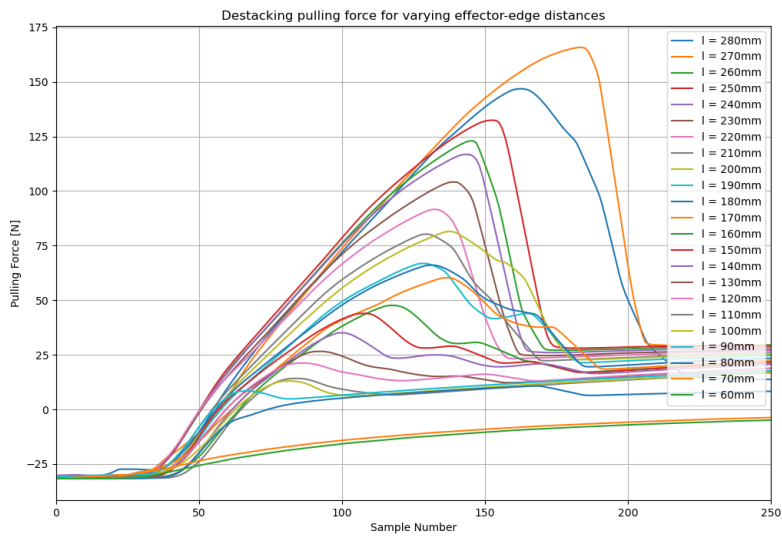


Figure 6.16: Effector pulling force for varying distances to the product edge.

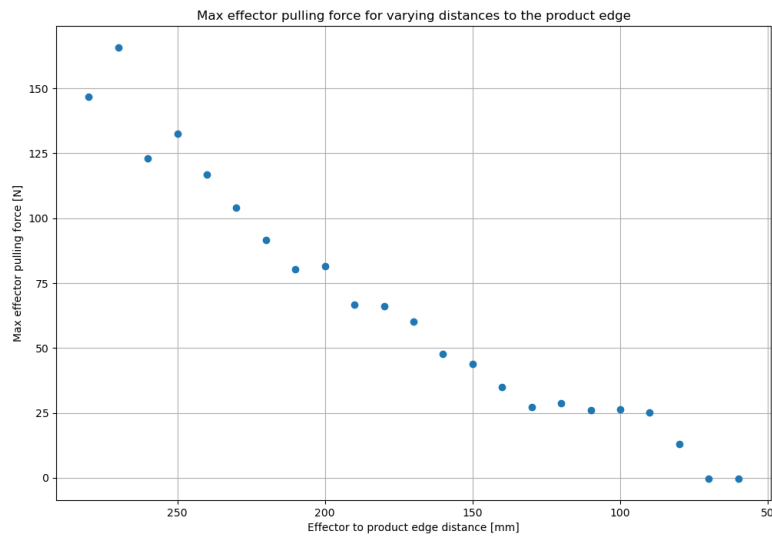


Figure 6.17: Measured breaking forces at varying effector-edge distances.

were applied to the measured breaking forces, as shown in Figure 6.18. The `polyfit()` function from the NumPy package was used for the linear and quadratic fits, while the `curve_fit()` function from the SciPy package was used for the exponential fit. The latter can be used for general-purpose

non-linear curve fitting [46]. The resulting coefficients for the fit functions are also shown in Figure 6.18.

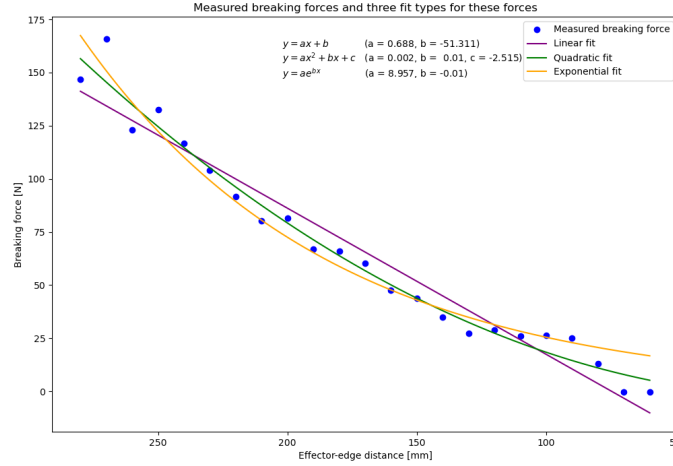


Figure 6.18: Measured breaking forces at varying effector-edge distances, with linear, quadratic, and exponential fit functions.

To quantify the fit quality, the Residual Sum of Squares (RSS) was used. This metric is calculated by squaring the difference between each measured data point and the corresponding value from the fit function, then summing all these squared differences, as expressed in Equation 6.50. A lower RSS value indicates a better fit to the data.

$$\text{RSS} = \sum_{i=1}^n (y_i - \hat{y}_i)^2 \quad (6.50)$$

Using Equation 6.50 on the fit functions shown in Figure 6.18, the following RSS values were obtained:

- Linear RSS: 2568.6
- Quadratic RSS: 1163.6
- Exponential RSS: 1975.0

These values indicate that the quadratic function provides the best approximation of the measured breaking forces, followed by the exponential fit. The linear fit yields the highest RSS and is therefore the least accurate of the three. However, when visually comparing the fit curves with the experimental data in Figure 6.18, it is evident that all three fits provide a reasonably good approximation given the spread of the measurements.

Consequently, a linear model can still offer a relatively reliable prediction of the breaking forces, especially when using the calculated coefficients $a = 0.688 \text{ N mm}^{-1}$ and $b = -51.311 \text{ N}$ from Figure 6.18. In contrast, the linear fit for the cross-sectional model shown in Figure 6.11 has significantly different coefficients, with $a = 39.26 \text{ N mm}^{-1}$ and $b = -174.0 \text{ N}$. The difference is especially notable in the slope, indicating a substantial difference between the modelled and measured force behaviours.

Finite element model validation

The developed finite element model aims to simulate the deflections of a sheet subjected to gravitational, atmospheric, and normal forces. The model was implemented using the PyNite library, but it did not reach a stage of development where quantitative validation could be performed.

The lack of built-in contact modelling in the PyNite library led to the development of an iterative approach to approximate the normal forces from the second sheet in the stack. Despite these efforts, the method proved computationally unstable when atmospheric forces were included, resulting in diverging deflections.

Due to these limitations and time constraints, the model could not be extended to predict breaking forces for validation against experimental data. As such, the finite element model serves primarily as a proof of concept for integrating FEM simulations into the destacking model program. Further development, such as implementing more advanced contact modelling or identifying a different FEM library with built-in collision detection, would be necessary to enable meaningful quantitative validation.

6.5 Conclusion

The main focus of this thesis is to optimise the destacking process by isolating the critical factors and predicting when the double-sheet problem will occur for a given product. Achieving this requires a precise and efficient model, one that accurately predicts the double-sheet phenomenon while remaining computationally efficient to prevent delays. Additionally, the model should be able to integrate easily into the destacking process.

The experimental measurements show that the breaking force for a stacked sheet decreases as the effector is placed closer to the edge. This relationship is best approximated using a quadratic fit line. However, exponential and linear fit lines also provide reasonable approximations of the breaking force, given the spread in the measurements.

The predicted breaking forces from the cross-sectional model can similarly be fitted using a linear fit line. However, the slope of the fit line for the cross-sectional model is approximately 57 times greater than the slope of the fit for the measured values. As a result, the cross-sectional model cannot be considered a competent predictive model, despite its computational efficiency.

To further investigate the problem, a finite element model was developed using the PyNite library. This model introduced a method for simulating sheet deflections under gravitational, atmospheric and normal forces. Although promising due to its ease of integration, the finite element model encountered significant limitations. The absence of built-in contact modelling required the development of an iterative approximation method for the normal forces. This method proved computationally unstable when atmospheric forces were applied. As a result of these challenges and time limitations, the model could not be quantitatively validated or extended to predict breaking forces.

These findings indicate that a more advanced model is required to accurately predict the double-sheet phenomenon. Such a model would need a more precise representation of the normal forces, a more realistic classification of when a seal is broken, and a three-dimensional approach to account for effector placement across the entire sheet. For FEM-based approaches, the use of a simulation framework with built-in support for contact detection would also be essential. Future development of a model for double-sheet prediction should incorporate these factors in order to obtain a more accurate and reliable prediction.

Chapter 7

Discussion

This chapter presents a discussion on the findings presented in this thesis. The modelling and experimental approaches are reviewed and the implications for robotic destacking systems are discussed. This chapter focuses on interpreting the results presented in the previous chapters. This chapter also discusses the limitations of the the assignment.

7.1 Analysis of breaking force prediction discrepancies

The breaking forces that are estimated by the cross-sectional model are significantly higher than the measured breaking forces. Both the modelled values and measured decrease as the effector-edge distances decreases. When approximating this relation between the breaking force and the effector-edge distance as a linear function, the slope of the model is approximately 57 larger than the slope of the experimental value fit. Additionally, the linear fits have an intercept difference of 122.7 N. Several factors may contribute to the differences between the coefficients of the linear fit functions.

One factor that can affect the stiffness of the material, and consequently the breaking force, is the Young's modulus. The cross-sectional model assumes a Young's modulus of $200 \times 10^9 \text{ N/m}^2$, corresponding to alloy steel. However, the Young's modulus for steels can vary between $190 \times 10^9 \text{ N/m}^2$ and $215 \times 10^9 \text{ N/m}^2$, depending on the specific alloy used [47]. A variation in the stiffness of a sheet can influence the breaking force. The Young's modulus may be up to 5.0 % lower or 7.5 % higher than the value used in the model. This 12.5 % variation can lead to a comparable percentage of variation in the predicted breaking forces when the Young's modulus is varied.

The cross-sectional model approximates the cross-section of the sheet as a beam subjected to a distributed load and supported by a hinged cart on the right. It includes a condition to determine whether the seal beneath the sheet is broken. According to this condition, the seal is broken if the beam's slope on the right side is zero or negative. However, it is possible that this behaviour differs in practice. When the slope at $x = l$ is only slightly positive, the resulting seal width may be small, still resulting in seal rupture.

Modelling the breaking force as a function of seal width was not incorporated into the cross-sectional model, as this model does not include normal forces. Normal forces were excluded to keep the model relatively simple. To compensate for this, the zero-slope condition for determining seal breakage was introduced. However, without normal forces to push the sheet above zero deflection, the model is unable to determine the actual width of the seal.

Future research could elaborate on the cross-sectional model by including normal forces if the continuation of this modelling approach is desired. Additionally, the correlation between seal width

and seal breakage may depend on the pressure difference, which is also not considered in the current model. Incorporating this effect could reduce the predicted breaking forces and help narrow the discrepancy between the model's predictions and the experimental results. However, the extent to which this difference would be reduced is difficult to quantify without implementing the proposed modifications to the model.

Since the robotic manipulator was moved upward slowly during the experiments, the destacking process was conducted at a relatively low speed. This possibly allows air to seep through the seal and into the cavity during the process. Small imperfections in the sheets could enable air to gradually enter the cavity as the pressure difference increases. If this effect is significant, it could have a considerable impact on the breaking forces, partially explaining the relatively low breaking forces observed compared to the model predictions.

7.2 Evaluation of Modelling Approaches

The development of the cross-sectional model led to a better understanding of the critical factors contributing to the destacking problem, thereby supporting the overall goal of the assignment. The analytical nature of the Euler-Bernoulli beam theory used in this model provides computational efficiency. However, despite the linear trend in its predicted breaking forces, the model lacks predictive accuracy as it significantly overestimates the breaking forces. Potential reasons for this inaccuracy have been discussed above. Future work on this model would benefit from the inclusion of normal forces, allowing for example for the modelling of seal widths.

The development of the finite element model highlights important differences between two-dimensional and three-dimensional modelling. One of the differences is computational efficiency. Modelling the full deflection of a densely meshed sheet subjected to various loads and supports quickly becomes computationally demanding. Due to time constraints and the absence of collision functions in PyNite, the finite element model was not developed to a stage where it could produce reliable predictions regarding breaking forces.

7.3 Limitations

The pulling force measurements use a load cell to record force over time, this can be used to determine the breaking force to a destacking measurement. However, the load cell has a maximum capacity of 1000 N, requiring the measurements for test product one in Chapter 5 to be stopped early to prevent damage. A load cell with a higher force capacity would have allowed the measurements to continue.

As discussed in Section 6.4, the breaking forces predicted by the cross-sectional model are considerably larger than the measured values. The model applies Euler-Bernoulli beam theory to a two-dimensional beam to simulate the cross-sectional deflection of a thin metal sheet during destacking. This approach enables a hand derivation and is computationally efficient but also limits the accuracy of the model.

A limitation of the cross-sectional model is the absence of a normal force from the second sheet in the stack. Deriving a beam deflection model that accounts for this distributed normal force proved challenging, as this reaction force is a non-uniformly distributed load. Additionally, the length range over which this load is applied varies with each beam shape. Multiple derivation attempts were made, but none resulted in a functional predictive model.

As a result, an alternative approach for the cross-sectional model was adopted, in which the normal force is not explicitly modelled, allowing the beam deflection to be negative. While this is not physically accurate, since the top sheet cannot deflect through the second sheet, this simplification

was made because the model's focus is not on the normal force itself, but on the moment it becomes zero. In the context of destacking, this moment represents the point at which the seal thickness between the cavity and the product edge reaches zero.

The cross-sectional model is therefore designed to determine the pulling force at which the sheet's slope at the edges becomes zero. At this force, the deflection at the edges transitions from negative (indicating normal forces in practice) to positive (indicating separation), indicating that the seal thickness has reached zero. This condition is thus chosen as the model's breaking force criterion. This simplification allowed the mathematical model to be derived by hand, but it might also be the reason for the large difference with the measured breaking forces.

A limitation of the FEM model is the iterative approximation of the normal forces that prevents the sheet from deflecting below the height of the second sheet. These forces are approximated iteratively because the selected Python library does not include built-in collision functions. This approximation method was able to produce a realistic deflection result when only gravitational forces were applied. However, when atmospheric forces were added, the model's deflections failed to converge due to their significantly larger magnitude. Further research into a more suitable Python library or alternative approximation methods for the normal forces may help to resolve this issue.

Addressing these limitations could significantly enhance the model's predictive capability and applicability to real-world destacking scenarios.

Chapter 8

Conclusion

8.1 Research questions

The goal of this assignment is to deepen the understanding of the critical factors that influence the sheet separation during destacking. This goal is approached using the following research questions: **How can the critical factors, that contribute to the successful and efficient destacking of thin metal sheets using robotic manipulators, be optimized?**

- How do industry professionals experience and perceive the destacking problem?
- What are the factors that cause adhesion between thin metal sheets, and under what conditions do these forces become significant?
- Under which conditions do adhesive effects influence destacking and when does this become problematic?
- What solutions to the destacking problem have been discussed in the literature?
- How can these insights be used to improve automated destacking procedures?

8.2 Empirical findings

The first research sub-question asks how industry professionals experience and perceive the destacking problem. Two industry professionals were interviewed to gather their experiences with the destacking problem. Both professionals have experienced the destacking problem in practice and described their experiences. Both respondents indicate that the vacuum between the products that results in the atmospheric pressure is the main factor that causes the destacking problem. One of the respondents explains their experiences with residual magnetism in products, while the other respondent explains how an oil layer on the products worsens the problem. Both respondents indicate that vacuum effectors are the most suitable for destacking thin metal products. One of the professionals also emphasizes the importance of a double sheet detection system for a destacking system.

The second research sub-question asks which factors influence the adhesion between thin metal sheets. The following five factors were identified that can influence the adhesion forces between two metal sheets: atmospheric pressure, capillary forces, residual magnetism, the triboelectric effect and metal-to-metal adhesion forces.

The third research sub-question asks under which conditions the destacking is influenced by adhesive effects. It was concluded that the atmospheric pressure, the capillary forces and the residual magnetism can have a considerable contribution to the adhesion forces.

The fourth research sub-question asks which solutions to the destacking problem are discussed in the literature. Destacking solutions such as magnetic sheet separators, air knives, sheet bending and mechanical peeling are described in the literature. Double sheet detection systems can be an important addition to a destacking system. All discussed solutions focus on breaking the airtight seal between the sheets, suggesting that the atmospheric pressure is the main factor at play in the destacking problem.

An experimental setup was used to validate the theoretical sum of forces. This experiment measured the required force to separate two thin metal part and was performed on two test products. The measured adhesion force is negligible for the smaller test product. However, the measured adhesion force for the larger test product exceeded the 1000 N maximum of the used load cell. It can be concluded that the product area drastically influences the adhesion forces. The calculated sum of forces significantly overestimated the adhesion forces for both products. One explanation for this difference is the seal strength being less strong in the real-world experiments in comparison to the assumed seal strength in the calculation of the sum of forces.

The fifth research question asks how the gained insights can be applied to enhance automated destacking procedures. These insights into the adhesion factors between thin metal sheets during destacking can be used to develop a predictive model. Such a model can help determine optimal effector locations on a product and predict the occurrence of the double-sheet problem.

Developing a predictive model that is accurate, computationally efficient, and easy to integrate proved to be challenging. Experimental results show that the breaking force decreases as the effector-edge distance decreases. Although the cross-sectional model predicts this same trend, it significantly overestimates the magnitude of the breaking forces. Constructing a FEM model that can be easily integrated into the real-time code of the effector placement software also proved difficult, primarily due to time restrictions and the lack of built-in collision features.

The results indicate that atmospheric pressure, capillary forces, and residual magnetism are the primary factors influencing the destacking process. Further development of the predictive models and effector placement program, combined with a gripper that bends the top product, could lead to a robust destacking solution.

8.3 Future research directions

This thesis examines the factors contributing to the destacking problem and focuses on developing a model to predict the double-sheet phenomenon. An accurate predictive model for double-sheet pickups is valuable for improving the understanding of the underlying mechanics. However, deriving such models can quickly become complex. Moreover, when practical pickup methods involve multiple effectors, the sheet separation mechanics change, requiring further model development. The same applies when incorporating effectors that bend the top product, such as the gripper shown in Figure 4.7.

For a practical solution to the destacking problem, using a maximum effector-edge distance combined with a mechanical pickup method that induces bending in the product may be sufficient for reliable destacking. As shown in Figure 6.16, vacuums began forming at effector-edge distances greater than 80 mm. These measurements were taken on a dry product with no residual magnetization, so the critical distance may be shorter for products that are more difficult to destack. If this maximum distance from the product edge is known, the effectors can be positioned to minimize

their distance from the edge while maximizing their spacing to promote bending.

Further development of a solution involves improvements in both hardware and software. On the hardware side, a gripper capable of rotating its effectors to bend the product is recommended for successful destacking. A stretching gripper would allow the distance between effectors to be adjusted based on product size. Figure 4.7 illustrates a stretching gripper with magnetic effectors that rotate outward. However, the magnetic field penetrates the stack, attracting multiple products simultaneously. To prevent this, the same gripper platform could be used with vacuum pads instead. This setup would enable the gripper to adapt to the product's size, bend the top sheet, and avoid unintended magnetic attraction.

On the software side, an effector location program needs to be developed to optimize effector placement for effective destacking. This program could use a predictive model similar to those discussed in this thesis or simply apply a maximum allowable distance between the effector and the edge. Based on these criteria, the program would identify optimal effector locations on the product.

8.4 Final Remarks

This research contributes to the field of industrial automation by providing insights into the factors influencing adhesion between metal sheets and proposing potential solutions for improving robotic destacking. While certain limitations exist, the findings form a foundation for further development of predictive models and hardware solutions. By incorporating improved modelling techniques with practical hardware improvements, future advancements in automated sheet destacking can lead to increased efficiency and reliability.

Bibliography

- [1] David Quéré Pierre-Gilles de Gennes Françoise Brochard-Wyart. *Capillarity and Wetting Phenomena*. Springer, 2004.
- [2] Science ABC. *Why Are Bubbles Round?* URL: <https://in.pinterest.com/pin/691232242785996044/>.
- [3] Danya Pang et al. “Liquid-bridge flow between two slender plates: Formation and fluid mechanics”. In: *Chemical Engineering Research and Design* 170 (June 2021), pp. 304–313. ISSN: 02638762. DOI: 10.1016/j.cherd.2021.04.009.
- [4] Vaya Sapobi Samui Vos. “Deformations of a bubble”. In: *Leids Instituut voor Onderzoek in Natuurkunde, Universiteit Leiden* (Apr. 2012), p. 8.
- [5] Michael J. Adamst Guoping Lian Colin Thoeernton. “A Theoretical Study of the Liquid Bridge Forces between Two Rigid Spherical Bodies”. In: *Journal of Colloid and Interface Science* (1 June 1993), pp. 138–147. DOI: <https://doi.org/10.1006/jcis.1993.1452>. URL: <https://www-sciencedirect-com.ezproxy2.utwente.nl/science/article/pii/S0021979783714529>.
- [6] David J. Griffiths. *Introduction to Electrodynamics*. 4th ed. Cambridge University Press, 2017.
- [7] Texas Gateway. *Magnetic Fields, Field Lines, and Force*. 2024. URL: <https://texasgateway.org/resource/201-magnetic-fields-field-lines-and-force>.
- [8] John R Brauer. *Magnetic Actuators and Sensors*. Equation 5.11 gives the magnetic force. 2006. URL: <https://ieeexplore.ieee.org/book/5201936>.
- [9] dr.ir. J.P. Schilder ir. B.M. de Gooijer. “Mechanics of Materials”. In: Faculty of Engineering Technology (ET), 2020, pp. 66–93.
- [10] E.J. HEARN. “CHAPTER 5 - SLOPE AND DEFLECTION OF BEAMS”. In: *Mechanics of Materials 1 (Third Edition)*. Ed. by E.J. HEARN. Third Edition. Oxford: Butterworth-Heinemann, 1997, pp. 92–139. ISBN: 978-0-7506-3265-2. DOI: <https://doi.org/10.1016/B978-075063265-2/50006-2>. URL: <https://www.sciencedirect.com/science/article/pii/B9780750632652500062>.
- [11] EfficientEngineer.com. *Understanding the Area Moment of Inertia*. May 2024. URL: <https://efficientengineer.com/area-moment-of-inertia/>.
- [12] Chegg.com. *Compression h/2 Neutral Axis Tension A ideal beam in pure bending*. URL: <https://www.chegg.com/homework-help/questions-and-answers/compression-h-2-neutral-axis-tension-ideal-beam-pure-bending-deforms-like-arc-circle-centr-q41432761>.
- [13] The Efficient Engineer. *Understanding the Area Moment of Inertia*. May 2024. URL: <https://efficientengineer.com/area-moment-of-inertia/>.

- [14] EuroTech. *How to calculate vacuum suction force to find appropriate suction cups?* July 2022. URL: <https://eurotech-vacuum-technologies.com/how-to-calculate-vacuum-suction-force-to-find-appropriate-suction-cups/>.
- [15] E. J. De Souza et al. "Enhancement of capillary forces by multiple liquid bridges". In: *Langmuir* 24 (16 Aug. 2008), pp. 8813–8820. ISSN: 07437463. DOI: 10.1021/la8005376.
- [16] Iowa State University. *Physics of Nondestructive Evaluation: Magnetism*. URL: <https://www.nde-ed.org/Physics/Magnetism/HysteresisLoop.xhtml>.
- [17] Maurer Magnetic. *Measuring instrument technology Measuring residual magnetism As production manager*. Aug. 2021. URL: <https://content.ndtupply.com/assets/Uploads/Measuring-Instrument-Technology-Maurer-Magnetic.pdf?clientId=671729267.1721001600>.
- [18] Thomas Freund. *Tribo-Electricity*. 1979. URL: [https://doi.org/10.1016/0001-8686\(79\)80003-2](https://doi.org/10.1016/0001-8686(79)80003-2).
- [19] AlphaLab Inc. *Electrostatic Effects*. Nov. 2022. URL: <https://www.alphalabinc.com/static-electricity-effects/#:~:text=Because%20of%20mutual%20repulsion%2C%20the,%2B%20or%20%E2%80%93%20charges%20redistribute%20themselves..>
- [20] M E Sikorski. *THE ADHESION OF METALS AND FACTORS THAT INFLUENCE IT*. 1964.
- [21] K. Yuri. *Convert standard atmosphere [atm] to pascal [Pa]*. 2017. URL: https://www.translatorscafe.com/unit-converter/en-US/pressure/52-1/standard%20atmosphere-pascal/#google_vignette.
- [22] Ansys Innovation Space. *Surface tension issues*. 2018. URL: <https://innovationspace.ansys.com/forum/forums/topic/surface-tension-issues/>.
- [23] Anton Paar. *Viscosity of Engine Oil*. 2024. URL: <https://wiki.anton-paar.com/nl-en/engine-oil/>.
- [24] Byju's. *Density of air*. 2024. URL: [https://byjus.com/physics/density-of-air/#:~:text=The%20value%20of%20air%20density%20is%201.29%20grams%20per%20litre,of%20mercury%20or%20760%20millimetres\)..](https://byjus.com/physics/density-of-air/#:~:text=The%20value%20of%20air%20density%20is%201.29%20grams%20per%20litre,of%20mercury%20or%20760%20millimetres)..)
- [25] Helling NDT. *Residual magnetic field meter MP-80*. 2024. URL: <https://helling.de/en/product/restfeld-messgeraet-mp-80-en/>.
- [26] J.M.K.C. Donev et al. *Permeability of free space*. 2024. URL: https://energyeducation.ca/encyclopedia/Permeability_of_free_space.
- [27] Goudsmit Magnetics. *Pneumatische magneetgrijper - 40 mm*. 2024. URL: <https://www.goudsmitmagnetics.com/nl-nl/producten/pneumatische-magneetgrijper-40-mm/tpgc040078>.
- [28] The Engineering ToolBox. *Permeability*. 2016. URL: https://www.engineeringtoolbox.com/permeability-d_1923.html.
- [29] S. Zurek. *Magnetic permeability*. 2023. URL: https://www.e-magnetica.pl/doku.php/magnetic_permeability.
- [30] Goudsmit Magnetics. *Pneumatische magneetgrijper - 24 mm*. 2024. URL: <https://www.goudsmitmagnetics.com/nl-nl/producten/pneumatische-magneetgrijper-24-mm/tpgc024078>.
- [31] Piezo Data. *7 Facts you should know about double sheet sensors*. 2018. URL: <https://www.piezodata.com/7-facts-you-should-know-about-double-sheet-sensors/>.

- [32] SICK Sensor Intelligence. *Double-sheet detector*. 2024. URL: <https://www.sick.com/dk/en/industries/consumer-goods/paper-and-print/press/double-sheet-detector/c/p350013>.
- [33] Magnetic Magazine. *Goudsmit Develops Steel Sheet Separator with Fail-Safe Magnet & Assists Hyperloop Project in Netherlands*. 2020. URL: <https://magneticmag.com/goudsmit-develops-steel-sheet-separator-with-fail-safe-magnet-assists-hyperloop-project-in-netherlands/>.
- [34] Solvair. *How Air Knife Systems Work*. 2024. URL: <https://solvair.co.uk/resource/how-air-knife-systems-work/>.
- [35] Carlo Boeve. *Magic Gripper internship report*. May 2024.
- [36] et al. B. Olofsson. "Method and apparatus for destacking sheet metal members". In: *European Patent Office* (Dec. 1998).
- [37] N. Hall. *Boyle's Law*. Nov. 2024. URL: <https://www1.grc.nasa.gov/beginners-guide-to-aeronautics/boyles-law/>.
- [38] M. van Biezen. *Calculus #3: Find Volume=? by Revolving Area Around y-Axis*. Sept. 2020. URL: <https://www.youtube.com/watch?v=gdIuUhuq7SM>.
- [39] Sugna Premium Steel. *What is young's modulus of steel?* June 2023. URL: <https://sugnatmt.com/youngs-modulus-of-steel/#:~:text=When%20it%20comes%20to%20its,bend%20or%20stretch%20under%20stress..>
- [40] NumPy Developers. *numpy.polyfit*. 2024. URL: <https://numpy.org/doc/stable/reference/generated/numpy.polyfit.html>.
- [41] D. Craig Brinck. *Welcome to Pynite's Documentation*. 2023. URL: <https://pynite.readthedocs.io/en/latest/>.
- [42] SteelOnCall. *What Is Young's Modulus Of Steel?* 2024. URL: [https://steeloncall.com/what-is-young-s-modulus-of-steel#:~:text=Young's%20modulus%20of%20steel%20at,and%20215%20GPA%20\(31200\)..](https://steeloncall.com/what-is-young-s-modulus-of-steel#:~:text=Young's%20modulus%20of%20steel%20at,and%20215%20GPA%20(31200)..)
- [43] AmesWeb. *MODULUS OF RIGIDITY (SHEAR MODULUS)*. 2025. URL: <https://amesweb.info/StressStrainTransformations/Shear-Modulus-of-Rigidity.aspx>.
- [44] The Engineering ToolBox. *Poisson's Ratio - Definition, Values for Materials, and Applications*. 2025. URL: https://www.engineeringtoolbox.com/poissons-ratio-d_1224.html.
- [45] Solitaire Overseas. *Density of Steel - Mild and Carbon Density of Steel lb/in³*. 2019. URL: <https://www.solitaire-overseas.com/blog/density-of-steel/#:~:text=Steel%20has%20a%20density%20of,490%20pounds%20per%20cubic%20foot..>
- [46] The SciPy community. *curvefit*. 2025. URL: https://docs.scipy.org/doc/scipy/reference/generated/scipy.optimize.curve_fit.html.
- [47] SteelOnCall.com. *What Is Young's Modulus Of Steel?* May 2020. URL: <https://steeloncall.com/what-is-young-s-modulus-of-steel#:~:text=Young's%20modulus%20of%20steel%20at,underneath%20as%20far%20as%20possible..>

Appendix A

Interviews

A.1 Interview questions

- Can you describe a specific situation where the destacking of products was not successful because the parts would stick together?
 - For which kind of parts did this problem occur? (material, shape, size, thickness, oil layer, plastic coating, etc.)
 - Which type of grippers / effectors were used?
 - Have you observed factors that had a direct effect on the amount of sticking between the parts?
 - * Location in stack.
 - * Parts with burrs.
 - * Prior processing of the part.
- What actions were taken to try to solve the destacking issue?
 - How effective were these actions and why?
- What do you think are the main factors that contribute to the occurrence of the destacking problem?
 - According to you, which of these factors needs to be researched further, to increase our understanding?
- How would you approach solving the destacking issue?

A.2 Respondent A transcript

- Interviewer: Can you describe a specific situation where the destacking of products was unsuccessful due to sticking products?
- Respondent: Yes, one of our American customers works with metal parts that have a thickness of around one millimeter. At this customer, our robot tried to destack the parts with a conventional approach. Meaning that its approach and departs from the stack was straight

down and upward, respectively. Conventional effector placement was also used, meaning that the two effectors were divided over the middle of the part to equally distribute the weight.

- Interview: What kind of effectors were used?
- Respondent: We used foam vacuum pads as effectors. These pads have multiple holes in them, allowing the pads to retain their holding force even if a section of the pad was not connected to the part. These two vacuum pads are mounted to a 'stretchgripper', meaning that the effector distance can be changed dynamically within a specific range. The vacuum pads that we used also did not have any angle to them with respect to the product.

Using this approach, we often observed that parts were sticking to each other.

- Interviewer: What are the dimensions of these sticking products?
- Respondent: This customer has a large variety of product dimensions. The product that caused us the most destacking issues, has a length of 1600 millimeters and a width of 1400 millimeters. So a large rectangular thin metal sheet.

- Interviewer: Was the destacking issue more severe for larger products?

- Respondent: For this customer, this was the case indeed. Larger products with the same thickness are less rigid and almost behave like a sheet of paper. For the product I just described, five products would be destacked at once. When the robot then moved from the stack, the parts would fall to the ground one by one and be destroyed.

During testing at this customer, the destacking problem kept becoming worse. I suspect that this had to do with the deburring machine that the parts would pass through before arriving at the robot. Since the robot is part of a fully automated production line, the output parts would travel through this deburring machine in the same direction and orientation every time before returning again at our robot cell. Since we were testing continuously, the test parts would pass through the same deburring machine countless of times. The deburring machine works by aggressively brushing the surface in the same direction. The parts would also be very hot when exiting the deburring machine. I can therefore imagine that the parts would obtain residual magnetism by passing through this deburring machine many times. Magnetized parts can contribute to the sticking effect. This would also explain why the problem would keep getting worse when the products kept going through the deburring machine.

- Interviewer: Where these products ferritic?
- Respondent: Yes these products were ferritic. I have not measured if the parts were actually residually magnetic but I do suspect that this was contributing to the sticking problem.

Since the problem kept on becoming worse, we eventually sent the cart that was supplying the parts away. This cart with parts would then continue to another robotics team and this team would also give feedback that these parts were exceptionally sticky.

Having said that, we also worked with products that did not go through the deburring machine and the destacking problem would sometimes occur even for these products. So I do not think that the deburring machine is the main cause of the problem but I do think it amplifies it.

- Interviewer: Did you observe this destacking problem for products that did not go through a deburring machine at the same customer or somewhere else?

- Respondent: This was all at the same customer.

In a recent example for this customer, they were handling smaller products of 650 millimeters long and 300 millimeters wide. These products were also sticking together and then separating from the gripper while the robot was moving, resulting in shattered products across the robot cell.

- Interviewer: What can you say about the surface of these products? Were these products rough or smooth, was there an oil layer or an plastic coating on the products?

- Respondent: From what I remember, these products were very smooth. The laser cutter that was cutting these products was set to a lower speed that it is capable of, resulting in products without any burrs. So these products are already super thin, do not have any burrs and the product stacks are compressed by a machine that comes before the robot cell. These products did not contain any oil or plastic coatings.

At one point there was a colleague from a related company that had degreased all parts in the stack to remove any oil or grease residues. Despite this effort, the parts would still stick after degreasing.

- Interviewer: Okay, so you do not think that fluid forces from oil between parts are the main factor that cause the destacking problem?

- Respondent: No indeed.

- Interviewer: What do you think is the main factor that is contributing to the sticking effect?

- Respondent: I suspect that a vacuum that builds up between the parts is the main factor contributing to the sticking effect. However, I am also not completely sure why it happens.

What we did notice, is that the problem would be more pronounced for parts that are lower in a stack.

- Interviewer: Why do you think this is the case?

- Respondent: Because these products have been more compressed. This compressive force can be caused by the products that lie on top of it. The compressive forces can also be caused by the robot during stacking. The robots are not perfect and might press down on the stack every time a part is stacked, consequently squeezing the stack below.

- Interviewer: Why do you think that compressive forces on a stack will amplify the destacking problem?

- Respondent: Because compressive forces push any remaining air out from between the parts. This is why products with burrs will be less susceptible to the destacking problem since these products will not stack as nicely, creating a small air layer in between the parts.

This is also what we heard from other companies that were working with robots at the same customers: never put pressure on the stack because it will cause all products to stick together.

For me, I always try to reason from how a person would destack such a part. I would start by peeling it at one of the corners to break the seal between the parts. I think that compressing the parts would only increase the strength of this seal.

- Interview: So there was a seal present between the products, but this was not an oil seal since there was no oil present?
- Respondent: Indeed, there was no oil present.
- Interviewer: These must have been rather smooth parts then. Were these products so smooth that you could see your own reflection in them?
- Respondent: This was almost the case indeed, the products were even smoother when exiting the deburring machine. The products were practically polished.

Just the fact that these products are so thin also makes it difficult to handle. We have tested here with products that are 1.5 millimeters thick but products that are 0.8 or 0.9 millimeters thick are considerably more flexible, especially if they are large.

- Interviewer: What actions were taken to solve the destacking issue?
- Respondent: We started by adjusting the way the robot approaches the product for destacking to avoid compressing the stack. We did this by hovering above the part and engaging the vacuum pads. Then we would slowly move downward until we essentially would suck up the top part. The downward movement would then stop because of the sensors that are installed on the gripper that can sense that a product is attached. One downside to this technique is that these pickup sensors needs to be calibrated very precisely. If one of the sensors fails or one of the sensor brackets is bend, the robot would just continue to move downward and compress the stack. This approach deemed unsuccessful since multiple products would still stick together during destacking.

In our second approach we tried to rotate around one of the effectors. This was done by rotating the gripper around one the effectors in such a way that the other effector would move upward from the stack. This would induce a bending moment in the attached parts that would separate any sticking parts.

This second approach would work successfully some of the time. One of the main problems with this system is that I can not know if the destacking was successful or not. We do not have any sensor on the gripper that can detect if the attached product is only on product or actually two products that stick together. If a double sheet detection system was installed I would be able to stop the system when a double sheet would be picked up.

As an addition to the second approach we would implement an extra downward movement. This would press the angled products back on the stack, increasing the bending moment. This would sometimes cause the remaining sticking parts to separate. However, this step puts extra compressive pressure on the stack, which is undesirable.

After the second approach, the robot rotates the gripper back to a straight position and then waits a few second above the stack. In this wait, some parts would still separate and fall back on the stack. After the wait, the robot would move to the output location, and even then there would still be extra sticking parts falling to the ground.

Since nothing seemed to work, we even tried to shake any sticking parts from the gripper. After picking up the top product the robot would then shake the gripper up and down in an attempt to loose the attached parts. In reality this was an unsuccessful and quite aggressive moment since the products are very large. Even with this aggressive shaking movement and waiting thirty seconds above the stack, another four parts would fall down in the cell when

moving to the output location. So it is safe to say that the destacking problem was severe at this customer.

Another problem we ran into is the presence of large holes in products. This approach of using the bending moment inside a product is relying on a certain degree of stiffness in the products. However, if there is a large slot or hole in a product, it can drastically influence the stiffness along a certain direction. Because of this, we would have to specify the specific effector locations on the product for some products that contained such holes.

Another effect that can influence destacking is when you have holes that you cannot detect with your system, you can easily place a vacuum pad on this location. This can cause complete loss of pressure but it can also attract underlying products through the partial vacuum in this hole.

One other thing we tried is the use of angled vacuum pads. This proved a challenge to implement since one side of the vacuum pad would be pressing down on the stack while the outer side would not yet touch the stack. The top products would therefore need to be compressed in order to make a good seal with the angled vacuum pad. When moving upward the top product would be bent downward. However, even with this bending multiple products would still attach to the top product.

- Interviewer: You were just talking about products with burrs and how these burrs would contribute to a small air layer between the products. Do you think that these burrs can also mechanically interlock and form a strong seal if they are stacked neatly?
- Respondent: Yes that is something I can imagine. However, how I see it, it would rather form a kind of distanced stack where each burr would not interlock but create a small air gap with the plate above.
- Interviewer: How would you go about solving the destacking issue within an industrial automation setting?
- Respondent: From my point of view you will need a gripper that is able successfully to destack products 100% of the time. And if that is not possible, you will need some kind of system that can detect if double products have been picked up.

If I can detect double sheets, I can program the robot to put the parts back on the stack and try again for example. If this retry is then unsuccessful I can send an notification to the operator. Now, I don't know when the destacking was successful or unsuccessful and I just have to assume the worst case scenario which has a large impact on the runtime.

- Interviewer: Would you say that detecting double sheet pickups is even more important than destacking one by one itself?
- Respondent: Double sheet detection would allow me to improve the current system significantly yes.
- Interviewer: How would you envision such a double sheet detection system?
- Respondent: The most important thing is that you should be able to detect double sheet pickups when you are still above the stack because you want to minimize the chance of falling products on the cell floor.

A lot of possibilities for double sheet detection systems that we looked at require the robot to first move the part to the location where the detection can be done.

- Interviewer: There are double sheet detection systems that only require one ultrasonic probe on one side of the product to detect a double sheet. Would such a sensor then be suitable?
- Respondent: Yes, but I think that such systems are often calibrated for just one plate thickness, limiting their flexibility.
- Interviewer: How would you try to solve the destacking problem yourself?
- Respondent: I would approach the problem by asking myself how I would destack the sheets manually. I would start with breaking the seal between the products somewhere along the edges
- Interviewer: Would you chose for a peeling or separation mechanism that is mechanical, uses magnets or uses vacuum pads?
- Respondent: I think it is easiest to use vacuum effectors. Because what I see from experience is that placing the vacuum effectors on the edges of a product with angled vacuum pads seems to work relatively well.

One other approach that we have thought about is using a linear actuator that can pull one of the effectors upward at the product edge. This would break the seal between the products. The downside to this approach is that there exist product shapes where it is almost impossible to find suitable effector locations. Another problem occurs when vacuum grippers land on some holes. Then the partial vacuum can create a suction force on multiple parts of the stack, increasing their tendency to stick to the gripper.

- Interviewer: Have you ever considered vacuum effectors that use rubber seals instead of the foam seal that we currently use?
- Respondent: Well, it is interesting too see that other robot companies that also operate at this customer do use more traditional suction cups. However, the grippers of these companies tend to be less flexible in product shapes than our grippers.

Another interesting approach would be a two-steps separation. Where the seal underneath the top products is first broken. And that the second step is the destacking step.

- Interviewer: Yes that is an interesting approach as well. Would you then not be worried the part seals again after the first step.
- Respondent: Yes that could be the case indeed.
- Interviewer: Okay I think that I have discussed everything I wanted.
- Respondent: Yes, so I think that detecting the double sheets during destacking is one of the most important advancements of the system. This advancement would make the system a lot more robust and stop us from breaking parts because they fall on the ground.
- Interviewer: For the design of a solution, the latest stretchgripper design included two magnets that can both be rotated outward. Would you then suggest to continue with this design, but then with vacuum pads instead of magnets?
- Respondent: Yes, I think that using vacuum is the right approach. You should however be careful to not break the seal between the vacuum pads and the top product during bending or moving.

- Interviewer: I was also thinking that some kind of vibration on the effectors might help with breaking the seal underneath the top product. What are your thoughts on this?
- Respondent: Yes I have also heard about this concept. I saw a video from Trumpf where they also used vibrations to remove parts from a laser-cut bed. A similar device might indeed be suitable for separating the top part from the rest of the stack.
Another idea is to request from the prior production line to stack the parts in such a way that every part is slightly shifted with respect to the previous. This would make it easier to break the seal between the parts.
- Interviewer: Yes that is indeed an interesting idea. The downside of course then being that the rest of the factory has to adjust to our robot.
I think that I have asked all the questions that I wanted to ask you. Do you yourself have any final remarks regarding the subject?
- Respondent: Yes, that this problem is still present at our customer and we are now coming to a conclusion that our solution does not work reliably enough. So it underscores the importance of this subject.
- Interviewer: Yes it is indeed an important problem to be solved. I want to thank you for your time and participation in the interview.
- Respondent: No problem, thank you.

A.3 Respondent B transcript

- Interviewer: Can you describe a specific situation where you encountered this destacking issue in practice?
- Respondent: Yeah, we have this customer in Germany and they have quite large products, maybe one and a half meters in length. These products were sticking quite a lot. A problem presented itself when the products turned out to stick together because the old vacuum gripper simply wasn't strong enough to pick them up from the stack. So it was not like we were picking up multiple products at once, we were not able to pick up any products due to the sticking. So it is a little bit of a different problem than when you have smaller products.
We initially thought the vacuum on the vacuum pads was not strong enough but after some investigation the customer concluded that the products were not being picked up because the products were sticking together. These products are a little bit oily as well and if you have oil then that often makes it worse. Especially if there is no air between the parts and when the parts are oily, the parts become very sticky.
So, then we came up with a new large peeling stretchgripper concept. This gripper has four vacuum pads and the outer two are mounted higher than the inner two. That height difference naturally creates a peeling motion when you try to pick up a large product. This new gripper has worked very successfully for these larger products.
- Interviewer: How large were these products that you are talking about, you mentioned a length of one and a half meters?

- Respondent: Yes, something like that and maybe three millimeters or so thick. So they bend easily with that larger peelgripper.
- Interviewer: Do you know what kind of material the sheets were made of?
- Respondent: It might be stainless steel but I am not certain.
- Interviewer: Do you know if the material is ferritic?
- Respondent: No, I don't.
- Interviewer: And this oily layer, do you know how this oil was applied to the sheets? And how thick the layer is?
- Respondent: No, I also don't know that. But I think you can test if the products are ferritic because they are in cell 5. So, you just find a magnet and see if it sticks.
- Interviewer: Yes, and what type of grippers were used? You mentioned that you first used the smaller vacuum grippers?
- Respondent: So, we used the large stretch vacuum gripper that we have. So the vacuum pads are maybe twenty centimeters long and fifteen centimeters wide or something like that. This gripper has two pads and is rated for thirty kilos. So it is decently strong but it was unable to pick up the large products from the stack due to the sticking between the parts.
- Interviewer: Okay, and have you observed factors that directly affect the extent of this destacking problem?
- Respondent: If the products are oily, that is a big one. The material type and how the products have been cut is also important. If you have thick products that have been cut by an oxygen cutter, you will always have slag and other bits of scrap in between the parts. Then you never have this problem.
So, it is probably with laser-cut products that give you a very nice clean cut that you experience the problem. I am not sure where the oil comes from in the production process. Maybe the parts have gone through some sort of flattening or deburring process before our machines get to them, maybe that is where the oil comes from. If surfaces are very clean and smooth, especially when there is oil between the parts, you encounter this issue.
- Interviewer: Okay, and have you seen effects of the part location in a stack? So, is there a difference in sticking between one of the top plates or one of the bottom plates?
- Respondent: No I have not seen this effect but I would assume that if you have a tall stack the bottom parts would be stickier. Just because there would be more weight on those parts. This weight would be more likely to push out any remaining air between the sheets.
But I think generally, if you have problems with the bottom of the stack you will also have problems with the top of the stack. For these sort of problems it is not acceptable to solve it for 99% reliability. Because then you have problems still happening way too often. You need to solve it with 99.9% or 99.999% reliability and then you can be happy.
- Interviewer: Okay, and if you have products with burrs as a result from the punching process, have you seen effects of these burrs on the destacking?

- Respondent: You won't have any issues with such products because the touching surface area between stacked products will be very small. As soon as you have a burr, you will have an air gap between the products. I guess, if it is a very thin product with burrs it would be a bit sticky in the middle but still easily peel up because it has the air gaps from the burrs on the outside.

Then, the only problem you might have with sticking happens when you pick up ferritic products with a magnetic gripper and the magnet is too strong. The magnet will then attract multiple products at once. Which, I guess, is an entirely separate problem.

- Interviewer: And in a situation where the punched parts with burrs would be precisely stacked by a robot, the burrs could mechanically interlock. So that the seal strength would be increased because the parts interlock like puzzle pieces. Do you think that could be a problem?
- Respondent: I doubt it, because the burrs are never the same between the products. I do not think you could have burrs interlocking like that.
- Interviewer: Okay, so it would almost always be beneficial for the destacking problem if the products have burrs?
- Respondent: Yes, I have never seen products with burrs that have these destacking problems.
- Interviewer: So the thin products that we work with the most are laser-cut can not punched?
- Respondent: Yes.
- Interviewer: Okay, and what was your involvement in the American customer that also experiences these destacking problems?

- Respondent: While other colleagues were on site, I supplied support from here. We don't have any dedicated peeling grippers at that customer so we have tried various approaches to solving the problem in another way.

We tried picking up the products and then just waiting for attaching products to fall down. We tried shaking the gripper to make the additional parts fall off. Sometimes this works, and sometimes it doesn't.

We also tried some kind of peeling motion with the regular gripper. In this motion you go down, you lift one vacuum pad up and keep the other one on the product. Sometimes that works, but sometimes it doesn't.

- Interviewer: Okay, so the idea is again to induce some kind of spring force in the product?
- Respondent: Yes, exactly.

Even if you had a gripper that could peel up from both edges of the product at the same time, like a miniature version of the large peeling gripper, I am not sure it could destack smaller products reliably. Smaller products that are maybe fifteen centimeters long are not so flexible. So then you would need quite a strong vacuum for the peeling. I think it would be possible but you would need more research and development and probably some strong suction cups because you will need more strength to bend the product. The overall rigidity will be a challenge with destacking smaller products.

- Interviewer: Have you seen a correlation between the product area size and the extend of the destacking problem?

- Respondent: I don't really know. I think it is worse for our American customer for smaller products but that is more of a gut feeling than observed facts.
I know that some of the products of the American customer are 1300 by 1300 millimeters. So maybe if you grab the diagonal corners of this large product, it would bend enough by itself to separate from the rest of the stack.
- Interviewer: Okay, and were there any other actions taken to solve the destacking problem in practice that we did not discuss yet?
- Respondent: No, I don't think so.
- Interviewer: What do you think are the main factors that contribute to the destacking problem?
- Respondent: Fundamentally, it is just a lack of air between the products which causes the products to pull each other up. So there is a partial vacuum and a seal between the products when the products are very clean and have a very smooth surface. Somehow, you need to break that seal and that is the fundamental issue.
- Interviewer: So the destacking issue can also occur if there is not any oil between the products?
- Respondent: Yes. So, generally those are laser-cut aluminium or stainless steel products.
- Interviewer: Okay, and in terms of research. Which areas of this topic would require more research in your opinion?
- Respondent: Yes, so I think there are a few avenues of research and development that we can take. If you consider the problem of wanting to destack small non-ferritic products, then you cannot use a magnet as a plate separator because the parts are non-ferritic. The only solution then is vacuum grippers. So we may want to design a vacuum gripper that is as strong as possible to be able to peel these products up, to see how well it works in practice. For this, you will need small strong suction cups. If you would use vacuum pads that are ten by ten centimeters, they might not fit nicely on the corners of the products.
- Interviewer: So you would suggest a peeling motion using vacuum effectors. And in terms of effector locations on the product, what would you suggest?
- Respondent: I think that placing the effectors diagonally across the longest axis of the product would yield the best results. Such a placement would make the part the easiest to bend.
So what you might want is a vacuum gripper with three effectors. One in the middle and two on the edges that are slightly higher than the one in the middle. I think that is how you can generate your peeling motion.
- Interviewer: Okay, and what are your thoughts on the latest peelgripper that was made here with the air cylinders on the side and the rotatable magnets?
- Respondent: It is just a magnetic version of the vacuum peelgripper that I suggested. But the problem with magnets is that you are restricted to magnetic products and if your magnet is too strong you will pick up multiple products at once. So I think vacuum gripper are the way to go.
- Interviewer: So you would suggest a similar construction as the latest version but than with vacuum effectors?

- Respondent: Yes, I think that is the best way to handle as many products as possible.
There will always be edge cases that we can't handle. But we can at least solve that as best as we can by providing the machine operators good tools to test which products do and don't work with the grippers. For our latest customer we have done that by giving them a tool to teach the appropriate pickup locations for all the stacks. So after you have scanned the pallets you can teach the robot where exactly it needs to pickup the products. We have solved it there in this manner because their products often have such small holes that we cannot detect them.
- Interviewer: Okay, how exactly does this teaching of pickup locations work in practice?
- Respondent: After we have scanned the pallets with the scanner, the operators gets a popup window on his computer screen. In this window, the operator can select which gripper to use and then they can choose where the gripper pickup positions should be on the products. This is a visual interface.
- Interviewer: Okay, thank you for your input. For me these were all the questions I wanted to ask today. Are there for you any more remarks on this subject?
- Respondent: No, I think I have said basically everything I know.
- Interviewer: Okay, thank you for participating.

Appendix B

Derivation area moment of inertia

$I_{y'}$

$$I_{y'} = \int_{-l}^l z^2 dA + Ad^2 \quad (\text{B.1})$$

$$I_{y'} = 2h \int_0^l z^2 dy + Ad^2 \quad (\text{B.2})$$

$$I_{y'} = 2h \int_0^l v^2(y) dy + Ad^2 \quad (\text{B.3})$$

$$I_{y'} = 2h \int_0^l v^2(y) dy + hld^2 \quad (\text{B.4})$$

$$I_{y'} = 2h \int_0^l v^2(y) dy + hl \left(\frac{1}{2}v(0) \right)^2 \quad (\text{B.5})$$

$$I_{y'} = 2h \int_0^l v^2(y) dy + \frac{1}{4}hlv(0)^2 \quad (\text{B.6})$$

$$v(y) = \frac{1}{EI_{y'}} \left(-\frac{1}{24}fy^4 + \frac{1}{6}F_{\text{pull}}y^3 + \frac{1}{4}fl^2y^2 - \frac{1}{2}F_{\text{pull}}ly^2 - \frac{5}{24}fl^4 + \frac{1}{3}F_{\text{pull}}l^3 \right) \quad (\text{B.7})$$

$$I_{y'} = 2h \int_0^l \left(\frac{1}{EI_{y'}} \left(-\frac{1}{24}fy^4 + \frac{1}{6}F_{\text{pull}}y^3 + \frac{1}{4}fl^2y^2 - \frac{1}{2}F_{\text{pull}}ly^2 - \frac{5}{24}fl^4 + \frac{1}{3}F_{\text{pull}}l^3 \right) \right)^2 dy + \frac{1}{4}hl \left(\frac{1}{EI_{y'}} \left(-\frac{5}{24}fl^4 + \frac{1}{3}F_{\text{pull}}l^3 \right) \right)^2 \quad (\text{B.8})$$

$$I_{y'} = \frac{2h}{E^2I_{y'}^2} \int_0^l \left(-\frac{1}{24}fy^4 + \frac{1}{6}F_{\text{pull}}y^3 + \frac{1}{4}fl^2y^2 - \frac{1}{2}F_{\text{pull}}ly^2 - \frac{5}{24}fl^4 + \frac{1}{3}F_{\text{pull}}l^3 \right)^2 dy + \frac{hl}{4E^2I_{y'}^2} \left(-\frac{5}{24}fl^4 + \frac{1}{3}F_{\text{pull}}l^3 \right)^2 \quad (\text{B.9})$$

$$I_{y'} = \frac{2h}{E^2I_{y'}^2} \int_0^l \left(-\frac{1}{24}fy^4 + \frac{1}{6}F_{\text{pull}}y^3 + \frac{1}{4}fl^2y^2 - \frac{1}{2}F_{\text{pull}}ly^2 - \frac{5}{24}fl^4 + \frac{1}{3}F_{\text{pull}}l^3 \right)^2 dy + \frac{hl}{4E^2I_{y'}^2} \left(-\frac{5}{24}fl^4 + \frac{1}{3}F_{\text{pull}}l^3 \right)^2 \quad 88 \quad (\text{B.10})$$

$$I_{y'} = \frac{2h}{E^2I_{y'}^2} \int_0^l \left(-\frac{1}{24}fy^4 + \frac{1}{6}F_{\text{pull}}y^3 + \frac{1}{4}fl^2y^2 - \frac{1}{2}F_{\text{pull}}ly^2 - \frac{5}{24}fl^4 + \frac{1}{3}F_{\text{pull}}l^3 \right) \cdot \left(-\frac{1}{24}fy^4 + \frac{1}{6}F_{\text{pull}}y^3 + \frac{1}{4}fl^2y^2 - \frac{1}{2}F_{\text{pull}}ly^2 - \frac{5}{24}fl^4 + \frac{1}{3}F_{\text{pull}}l^3 \right) dy + \frac{hl}{4E^2I_{y'}^2} \left(-\frac{5}{24}fl^4 + \frac{1}{3}F_{\text{pull}}l^3 \right)^2 \quad (\text{B.11})$$

$$\begin{aligned}
I_{y'} &= \frac{2h}{E^2 I_{y'}^2} \int_0^l \left(-\frac{1}{24} f y^4 \left(-\frac{1}{24} f y^4 + \frac{1}{6} F_{\text{pull}} y^3 + \frac{1}{4} f l^2 y^2 - \frac{1}{2} F_{\text{pull}} l y^2 - \frac{5}{24} f l^4 + \frac{1}{3} F_{\text{pull}} l^3 \right) \right. \\
&\quad + \frac{1}{6} F_{\text{pull}} y^3 \left(-\frac{1}{24} f y^4 + \frac{1}{6} F_{\text{pull}} y^3 + \frac{1}{4} f l^2 y^2 - \frac{1}{2} F_{\text{pull}} l y^2 - \frac{5}{24} f l^4 + \frac{1}{3} F_{\text{pull}} l^3 \right) \\
&\quad + \frac{1}{4} f l^2 y^2 \left(-\frac{1}{24} f y^4 + \frac{1}{6} F_{\text{pull}} y^3 + \frac{1}{4} f l^2 y^2 - \frac{1}{2} F_{\text{pull}} l y^2 - \frac{5}{24} f l^4 + \frac{1}{3} F_{\text{pull}} l^3 \right) \\
&\quad - \frac{1}{2} F_{\text{pull}} l y^2 \left(-\frac{1}{24} f y^4 + \frac{1}{6} F_{\text{pull}} y^3 + \frac{1}{4} f l^2 y^2 - \frac{1}{2} F_{\text{pull}} l y^2 - \frac{5}{24} f l^4 + \frac{1}{3} F_{\text{pull}} l^3 \right) \\
&\quad - \frac{5}{24} f l^4 \left(-\frac{1}{24} f y^4 + \frac{1}{6} F_{\text{pull}} y^3 + \frac{1}{4} f l^2 y^2 - \frac{1}{2} F_{\text{pull}} l y^2 - \frac{5}{24} f l^4 + \frac{1}{3} F_{\text{pull}} l^3 \right) \\
&\quad \left. + \frac{1}{3} F_{\text{pull}} l^3 \left(-\frac{1}{24} f y^4 + \frac{1}{6} F_{\text{pull}} y^3 + \frac{1}{4} f l^2 y^2 - \frac{1}{2} F_{\text{pull}} l y^2 - \frac{5}{24} f l^4 + \frac{1}{3} F_{\text{pull}} l^3 \right) \right) dy \\
&\quad + \frac{hl}{4E^2 I_{y'}^2} \left(-\frac{5}{24} f l^4 + \frac{1}{3} F_{\text{pull}} l^3 \right)^2
\end{aligned} \tag{B.12}$$

$$\begin{aligned}
I_{y'} &= \frac{2h}{E^2 I_{y'}^2} \int_0^l \left(\frac{1}{576} f^2 y^8 - \frac{1}{144} f F_{\text{pull}} y^7 - \frac{1}{96} f^2 l^2 y^6 + \frac{1}{48} f F_{\text{pull}} l y^6 + \frac{5}{576} f^2 l^4 y^4 - \frac{1}{72} f F_{\text{pull}} l^3 y^4 \right. \\
&\quad - \frac{1}{144} F_{\text{pull}} f y^7 + \frac{1}{36} F_{\text{pull}}^2 y^6 + \frac{1}{24} F_{\text{pull}} f l^2 y^5 - \frac{1}{12} F_{\text{pull}}^2 l y^5 - \frac{5}{144} F_{\text{pull}} f l^4 y^3 + \frac{1}{18} F_{\text{pull}}^2 l^3 y^3 \\
&\quad - \frac{1}{96} f^2 l^2 y^6 + \frac{1}{24} f l^2 F_{\text{pull}} y^5 + \frac{1}{16} f^2 l^4 y^4 - \frac{1}{8} f F_{\text{pull}} l^3 y^4 - \frac{5}{96} f^2 l^6 y^2 + \frac{1}{12} f F_{\text{pull}} l^5 y^2 \\
&\quad + \frac{1}{48} F_{\text{pull}} l f y^6 - \frac{1}{12} F_{\text{pull}}^2 l y^5 - \frac{1}{8} F_{\text{pull}} f l^3 y^4 + \frac{1}{4} F_{\text{pull}}^2 l^2 y^4 + \frac{5}{48} F_{\text{pull}} f l^5 y^2 - \frac{1}{6} F_{\text{pull}}^2 l^4 y^2 \\
&\quad + \frac{5}{576} l^4 f^2 y^4 - \frac{5}{144} f l^4 F_{\text{pull}} y^3 - \frac{5}{96} f^2 l^6 y^2 + \frac{5}{48} f F_{\text{pull}} l^5 y^2 + \frac{25}{576} f^2 l^8 - \frac{5}{72} f F_{\text{pull}} l^7 \\
&\quad \left. - \frac{1}{72} F_{\text{pull}} l^3 f y^4 + \frac{1}{18} F_{\text{pull}}^2 l^3 y^3 + \frac{1}{12} F_{\text{pull}} f l^5 y^2 - \frac{1}{6} F_{\text{pull}}^2 l^4 y^2 - \frac{5}{72} F_{\text{pull}} f l^7 + \frac{1}{9} F_{\text{pull}}^2 l^6 \right) dy \\
&\quad + \frac{hl}{4E^2 I_{y'}^2} \left(-\frac{5}{24} f l^4 + \frac{1}{3} F_{\text{pull}} l^3 \right)^2
\end{aligned} \tag{B.13}$$

$$\begin{aligned}
I_{y'} &= \frac{2h}{E^2 I_{y'}^2} \int_0^l \left(\frac{1}{576} f^2 y^8 - \frac{1}{72} f F_{\text{pull}} y^7 + \left(-\frac{1}{48} f^2 l^2 + \frac{1}{24} f F_{\text{pull}} l + \frac{1}{36} F_{\text{pull}}^2 \right) y^6 \right. \\
&\quad + \left(\frac{1}{12} F_{\text{pull}} f l^2 - \frac{1}{6} F_{\text{pull}}^2 l \right) y^5 + \left(\frac{23}{288} f^2 l^4 - \frac{5}{18} f F_{\text{pull}} l^3 + \frac{1}{4} F_{\text{pull}}^2 l^2 \right) y^4 \\
&\quad + \left(-\frac{5}{72} F_{\text{pull}} f l^4 + \frac{1}{9} F_{\text{pull}}^2 l^3 \right) y^3 + \left(-\frac{5}{48} f^2 l^6 + \frac{3}{8} f F_{\text{pull}} l^5 - \frac{1}{3} F_{\text{pull}}^2 l^4 \right) y^2 \\
&\quad \left. + \frac{25}{576} f^2 l^8 - \frac{5}{36} F_{\text{pull}} f l^7 + \frac{1}{9} F_{\text{pull}}^2 l^6 \right) dy \\
&\quad + \frac{hl}{4E^2 I_{y'}^2} \left(-\frac{5}{24} f l^4 + \frac{1}{3} F_{\text{pull}} l^3 \right)^2
\end{aligned} \tag{B.14}$$

$$\begin{aligned}
I_{y'} &= \frac{2h}{E^2 I_{y'}^2} \left[\frac{1}{5184} f^2 y^9 - \frac{1}{576} f F_{\text{pull}} y^8 + \left(-\frac{1}{336} f^2 l^2 + \frac{1}{168} f F_{\text{pull}} l + \frac{1}{252} F_{\text{pull}}^2 \right) y^7 \right. \\
&+ \left(\frac{1}{72} F_{\text{pull}} f l^2 - \frac{1}{36} F_{\text{pull}}^2 l \right) y^6 + \left(\frac{23}{1440} f^2 l^4 - \frac{1}{18} f F_{\text{pull}} l^3 + \frac{1}{20} F_{\text{pull}}^2 l^2 \right) y^5 \\
&+ \left(-\frac{5}{288} F_{\text{pull}} f l^4 + \frac{1}{36} F_{\text{pull}}^2 l^3 \right) y^4 + \left(-\frac{5}{144} f^2 l^6 + \frac{1}{8} f F_{\text{pull}} l^5 - \frac{1}{9} F_{\text{pull}}^2 l^4 \right) y^3 \\
&+ \left. \frac{25}{576} f^2 l^8 y - \frac{5}{36} F_{\text{pull}} f l^7 y + \frac{1}{9} F_{\text{pull}}^2 l^6 y \right]_0^l \\
&+ \frac{hl}{4E^2 I_{y'}^2} \left(-\frac{5}{24} f l^4 + \frac{1}{3} F_{\text{pull}} l^3 \right)^2
\end{aligned} \tag{B.15}$$

$$\begin{aligned}
I_{y'} &= \frac{2h}{E^2 I_{y'}^2} \left(\frac{1}{5184} f^2 l^9 - \frac{1}{576} f F_{\text{pull}} l^8 + \left(-\frac{1}{336} f^2 l^2 + \frac{1}{168} f F_{\text{pull}} l + \frac{1}{252} F_{\text{pull}}^2 \right) l^7 \right. \\
&+ \left(\frac{1}{72} F_{\text{pull}} f l - \frac{1}{36} F_{\text{pull}}^2 \right) l^7 + \left(\frac{23}{1440} f^2 l^2 - \frac{1}{18} f F_{\text{pull}} l + \frac{1}{20} F_{\text{pull}}^2 \right) l^7 \\
&+ \left(-\frac{5}{288} F_{\text{pull}} f l + \frac{1}{36} F_{\text{pull}}^2 \right) l^7 + \left(-\frac{5}{144} f^2 l^2 + \frac{1}{8} f F_{\text{pull}} l - \frac{1}{9} F_{\text{pull}}^2 \right) l^7 \\
&+ \left. \frac{25}{576} f^2 l^9 - \frac{5}{36} F_{\text{pull}} f l^8 + \frac{1}{9} F_{\text{pull}}^2 l^7 \right) \\
&+ \frac{hl}{4E^2 I_{y'}^2} \left(\frac{25}{576} f^2 l^8 - \frac{5}{72} f F_{\text{pull}} l^7 + \frac{1}{9} F_{\text{pull}}^2 l^6 \right)
\end{aligned} \tag{B.16}$$

$$\begin{aligned}
I_{y'} &= \frac{hl^7}{E^2 I_{y'}^2} \left(\frac{1}{2592} f^2 l^2 - \frac{1}{288} f F_{\text{pull}} l - \frac{1}{168} f^2 l^2 + \frac{1}{84} f F_{\text{pull}} l + \frac{1}{126} F_{\text{pull}}^2 \right. \\
&+ \frac{1}{36} F_{\text{pull}} f l - \frac{1}{18} F_{\text{pull}}^2 + \frac{23}{720} f^2 l^2 - \frac{1}{9} f F_{\text{pull}} l + \frac{1}{10} F_{\text{pull}}^2 \\
&- \frac{5}{144} F_{\text{pull}} f l + \frac{1}{18} F_{\text{pull}}^2 - \frac{5}{72} f^2 l^2 + \frac{1}{4} f F_{\text{pull}} l - \frac{2}{9} F_{\text{pull}}^2 \\
&+ \left. \frac{25}{288} f^2 l^2 - \frac{5}{18} F_{\text{pull}} f l + \frac{2}{9} F_{\text{pull}}^2 \right) \\
&+ \frac{hl^7}{E^2 I_{y'}^2} \left(\frac{25}{2304} f^2 l^2 - \frac{5}{288} f F_{\text{pull}} l + \frac{1}{36} F_{\text{pull}}^2 \right)
\end{aligned} \tag{B.17}$$

$$\begin{aligned}
I_{y'} &= \frac{hl^7}{E^2 I_{y'}^2} \left(\frac{1}{2592} f^2 l^2 - \frac{1}{288} f F_{\text{pull}} l - \frac{1}{168} f^2 l^2 + \frac{1}{84} f F_{\text{pull}} l + \frac{1}{126} F_{\text{pull}}^2 \right. \\
&+ \frac{1}{36} F_{\text{pull}} f l - \frac{1}{18} F_{\text{pull}}^2 + \frac{23}{720} f^2 l^2 - \frac{1}{9} f F_{\text{pull}} l + \frac{1}{10} F_{\text{pull}}^2 - \frac{5}{144} F_{\text{pull}} f l \\
&+ \frac{1}{18} F_{\text{pull}}^2 - \frac{5}{72} f^2 l^2 + \frac{1}{4} f F_{\text{pull}} l - \frac{2}{9} F_{\text{pull}}^2 + \frac{25}{288} f^2 l^2 - \frac{5}{18} F_{\text{pull}} f l \\
&+ \left. \frac{2}{9} F_{\text{pull}}^2 + \frac{25}{2304} f^2 l^2 - \frac{5}{288} f F_{\text{pull}} l + \frac{1}{36} F_{\text{pull}}^2 \right)
\end{aligned} \tag{B.18}$$

$$\begin{aligned}
I_{y'}^3 = & \frac{hl^7}{E^2} \left(\frac{1}{2592} f^2 l^2 - \frac{1}{288} f F_{\text{pull}} l - \frac{1}{168} f^2 l^2 + \frac{1}{84} f F_{\text{pull}} l + \frac{1}{126} F_{\text{pull}}^2 + \frac{1}{36} F_{\text{pull}} f l - \frac{1}{18} F_{\text{pull}}^2 + \frac{23}{720} f^2 l^2 \right. \\
& - \frac{1}{9} f F_{\text{pull}} l + \frac{1}{10} F_{\text{pull}}^2 - \frac{5}{144} F_{\text{pull}} f l + \frac{1}{18} F_{\text{pull}}^2 - \frac{5}{72} f^2 l^2 + \frac{1}{4} f F_{\text{pull}} l - \frac{2}{9} F_{\text{pull}}^2 + \frac{25}{288} f^2 l^2 - \frac{5}{18} F_{\text{pull}} f l \\
& \left. + \frac{2}{9} F_{\text{pull}}^2 + \frac{25}{2304} f^2 l^2 - \frac{5}{288} f F_{\text{pull}} l + \frac{1}{36} F_{\text{pull}}^2 \right) \tag{B.19}
\end{aligned}$$

$$\begin{aligned}
I_{y'} = & \left(\frac{hl^7}{E^2} \left(\frac{1}{2592} f^2 l^2 - \frac{6}{288} f F_{\text{pull}} l - \frac{1}{168} f^2 l^2 + \frac{1}{84} f F_{\text{pull}} l + \frac{1}{126} F_{\text{pull}}^2 + \frac{1}{36} F_{\text{pull}} f l - \frac{1}{18} F_{\text{pull}}^2 + \frac{23}{720} f^2 l^2 \right. \right. \\
& - \frac{1}{9} f F_{\text{pull}} l + \frac{1}{10} F_{\text{pull}}^2 - \frac{5}{144} F_{\text{pull}} f l + \frac{1}{18} F_{\text{pull}}^2 - \frac{5}{72} f^2 l^2 + \frac{1}{4} f F_{\text{pull}} l - \frac{2}{9} F_{\text{pull}}^2 + \frac{25}{288} f^2 l^2 - \frac{5}{18} F_{\text{pull}} f l \\
& \left. \left. + \frac{25}{2304} f^2 l^2 + \frac{1}{4} F_{\text{pull}}^2 \right) \right)^{\frac{1}{3}} \tag{B.20}
\end{aligned}$$

$$\begin{aligned}
I_{y'} = & \left(\frac{hl^7}{E^2} \right)^{\frac{1}{3}} \left(\left(\frac{l^2}{2592} - \frac{l^2}{168} + \frac{23l^2}{720} - \frac{5l^2}{72} + \frac{25l^2}{288} + \frac{25l^2}{2304} \right) f^2 + \left(-\frac{6F_{\text{pull}}l}{288} + \frac{F_{\text{pull}}l}{84} + \frac{F_{\text{pull}}l}{36} - \frac{F_{\text{pull}}l}{9} \right. \right. \\
& \left. \left. - \frac{5F_{\text{pull}}l}{144} + \frac{F_{\text{pull}}l}{4} - \frac{5F_{\text{pull}}l}{18} \right) f + \left(\frac{F_{\text{pull}}^2}{126} - \frac{F_{\text{pull}}^2}{18} + \frac{F_{\text{pull}}^2}{10} + \frac{F_{\text{pull}}^2}{18} - \frac{2F_{\text{pull}}^2}{9} + \frac{F_{\text{pull}}^2}{4} \right) \right)^{\frac{1}{3}} \tag{B.21}
\end{aligned}$$

$$\begin{aligned}
I_{y'} = & \frac{h^{1/3} l^{7/3}}{E^{2/3}} \left(\left(\frac{1}{2592} - \frac{1}{168} + \frac{23}{720} - \frac{5}{72} + \frac{25}{288} + \frac{25}{2304} \right) l^2 f^2 + \left(-\frac{6}{288} + \frac{1}{84} + \frac{1}{36} - \frac{1}{9} - \frac{5}{144} + \frac{1}{4} - \frac{5}{18} \right) F_{\text{pull}} l f \right. \\
& \left. + \left(\frac{1}{126} - \frac{1}{18} + \frac{1}{10} + \frac{1}{18} - \frac{2}{9} + \frac{1}{4} \right) F_{\text{pull}}^2 \right)^{1/3} \tag{B.22}
\end{aligned}$$

$$I_{y'} = \frac{h^{1/3} l^{7/3}}{E^{2/3}} \left(\frac{39619l^2}{725760} f^2 - \frac{13F_{\text{pull}}l}{84} f + \frac{19F_{\text{pull}}^2}{140} \right)^{1/3} \tag{B.23}$$

Appendix C

Derivation distributed load f

$$V_2 = \frac{\pi}{EI} \left(\frac{1}{9} f l^6 + \frac{3}{20} F_{\text{pull}} l^5 \right) \quad (\text{C.1})$$

$$f = \frac{Wg}{L} + P_0 w \left(1 - \frac{V_1}{V_2} \right) \quad (\text{C.2})$$

$$f = \frac{Wg}{L} + P_0 w - P_0 w V_1 (V_2)^{-1} \quad (\text{C.3})$$

$$f = \frac{Wg}{L} + P_0 w - P_0 w V_1 \left(\frac{\pi}{EI} \left(\frac{1}{9} f l^6 + \frac{3}{20} F_{\text{pull}} l^5 \right) \right)^{-1} \quad (\text{C.4})$$

$$f = \frac{Wg}{L} + P_0 w - P_0 w V_1 \left(\frac{\pi l^6}{9EI} f + \frac{3\pi F_{\text{pull}} l^5}{20EI} \right)^{-1} \quad (\text{C.5})$$

$$f \left(\frac{\pi l^6}{9EI} f + \frac{3\pi F_{\text{pull}} l^5}{20EI} \right) = \frac{Wg}{L} \left(\frac{\pi l^6}{9EI} f + \frac{3\pi F_{\text{pull}} l^5}{20EI} \right) + P_0 w \left(\frac{\pi l^6}{9EI} f + \frac{3\pi F_{\text{pull}} l^5}{20EI} \right) - P_0 w V_1 \quad (\text{C.6})$$

$$\frac{\pi l^6}{9EI} f^2 + \frac{3\pi F_{\text{pull}} l^5}{20EI} f = \frac{Wg \pi l^6}{9EIL} f + \frac{3Wg \pi F_{\text{pull}} l^5}{20EIL} + \frac{P_0 w \pi l^6}{9EI} f + \frac{3P_0 w \pi F_{\text{pull}} l^5}{20EI} - P_0 w V_1 \quad (\text{C.7})$$

$$\frac{\pi l^6}{9EI} f^2 + \left(\frac{3\pi F_{\text{pull}} l^5}{20EI} - \frac{Wg \pi l^6}{9EIL} - \frac{P_0 w \pi l^6}{9EI} \right) f - \frac{3Wg \pi F_{\text{pull}} l^5}{20EIL} - \frac{3P_0 w \pi F_{\text{pull}} l^5}{20EI} + P_0 w V_1 = 0 \quad (\text{C.8})$$

$$f = \frac{- \left(\frac{3\pi F_{\text{pull}} l^5}{20EI} - \frac{Wg \pi l^6}{9EIL} - \frac{P_0 w \pi l^6}{9EI} \right) \pm \sqrt{\left(\frac{3\pi F_{\text{pull}} l^5}{20EI} - \frac{Wg \pi l^6}{9EIL} - \frac{P_0 w \pi l^6}{9EI} \right)^2 - 4 \frac{\pi l^6}{9EI} \left(-\frac{3Wg \pi F_{\text{pull}} l^5}{20EIL} - \frac{3P_0 w \pi F_{\text{pull}} l^5}{20EI} + P_0 w V_1 \right)}}{2 \frac{\pi l^6}{9EI}} \quad (\text{C.9})$$